Development of a converter for grid-tied and isolated operation of an interior permanent magnet synchronous generator, coupled to a twin-shaft gas turbine

By: Molaoa Molaoa

Thesis submitted to the Department of Electrical Engineering, University of Cape Town, in complete fulfilment of the requirements for the degree of Master of Science in Electrical Engineering

10th of August 2018

Declaration

This dissertation is submitted to the Department of Electrical Engineering, University of Cape Town, in complete fulfilment of the requirements for the degree of Master of Science in Electrical Engineering. It has not been submitted before for any degree or examination at this or any other university.

"I know the meaning of plagiarism and declare that all the work in the document, save for that which is properly acknowledged, is my own. This thesis/dissertation has been submitted to the Turnitin module (or equivalent similarity and originality checking software) and I confirm that my supervisor has seen my report and any concerns revealed by such have been resolved with my supervisor."

Signed by candidate

M. Molaoa

10th of August 2018

Assessment of Ethics in Research Projects form

EBE Faculty: Assessment of Ethics in Research Projects (Rev2)

Any person planning to undertake research in the Faculty of Engineering and the Built Environment at the University of Cape Town is required to complete this form before collecting or analysing data. When completed it should be submitted to the supervisor (where applicable) and from there to the Head of Department. If any of the questions below have been answered YES, and the applicant is NOT a fourth year student, the Head should forward this form for approval by the Faculty EIR committee: submit to Ms Zulpha Geyer (Zulpha.Geyer@uct.ac.za; Chem Eng Building, Ph 021 650 4791).
NB: A copy of this signed form must be included with the thesis/dissertation/report when it is submitted for examination

This form must only be completed once the most recent revision EBE EiR Handbook has been read.

Name of Principal Researcher/Student: MOLAOA MOLAOA Department: Electrical Engineering

Preferred email address of the applicant:

If a Student: Degree: MSc. Supervisor: A.Prof. Azeem Khan

If a Research Contract indicate source of funding/sponsorship: N/A

Research Project Title: Development of Back to Back converter to interface a High speed Permanent Magnet generator to the grid and an isolated load

Overview of ethics issues in your research project:

Question 1: Is there a possibility that your research could cause harm to a third party (i.e. a person not involved in your project)?	YES	(NO)
Question 2: Is your research making use of human subjects as sources of data? If your answer is YES, please complete Addendum 2.	YES	(NO)
Question 3: Does your research involve the participation of or provision of services to communities? If your answer is YES, please complete Addendum 3.	YES	(NO)
Question 4: If your research is sponsored, is there any potential for conflicts of interest? If your answer is YES, please complete Addendum 4.	YES	(NO)

If you have answered YES to any of the above questions, please append a copy of your research proposal, as well as any interview schedules or questionnaires (Addendum 1) and please complete further addenda as appropriate. Ensure that you refer to the EiR Handbook to assist you in completing the documentation requirements for this form.

I hereby undertake to carry out my research in such a way that

- there is no apparent legal objection to the nature or the method of research; and
- the research will not compromise staff or students or the other responsibilities of the University;
- the stated objective will be achieved, and the findings will have a high degree of validity;
- limitations and alternative interpretations will be considered;
- the findings could be subject to peer review and publicly available; and
- I will comply with the conventions of copyright and avoid any practice that would constitute plagiarism.

Signed by:

	Full name and signature	Date
Principal Researcher/Student:	Signed by candidate	12/10/15
This application is approved by:		
Supervisor (if applicable):		14/10/15
HOD (or delegated nominee): *Final authority for all assessments with NO to all questions and for all undergraduate research.*	Signed by candidate	27/1/16
Chair : Faculty EIR Committee For applicants other than undergraduate students who have answered YES to any of the above questions.		

Acknowledgments

I would like to thank my family for their generous love and support throughout my time at UCT.

My sincere gratitude to Prof. M.A. Khan and Prof. P. Barendse for their guidance and support throughout the project.

I would also like to thank Chris Wozniak and Phillip Titus. Their technical knowhow is invaluable and without them I would never have managed to complete this project.

A special thank you to my fellow members of the AMES group, for their input, whenever I required advice.

I would like to thank the technical team in the lab. This project was truly a team effort, and their help in assembling the rig is greatly appreciated.

Abstract

South Africa's overreliance on coal fired power generation has led to the government's commitment to diversifying the country's energy mix. Gas turbine generators are poised to play a larger role in South Africa's energy mix, due to the country's abundance in natural gas reserves. Therefore, there is a need to developed gas turbine emulation systems to investigate how this transition is to be implemented and to discover new efficient ways to generate power through gas turbines.

This thesis presents the development of a twin-shaft gas turbine emulator. A DC-machine that accepts both torque and speed references is used to emulate the behaviour of the gas turbine according to a modified Rowen gas turbine model. The emulator is coupled to a 1.5kW interior permanent magnet synchronous generator (IPM). The power density of a DC-machine is significantly lower than that of a gas turbine of the same rating. Thus, the DC-machine is rated at double the rating of the IPM to overcome the high inertia it has when compared to a gas turbine of the same rating. This means that the DC-machine can produce large toques to successfully emulated the dynamic behaviour of the gas turbine. A maximum error 2.5% in the emulation of the gas turbine's speed is reported.

A two-level active converter is used to compare control strategies for an IPM. Ninety-degree torque angle (NTA) control, maximum torque per ampere (MTPA) control and unity power factor (UPF) control are compared for performance. The UPF and MTPA control result in the lowest and second lowest DC-link utilisation respectively when compared to NTA control. This is due to a negative d-axis current component as opposed to a zero d-axis current component in the case of NTA control. It is also concluded that to achieve a high power factor and torque development, a negative d-axis current component is required. UPF and MTPA control perform well in both categories, with UPF control and MTPA control resulting in the highest power factor and developed torque respectively. A fourth control strategy that maximises the efficiency of the IPM is developed experimentally. The maximum efficiency (ME) control strategy minimises mechanical, core, windage and conduction losses. It also results in near unity power factor and near maximum developed torque.

A nonconventional control structure that involves control of the DC-link from the generator-side converter is presented. This frees the outer-loop control of load-side converter to

regulate voltage across the load when the system is supplying power to an isolated load. This control structure also allows the grid-side converter to employ reactive power compensation, without having to regulate the DC-link voltage at the same time. In doing so, large grid currents are avoided.

A recursive least squares (RLS) algorithm is used to separate negative and positive sequence current components during grid voltage unbalance. A method to minimise the presence of negative sequence components in the load current is presented and implemented successfully in an experiment.

Table of Contents

List of figures

List of tables

List of abbreviations

IPM	Interior permanent magnet machine
NTA	Ninety-degree torque angle
MTPA	Maximum torque per ampere
UPF	Unity power factor
ME	Maximum efficiency
RLS	Recursive least squares
PMSG	Permanent magnet synchronous generator
LCL	Inductor-capacitor inductor topology
PMSM	Permanent magnet synchronous motor
THD	Total harmonic distortion
LC	Inductor-capacitor topology
EMF	Electromotive force
SPM	Surface-mounted permanent magnet machine
L	Inductor topology
PI	Proportional-integral
PLL	Phase-locked loop
SRF-PLL	Synchronous reference frame Phase-locked loop
RMS	Root-mean-square
SVPWM	Space vector pulse width modulation
SPWM	Sine wave pulse width modulation
RC	Resistor-capacitor topology
ESR	Equivalent series resistance
V_{CE}	Collector-emitter voltage

List of symbols

$\dot{w}$	Rate of change of energy	W
$\dot{m}$	Rate of change of mass	$kg \cdot s^{-1}$
T	Temperature	K
C	Specific heat capacity	$J \cdot K^{-1}$
η	Efficiency	
a	Valve position constant	
b	Valve position constant	
c	Valve position constant	
k_{flma}	No load fuel parameter	
k_{flmb}	No load fuel parameter	
T_c	Combustion time delay	s
K_{pft}	Speed governor proportional constant	
K_{tft}	Speed governor integral constant	
τ_{FS}	Fuel system time constant	s
τ_{CP}	Compressor discharge volume	s
J_T	Combined free-turbine, generator inertia	$kg \cdot m^2$
B_T	Combined free-turbine, generator viscous damping	$N \cdot s \cdot m^{-1}$
V_{sx}	Stator terminal phase voltage	V
λ_{sx}	Total stator flux-linkage	Wb·turns
R_s	Stator resistance	Ω
i_{sx}	Stator phase current	A
L_x	stator phase inductance	H
ω_e	angular velocity of magnetic field	$rad \cdot s^{-1}$
λ_{pm}	stator flux-linkage from permanent magnet	Wb·turns
P_G	Active power from generator	W
Q_G	Reactive power from generator	Var
T_m	Mechanical torque	N·m
T_e	Electromagnetic torque	N·m

ω_{res}	Resonance frequency	rad·s^{-1}
L_f	Filter inductor	H
C_f	Filter capacitor	F
R_f	Filter damping resistor	Ω
e_g	Grid voltage	V
P_{load}	Active load power	W
Q_{load}	Reactive load power	Var
V_{dc}	DC-link capacitor voltage	V
i_{dc}	DC-link capacitor current	A
τ_{dq}	d-axis and q-axis electrical constant	s
f_b	Bandwidth	Hz
f_{sw}	Switching frequency	Hz
ω_g	grid voltage frequency	rad·s^{-1}
Z_b	Base impedance	Ω
L_b	Base inductance	H
C_b	Base capacitance	F
θ_t	Torque angle	rad

Chapter 1

1. Introduction

1.1 Background

A gas turbine generator is comprised of a gas turbine that acts as the prime mover coupled to an electric generator that delivers electric power to a load. Due to its compact size, high-power density and relatively low-cost of installation, gas turbine generators are used in a variety of applications. In 1976 Allision Engine Co. produced a 150kW generator driven by a GT 404 gas turbine for a radar set for the United States army. A gas turbine generator was used to meet the objectives of the project, which were to develop a power generation unit that would fit on to a truck, that was fuel efficient, robust and that had multi-fuel capabilities [1]. Gas turbine generators have also found use in peak-load generation due to their fast start-up times. In [2], a gas turbine plant of 17.5MW is discussed which takes just 2 minutes to start-up, synchronize and deliver power to the utility grid. These advantages along with the ease of deploying gas turbine generators and the reduced cost thereof when compared to other forms of power generation is what has contributed to the increasing interest in the study of gas turbine generators.

Natural gas is the cleanest carbon-based fuel when it comes to carbon emissions. Due to its lower carbon content and high energy density, it emits half and a third of the carbon dioxide produced by coal and oil respectively per unit energy [3]. This is significant in the South African context because over 90% of electricity in South Africa is generated by coal-fired power plants, which makes the country one of the largest emitters of carbon emissions in the world. However, South Africa has large natural gas reserves in the Karoo and offshore, and thus has an opportunity to diversify its power generation capabilities into cleaner gas turbine generators [4].

Natural gas is sourced from a process known as hydraulic fracturing. This labour intensive process involves drilling into the earth and fracturing rock with water to release natural gas. The gas industry is still very much unexplored in South Africa and has the potential to create thousands of jobs in a country at a time when the unemployment rate is approaching 30%. It

is for these reasons South Africa has committed itself to investing in both gas imports as well sourcing gas locally [5].

The ecological damage that can result from hydraulic fracturing has stoked controversy and resulted in a few detractors. Water contamination is chief among the concerns hydraulic fracturing raises, specifically in fragile ecosystems like the Karoo and the coast.

It is not unusual in South Africa for a remote village's power demand to be supplied by solar power, completely isolated from the utility grid. This has led to an increased interest in distributed generation particularly in remote rural areas [6]. The focus has been on solar and wind power which has a much higher installation costs than that of gas turbine generation. Multi-fuel gas turbines are ideal for use in rural and remote areas due to their robustness and can be sustainable if biogas is used as fuel.

Gas turbine generation is increasingly seen as a viable alternative to coal based generation due the low cost of installation, the abundance of gas reserves available and the socio-economic upliftment that will result. Therefore, it is necessary for studies involving the operation of such generators to be conducted to tackle key issues in the development of the industry.

1.2 Literature Review

In this thesis a DC-machine is used to emulate a twin-shaft gas turbine. The turbine is coupled to an interior permanent magnet machine (IPM) which acts as the electrical generator. A two-level back-to-back converter interfaces the IPM with the grid or an isolated load through an LCL-filter.

An overview of gas turbine models is provided in [7]. The first type of model discussed are physical models; they are derived from the thermodynamic laws governing the Brayton cycle, which describes the operations of a heat engine. A further description of the thermodynamic processes of a gas turbine is provided in [8], [9], from which differential equations modelling the gas turbine are derived. The second type of model is the Rowen model. It comprises of transfer functions that represent processes within the gas turbine [10], [11]. The transfer functions are found experimentally from four gas turbines of different ratings to produce a per unit model of a gas turbine. Due to the simplicity of the Rowen model, it has been

referenced the most out of all the models in literature. The Rowen model was conceived initially for a single-shaft gas turbine; however, other works have since expanded on it to include multi-shaft gas turbines. The third model is the IEEE model [12]. It was developed by the IEEE Working Group on Prime Mover and Energy Supply Models for System Dynamic Performance Studies. It is very similar to the Rowen model with the difference primarily being the control mechanisms of the system. Other models are explained in depth in [7] and are variations of Rowen's model.

The use of DC-machines as turbine emulators is prominent in wind energy [13], [14]. The high cost of turbine installation means testing of generators on wind turbines can become very expensive. Thus, turbine emulators are developed to test generators before their real-world deployment. Emulators allow for changes in test scenarios which could include a change of rated conditions or abnormal conditions that are difficult to replicate on a real turbine. Gas and fuel turbine emulators have also been developed to a lesser extent. In [15], [16], a twin-shaft gas turbine emulator is developed using a permanent magnet synchronous motor (PMSM). The PMSM actuates torque and speeds according to a model on the motor's controller. The Rowen model was used in the work as the reference model for a gas turbine.

The control of a PMSG has been discussed extensively in literature. The PMSG comprises of a mechanical and electrical model. Control is achieved by manipulating the PMSG's direct and quadrature axis (d-axis and q-axis) current [17], [18]. Multiple strategies exist that ensure efficient operation of the generator [19]; they include ninety-degree torque angle (NTA) control, unity power factor (UPF) control and maximum torque per ampere (MTPA) control among others. Most control objectives involve loss minimisation and optimal power production. NTA control involves controlling the d-axis current to zero. This strategy is simple to implement and for a surface mounted permanent magnet machine (SPM) will also result in minimal copper losses for the power produced, this however does not apply to an IPM. In UPF control, the VA rating of the generator goes towards active power production. The result is a greater constant torque range for the PMSG. MTPA control generates the greatest amount of torque from the current in the stator. As a result, conduction losses in the stator are at a minimum for each stator current magnitude [19]-[21]. This method however does not consider the generator core and windage losses. IPMs have different d-axis and q-axis inductances, which can complicate control when implementing UPF and MTPA control. D-axis

and q-axis inductances are known to vary during the operation of the machine, which can further complicate control [22]. However, the difference in the d-axis and q axis inductances, allow for the extension of the speed range for an IPM [23].

In most cases power generation focuses on active power transfer to grid. In grid-tied operation, power is delivered to the grid in a manner that prevents inverter saturation. Inverter saturation refers to the scenario when the inverter is unable to produce the required phase voltages. This occurs when the line-to-line voltage of the gird or load is higher than the converter's DC-link voltage. To prevent inverter saturation, the DC-link is regulated to a sufficiently high value. Grid codes can stipulate the requirement of rated power delivery at the rated voltage when dealing with a weak grid or an isolated network. This has led to the development of static synchronous compensators that aid in the regulation of a network's voltage [24], [25]. In the event of an isolated load, the generator system must supply all the power demanded by the load. A standalone wind power generation system is discussed in [26] where load voltage is regulated by control of the load currents. This method is incomplete as inverter saturation can occur should the power generated by the PMSG be less than the power delivered to the load. To address this issue the authors in [27]-[29] provides a solution that alternates between the control tabled in [26] and the traditional grid-tied operation which regulates the DC-link voltage of the converter. Hence, the control on the load-side alternates between regulating the DC-link voltage and the load-voltage. Only one voltage can be regulated at one time. Therefore, this control approach may lead to significant load voltage and DC-link voltage oscillation if the control does not act quickly enough. A provision for when the generator produces more power than the load consumes is not given, which could lead to overloading of the isolated load.

Isolated networks inherently have weak grids which can cause grid voltage unbalance during asymmetrical loading of the phases. This causes an oscillation of twice the grid frequency in the d-axis and q-axis phase currents. The oscillation is a result of the presence of negative sequence currents within the load-side currents. The oscillations can cause the control of the system to fail and results in increase in losses in the converter's DC-link capacitor. In [30], [31] the positive sequence and negative sequence components are separated using a notch filter. The positive sequence components are controlled through PI controllers to achieve the system's main objective of power delivery. A second set of PI controllers work to suppress

negative sequence currents. The converter switching signals are a result of both sets of controllers. The biggest advantage of this method is that one converter is used for power delivery and for mitigation of current unbalance. The drawback is that large phase voltages can result, which can lead to inverter saturation. Therefore, this method is only suitable for small grid unbalances.

It is necessary to filter the output currents of an inverter before being delivered to the grid or load because of the presence of switching harmonics. The simplest filter consists of an inductor on each phase and is called an L-filter. Controlling currents in an L-filter is simple because the grid/load-side converter is inherently stable. The drawback, however, is that large inductors are required for sufficient attenuation of harmonics, which results in significant voltage drops across the inductor. The large voltage drop will require a higher DC-link voltage and consequently a larger DC-link capacitor which can be costly. LC and LCL-filters are used to provide greater attenuation with smaller components, the latter has become the industry standard in filter topology; a comparison of the three is given in [32]. The smaller components result in less conduction losses across the filter. A drawback of LCL-filters the existence of a resonance frequency, at which currents are uncontrollably amplified. To mitigate the effects of resonance, active and passive damping techniques have been developed [33]. Active damping methods involve the use of voltage or current sensors to inject currents in a controlled manner that mitigates the effect of resonance. Passive methods involve putting a resistor in series with the filter capacitor. The low cost of passive damping in terms of components and control complexity make it an attractive prospect. Passive damping, however, results in greater losses at high power. The design process of an LCL-filter is an iterative process involving multiple design objectives [34]-[36]; in the end an optimal solution is found.

It must be noted that in this thesis, the load-side refers to the side of the system that the grid or isolated load is found. If the system is feeding an isolated load it will be explicitly be stated in the thesis. If the system is connected to the utility grid, the system is said to be grid-tied, and this will be explicitly stated as well. Otherwise, load-side refers to the system in either modes of operation. The gas turbine generator refers to the entire system, which includes the gas turbine prime mover and the PMSG.

1.3 Research questions

This thesis focuses on the issues concerning the emulation of a twin-shaft gas turbine engine, its effect on the directly coupled IPM, and the efficient control thereof. An investigation into the operation of the IPM in grid-tied and isolated operation is conducted. Solutions for issues that result from grid voltage unbalance are also discussed. Theory is substantiated through simulation and validated through experimental implementation; the research questions are as follows:

- How can a twin-shaft gas turbine engine be emulated with DC-motor?
- How can the IPM be operated in a manner that guarantees maximum efficiency of the generator and optimal operation of the entire system?
- How can an IPM be operated for both grid-tied and isolated operation?
- Which is the optimal control structure required for gas turbine generator?
- How can the effects of grid voltage unbalance on the system be mitigated?

1.4 Objectives

The objectives of this project are as follows:

- Implement a twin-shaft gas turbine emulator in the lab.
- Develop and implement the control of an IPM driven by a twin-shaft gas turbine in simulations and experimentally.
- Implement both grid-tied and isolated operation on the IPM.
- Compare and assess the different control strategies of the IPM.
- Ensure adequate power supply in both grid-tied and isolated operation according to grid codes.

1.5 Scope and Limitations

The IPM used in this project is rated for a speed of 1500RPM and 1.5kW. However, due to a malfunctioning rotary encoder, speed values above 1100RPM could not be read. The lower speed meant a lower induced EMF in the generator; the grid voltage and DC-link reference

voltages were in turn lowered accordingly. A complete discussion as to the reasons why this was done is provided in section 6.2.3.

1.6 Structure

The theoretical bases regarding the modelling of a twin-shaft gas turbine and a PMSG is provided in chapter 2. In chapter 3, a deeper investigation on the operation of an IPM is conducted. In chapter 4, the models of the gas turbine, the IPM and the load-side system are simulated in isolation to validate the theories from the previous chapters. The experimental setup is discussed in chapter 5 and the results from the experimental implementation are given in chapter 6. Conclusions and recommendations are given in chapter 7.

Chapter 2

2. Theory and basic principles of twin-shaft gas turbines and PMSGs

The fundamental concepts of the operation of a gas turbine and a PMSG are discussed in this chapter. The gas turbine models are presented and compared, and the Rowen model is selected for implementation in the turbine emulator. The modelling of an IPM is discussed in detail and provides the basis to the control strategies presented in chapter 3.

2.1 Gas turbine theory

A diagram of a twin-shaft gas turbine is provided in figure 1. The gas generator turbine and compressor are mechanically coupled. The free-turbine and gas generator turbine are thermodynamically linked and no mechanical coupling exists. This allows the two turbines to rotate at different speeds [9], [37].

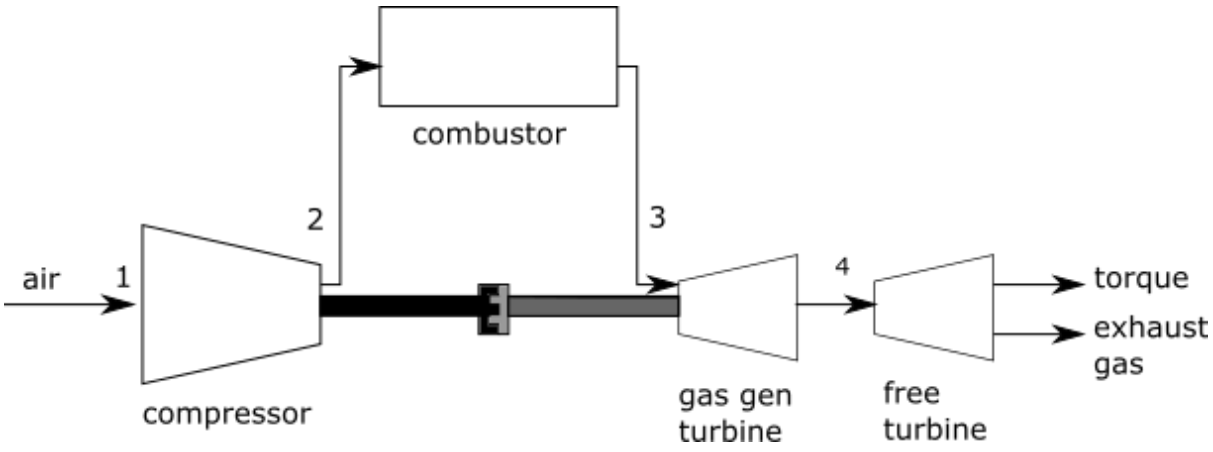

Figure 1: Twin-shaft gas turbine

The thermodynamic processes within a gas turbine can be modelled in terms of the conservation of internal mass and the conservation of internal energy [8], [9] principle. The rate of change of energy, $\dot{w}$, within a thermodynamic process is directly proportional to the rate of change of mass, $\dot{m}$, and the change in temperature T. The constant of proportionality is called the specific heat capacity C [38]. In figure 1, the compressor's function is to increase the pressure and the temperature of the fluid within its chamber. The input power necessary for this process is given in equation 2.1.

$$\dot{w}_c = \eta_c \dot{m}_a C_{pa}(T_2 - T_1) \tag{2.1}$$

The compressors inlet and outlet temperatures are T_1 and T_2 respectively. The process is not ideal and will therefore include an efficiency term η. The temperature of the fluid is raised in the combustor to T_3, which increases its pressure. The fluid is then expanded in the gas generator turbine, providing the power to drive the compressor through the mechanical coupling. The power produced in this process is given in equation 2.2.

$$\dot{w}_g = \eta_{T1}(\dot{m}_a + \dot{m}_f) C_{pg}(T_4 - T_3) \tag{2.2}$$

$\dot{m}_f$ represents exhausted fumes, T_4 and T_3 are the outlet and inlet turbine temperatures respectively. The fluid is further expanded in the free-turbine, further transferring power in the process. The model is overly simplified; for example, some energy goes into heating the lubricating oil. Therefore, a more realistic expression for the thermodynamic cycle is expressed in equation 2.3.

$$\eta_{T1}(\dot{m}_a + \dot{m}_f) C_{pg}(T_4 - T_3) + \eta_c \dot{m}_a C_{pa}(T_2 - T_1) + \dot{m}_{Lubric.Oil} C_{poil}(T_{oil\ out} - T_{oil\ in}) = 0 \tag{2.3}$$

Attempting to model the gas turbine according to its thermodynamic processes is difficult due to the many variables involved and other unmodeled dynamic behaviour. In [11], a more practical approach of modelling is taken. The model is created specifically for a twin-shaft model unlike most models which are specific to single-shaft turbines [10]. An attempt to relate turbine output variables like exhaust temperature, gas generator and free-turbine speeds to the turbine's fuel flow and generator turbine speed is made. The experiment was conducted on a 46MVA gas turbine generator which makes this approach specific to the gas turbine generator used in the experiment.

In [37], a simpler approach is presented, which adapts a popular turbine model known as the Rowen model into a twin-shaft gas turbine model. The turbine speed governor, valve positioner, fuel system, combustor, compressor, free-turbine and gas turbine are described by first order transfer functions. The block diagram of the model is illustrated in figure 2.

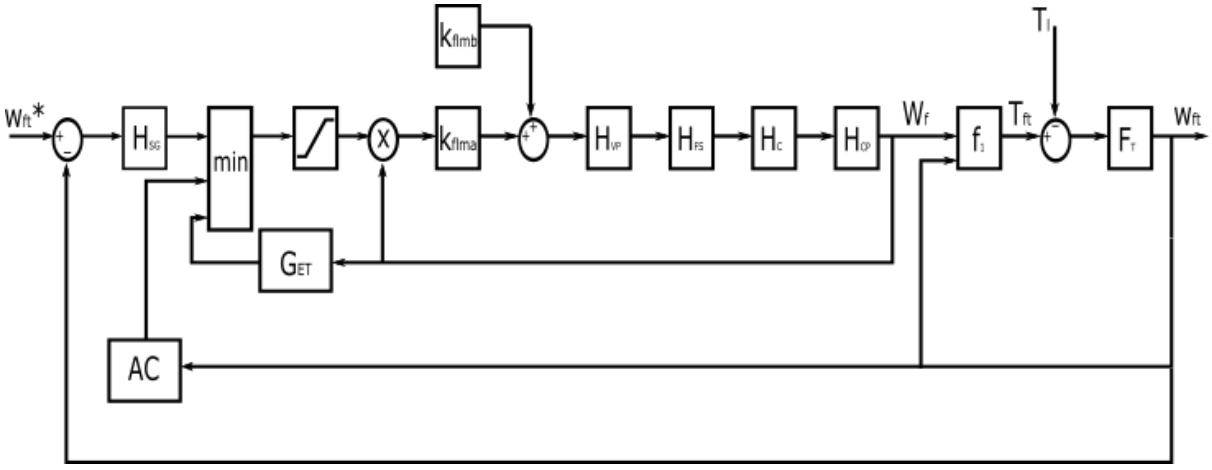

Figure 2: A simplified model of a twin-shaft gas generator

Control of the gas turbine is independent of the control of the electrical generator it drives. Thus, for a completeness sake, the control of the gas turbine must be emulated along with the gas turbine. The gas generator turbine (G_{ET}) speed, free-turbine (F_T) speed, acceleration (AC), and exhaust and inlet temperatures all require control. Control is achieved by regulating the fuel flow to the combustor W_f [11]. To regulate the gas turbine variables, a low-value-select (min) is used to select the most critical variable that needs to be regulated. During normal operation the speed control determines the fuel flow. However, if the gas generator turbine speed or free-turbine acceleration approaches its maximum values, the fuel flow will work to limit them as to not to damage the gas turbine generator. Therefore, only one variable is controlled at a time. In [16], the temperature control is ignored for simplicity sake, and the speed control of the gas generator and free-turbine, and the acceleration control of the free-turbine become the focus, as illustrate in figure 2. The transfer functions in figure 2 are elaborated on in equations 2.4-2.10 and their parameters are given in table 1.

$$H_{SG} = \frac{K_{pft}s + K_{tft}}{s} \tag{2.4}$$

$$H_{VP} = \frac{\left(\frac{a}{c}\right)}{1 + \left(\frac{b}{c}\right)s} \tag{2.5}$$

$$H_{FS} = \frac{1}{1 + \tau_{FS}s} \tag{2.6}$$

$$H_C = e^{-sT_C} \tag{2.7}$$

$$f_1(W_F, \omega_{GT}) = \frac{1}{k_{flmb}}\left[\left(W_f - k_{flma}\right) + 0.5(1 - \omega_{GT})\right] \tag{2.8}$$

$$F_T = \frac{1}{J_T s + B_T} \tag{2.9}$$

$$H_{CP} = \frac{1}{1 + \tau_{CP} s} \tag{2.10}$$

Table 1: parameters to equation 2.4

Symbol	Quantity	Value
a	Valve position constant	1.00pu
b	Valve position constant	0.05pu
c	Valve position constant	1.00pu
$\mathbf{k_{flma}}$	No load fuel parameter	0.20pu
$\mathbf{k_{flmb}}$	No load fuel parameter	0.80pu $(1 - \mathrm{k_{flma}})$
$\mathbf{T_c}$	Combustion time delay	0.01s
$\mathbf{K_{pft}}$	Speed governor proportional constant	1.00pu
$\mathbf{K_{tft}}$	Speed governor integral constant	2.00pu/s
$\boldsymbol{\tau_{FS}}$	Fuel system time constant	0.40s
$\boldsymbol{\tau_{CP}}$	Compressor discharge volume	0.10s
$\mathbf{J_T}$	Combined free-turbine, generator inertia	-
$\mathbf{B_T}$	Combined free-turbine, generator viscous damping	-

The parameters in table 1 are given in per unit values; they were obtained from studying four heavy duty gas turbines generators ranging from 19 686kW to 80 685kW [10].

In a twin-shaft gas turbine, the generator is coupled to the free-turbine. Thus, the gas generator turbine that produces the power for the unit and the electric generator can run at different speeds. This means the gas generator turbine can run at its optimal speed, which is usually very high, to produce maximum power, while the generator runs at a much lower speed. An increase in the speed of the gas generator turbine can be achieved by increasing

the fuel flow to the combustor which results in higher air mass flow into the system. The increase in inlet temperature, mass flow and pressure raises the power available to the gas generator turbine and subsequently the free-turbine [8]. The twin-shaft gas turbine is known to be more efficient at part-load as compared to the single-shaft gas turbine, which makes it an ideal candidate for supplying power to an isolated load or network, where the load can change over time [39]. It is also mentioned in [8] that near the free-turbine's optimal speed, the efficiency of the system is high and varies very little. This gives the possibility of varying the mechanical power supply of the gas generator system by changing the speed of the free-turbine without significantly compromising efficiency.

The single-shaft gas turbine is typically used in high speed applications, while the twin-shaft gas turbine is used in low speed applications. Twin-shaft gas turbine generators typically do not require any power electronics to interface to a load or grid; they are connected to the free-turbine directly or through a gearbox that will decrease generator speed to the rated frequency of the grid [40], [41]. Two main methods for emulating gas turbine generators have been discussed in literature. In [15], two machines are utilized to emulate the gas turbine generator. The first machine acts as the gas turbine, the second machine is a generator that provides power for an isolated load. In [42], a two-level back-to-back converter is used to emulate the electrical power production of a gas turbine generator. The active front end inverter on the converter feeds an isolated load and acts as the electrical output of the gas turbine-synchronous generator unit.

2.2 Power electronic interfacing

A twin-shaft gas turbine generator does not usually require a power electronics interface since the gas turbine control regulates the speed of the free-turbine, as stated in section 2.1. However, having a power electronics interface allows for greater controllability of the generator and allows for implementation of power quality measures. The power electronics interface is a converter which consists of switching devices situated on each phase of the generator. Three generator-converter arrangements are discussed in this chapter.

The first arrangement is illustrated in figure 3 and depicts the usual structure of a twin-shaft gas generator. The PMSG is directly coupled to the free-turbine and power is fed straight to a load or grid. The gas turbine system is responsible for regulating the speed of the generator.

If the rated speed of the free-turbine is higher than that of the nominal frequency of the load, a gearbox is utilized between the PMSG and the free-turbine.

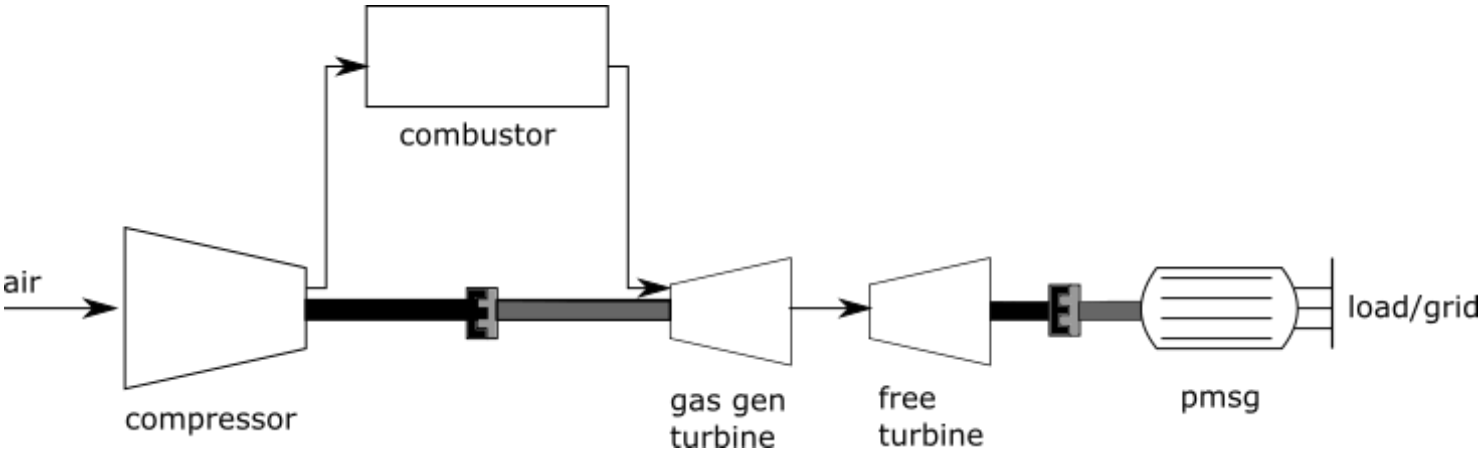

Figure 3: Gas turbine generator system

While figure 3 illustrates a cost-effective arrangement of the system, it does not provide a method of controlling the power being delivered to the load. In [43], [44] single-shaft gas turbine generators which run at high speeds are discussed. There is a requirement for a converter interface between the gas turbine and the load because of the high frequency electric output power produced. A diode rectifier is used to convert the high frequency power from the generator to DC. An inverter is used to supply power to the load at rated frequency. The inverter can also allow for the control of the power factor as well if necessary. The same scheme can be applied to a twin-shaft gas turbine. This would eliminate the need for a gearbox if the free-turbine speed differs from the nominal frequency of the load. In section 1.5 it was stated that the IPM was not able to achieve rated speed. Therefore, in this thesis a converter is necessary to interface the generator to the load. An illustration of this approach is given in figure 4.

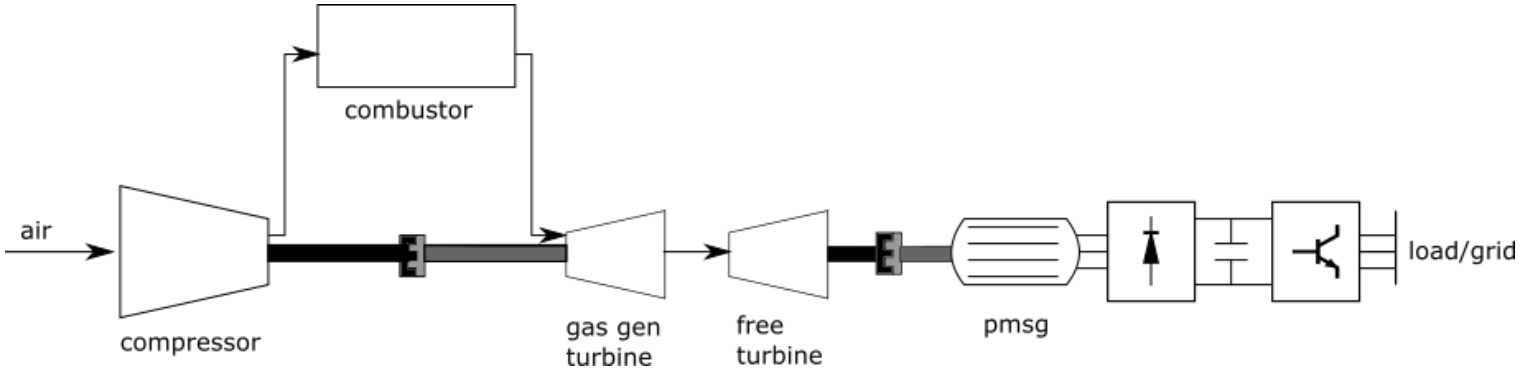

Figure 4: Gas turbine generator system with rectifier-inverter interface

It is mentioned in [44] that during load changes, the speed of the free-turbine can severely be affected, resulting in undesirable oscillations in the generator's output power. The burden then solely lies on the gas turbine's speed governor to mitigate the oscillations. A solution to this would be to employ an active front end rectifier, that enables controllability of the PMSG through converter switching. Load scheduling can be implemented to avoid sudden acceleration or deceleration of the free-turbine, by controlling generator currents. The PMSG's electromagnetic torque acts as the load on the free-turbine. If the PMSG's electromagnetic torque decreases the free-turbine speed would increase above the reference speed. The turbine speed governor would react by decreasing the fuel supply and thus the mechanical torque input from the gas turbine. The opposite would occur if the PMSG's electromagnetic torque increases. The generator's electromagnetic torque is determined by its currents. Therefore, by manipulation the PMSG's currents the mechanical power delivered to the generator can be altered, which is what is required for successful load scheduling.

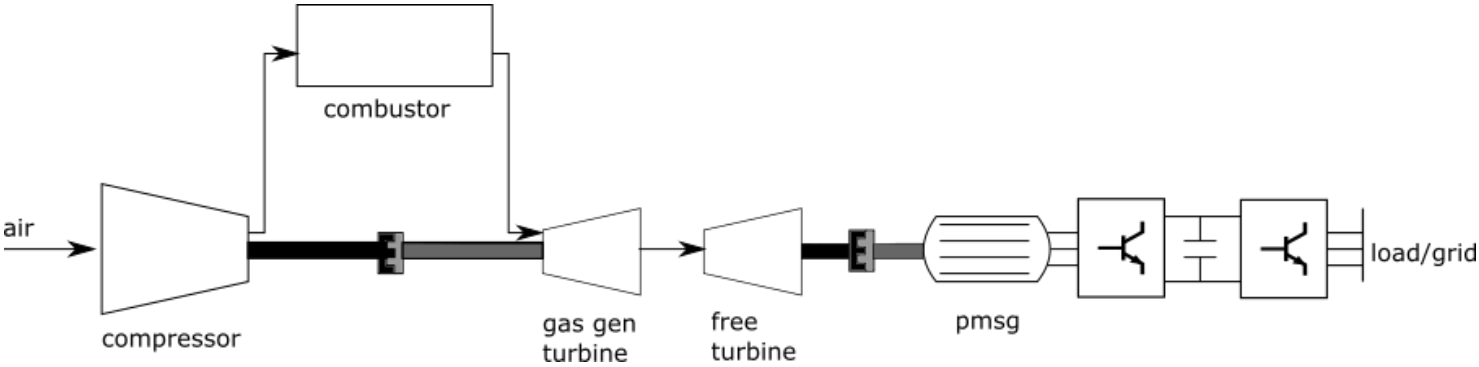

Figure 5: Gas turbine generator with active front end rectifier-inverter interface

In this thesis a two-level back-to-back converter with active front end rectifier and inverter is used to interface the gas turbine generator to the load. Multilevel converter can be implemented in the same manner; however, their use is mostly reserved for high voltage applications.

2.3 PMSG model

The IPM is used as the generator in this thesis. This section describes the model of an IPM and highlights its characteristics.

A PMSG generates voltage by rotating its permanent magnet rotor within its stator windings. The change in the flux-linkage of the stator windings as the magnets on the rotor change positions induces an EMF in the stator. The distribution of the flux-linkage density is sinusoidal resulting in sinusoidal voltages on the stator terminals. The phase stator equations are given

in equation 2.11-2.13. V_{sx} is the phase terminal voltage and varies sinusoidally, λ_{sx} is the total phase flux-linkage, R_s is the stator resistance and i_{sx} is the stator current.

$$V_{sa}(t) = \frac{d\lambda_{sa}(t)}{dt} + R_s i_{sa}(t) \tag{2.11}$$

$$V_{sb}(t) = \frac{d\lambda_{sb}(t)}{dt} + R_s i_{sb}(t) \tag{2.12}$$

$$V_{sc}(t) = \frac{d\lambda_{sc}(t)}{dt} + R_s i_{sc}(t) \tag{2.13}$$

The flux-linkage of each phase windings is a combination of the phase's self-inductance flux-linkage $L_x i_{sx}$, the flux-linkage from mutual inductance $M_{xy} i_{sx}$ and the flux-linkage from the permanent magnet λ_{pm}.

$$\lambda_{sa}(t) = L_a i_{sa}(t) + M_{ab} i_{sb}(t) + M_{ac} i_{sc}(t) + \lambda_{pm} \cos(\omega_e t) \tag{2.14}$$

$$\lambda_{sb}(t) = L_b i_{sb}(t) + M_{ba} i_{sa}(t) + M_{bc} i_{sc}(t) + \lambda_{pm} \cos\left(\omega_e t - \frac{2\pi}{3}\right) \tag{2.15}$$

$$\lambda_{sc}(t) = L_c i_{sc}(t) + M_{ca} i_{sa}(t) + M_{cb} i_{sb}(t) + \lambda_{pm} \cos\left(\omega_e t - \frac{4\pi}{3}\right) \tag{2.16}$$

Using Clarke's transformation, the three phase PMSG electrical model can be represented by a single space-vector rotating in the *α-β* plane. The space-vector rotates with the magnetic field's angular velocity of ω_e.

$$\overrightarrow{V_s} e^{j\omega_e t} = \frac{d\overrightarrow{\lambda_s} e^{j\omega_e t}}{dt} + R_s \overrightarrow{i_s} e^{j\omega_e t} \tag{2.17}$$

A set of orthogonal axes are imposed on the rotating vector as shown in figure 6. The *d-q* axes rotate at the same angular frequency as the space-vector. Within the *d-q*-axes the rotating vector is perceived as stationary. Thus, time varying quantities can be analysed as DC quantities in the *d-q* plane. By decomposing the space-vector into *d-q* components and treating the *q*-axis as the imaginary axis and the *d*-axis as the real axis, *d-q* stator equations can be derived. The *d-q* stator equations are shown in equations 2.19 and 2.20.

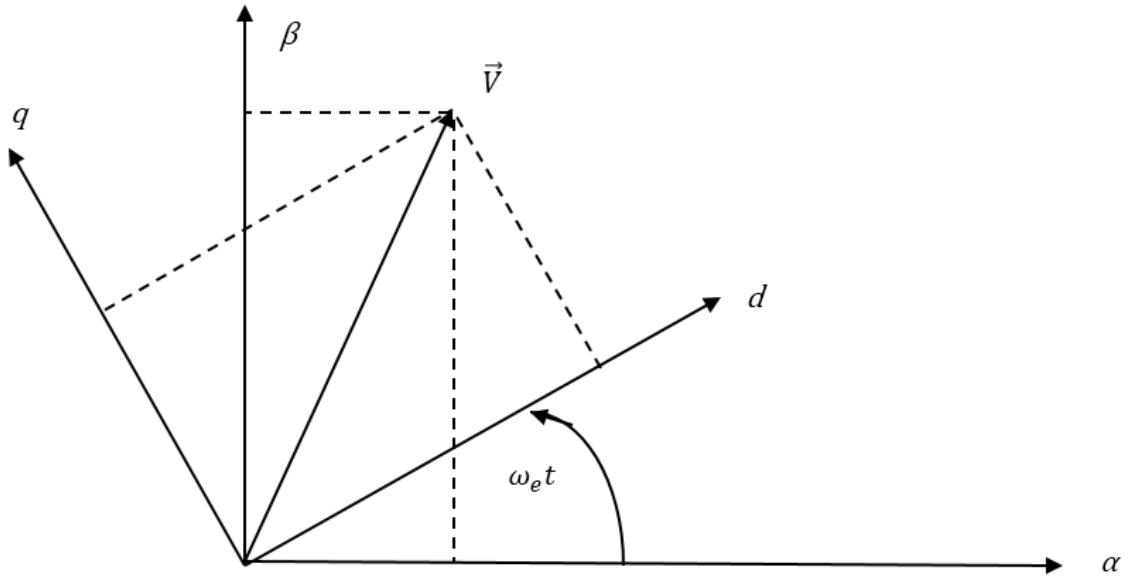

Figure 6: rotating d-q-axis in the stationary α − β plane

$$\vec{V_s}e^{j\omega_e t} - R_s\vec{i_s}e^{j\omega_e t} = \frac{d\vec{\lambda_s}e^{j\omega_e t}}{dt} = \frac{d(\vec{\lambda_s})}{dt}e^{j\omega_e t} + j\omega_e\vec{\lambda_s}e^{j\omega_e t} \quad (2.18)$$

$$V_d - R_s i_d = \frac{d\lambda_{sd}}{dt} - \omega_e\lambda_{sq} \quad (2.19)$$

$$V_q - R_s i_q = \frac{d\lambda_{sq}}{dt} + \omega_e\lambda_{sd} \quad (2.20)$$

$$V_s{}^2 = V_d{}^2 + V_q{}^2 \quad (2.21)$$

The d-axis is aligned with flux from the permanent magnet, therefore, the flux from the permanent magnet will only appear in the d-axis equations. The d-axis and q-axis flux terms are defined in equations 2.22 and 2.23. From equations 2.19 and 2.20 the equivalent circuits of a PMSG are illustrated in figure 7.

$$\lambda_{sd} = L_d i_d + \lambda_{pm} \quad (2.22)$$

$$\lambda_{sq} = L_q i_q \quad (2.23)$$

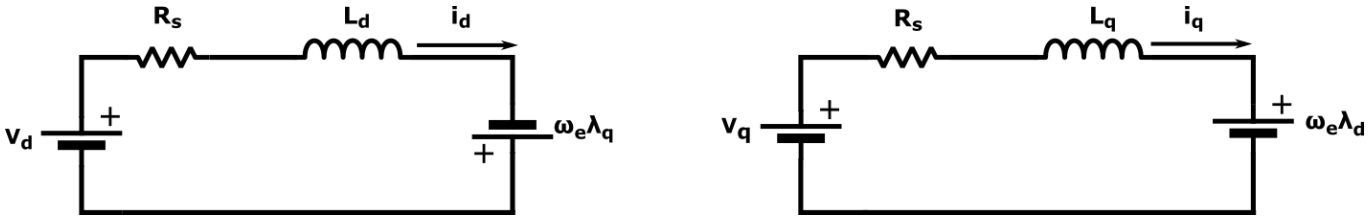

Figure 7: equivalent circuit model of the PMSG

To complete the electrical model of the PMSG an expression for the active and reactive power is given in equation 2.24 and 2.25 [45], [46].

$$P_G = v_{sd}i_{sd} + v_{sq}i_{sq} \tag{2.24}$$

$$Q_G = v_{sq}i_{sd} - v_{sd}i_{sq} \tag{2.25}$$

It must be noted that for an IPM the d-axis and q-axis inductances are not equal due to the its salient poles, this is not the case for an SPM. The mechanical model of a PMSG is given in equation 2.26 and 2.27. As a mechanical torque, T_m, is applied to the rotor of the PMSG, it is accelerated. The current induced in the stator develops an electromagnetic torque, T_e, acting in the opposite direction to the mechanical torque, decelerating the rotor [17].

$$J\frac{d\omega_e}{dt} = (T_e - T_m)p - B\omega_e \tag{2.26}$$

$$T_e = \frac{3}{2}p\left[\lambda_{pm} + \left(L_d - L_q\right)i_d\right]i_q \tag{2.27}$$

Since the d-axis and q-axis inductances are equal for a SPM the electromagnet torque is proportional to the q-axis current. The d-axis current does not influence the electromagnet torque and is often controlled to zero. An IPM, on the other hand, has a torque term that is attributed to the q-axis current and another torque term that is attributed to the product of the d-axis and q-axis currents. The latter is referred to as reluctance torque and gives the IPM greater control options at the cost of greater control complexity. A detailed description of the effect of the d-axis current on an IPM is given in [47].

The stator flux-linkage resulting from the d-axis current can increase or decrease the total flux-linkage in the stator. Consider equation 2.28, which describes the space vector voltage magnitude in figure 6.

$$V_s{}^2 = V_d{}^2 + V_q{}^2 \tag{2.28}$$

$$V_s{}^2 = r_s{}^2\left(i_d{}^2 + i_q{}^2\right) + 2\omega_r r_s\left(\lambda_d i_q - \lambda_q i_d\right) + \omega_r{}^2[\left(L_d i_d + \lambda_{pm}\right)^2 + \left(L_q i_q\right)^2 \tag{2.30}$$

$$V_s{}^2 = r_s{}^2 i_d{}^2 + \left(r_s{}^2 + \omega_r{}^2 L_q{}^2\right).\frac{4T_e{}^2}{9p^2\left[\lambda_{pm} + \left(L_d - L_q\right)i_d\right]^2} + \frac{4\omega_r}{3p}r_s T_e + \omega_r{}^2\left(L_d i_d + \lambda_{pm}\right)^2 \tag{2.31}$$

$$\omega_{r0} = \frac{\sqrt{V_s{}^2 - r_s{}^2 i_d{}^2}}{L_d i_d + \lambda_{pm}} \tag{2.32}$$

In the case of no load where $T_e \rightarrow 0$, equation 2.31 simplifies to equation 2.32. As the speed of the PMSG increases the rate of change of the flux-linkage in the stator increases, resulting in a higher induced EMF. To control a PMSG with a high induced EMF, a high stator terminal voltage is required. However, equation 2.32 implies that decreasing i_d will speed up the PMSG without changing the stator terminal voltage. According to equation 2.23, varying the d-axis current in the negative direction decreases the flux-linkage in the stator and in turn decreases the induced EMF. Hence, smaller stator terminal voltages can be used for control of the PMSG. As a result, the likelihood of inverter saturation is reduced and the constant power region of the PMSG is extended. This is referred to as field weakening. Figure 8 shows a vector diagram of stator quantities.

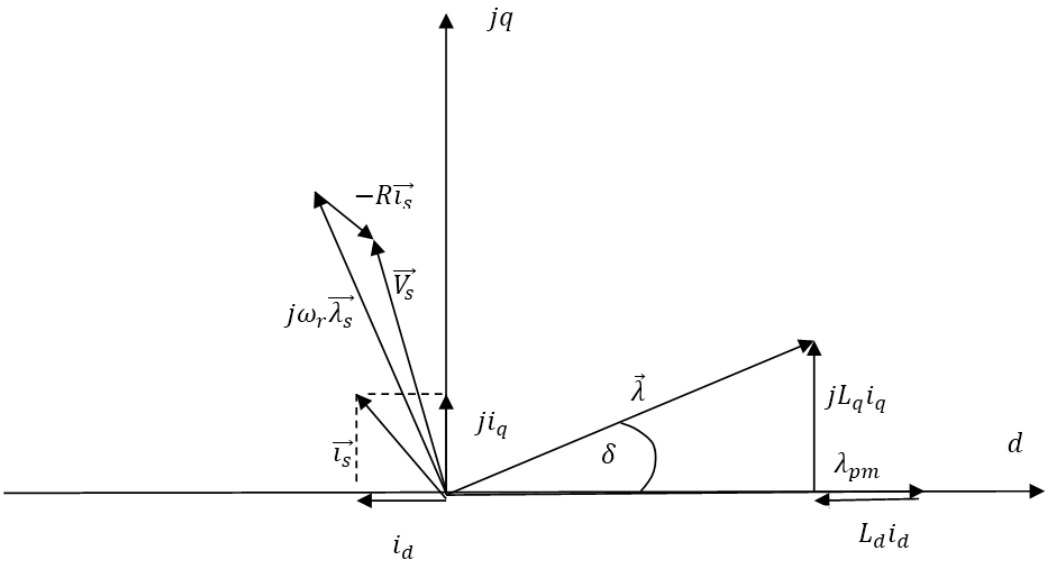

Figure 8: vector diagram of a PMSG

2.4 Load-side model

In this section the load-side model of the system is developed. The model will represent the load-side when it is in both grid-tied and isolated modes of operation.

The type of filter used between converter and load determines the dynamic behaviour of the load-side currents. Filters comprising of just an inductor are referred to as L-filters, and have been used extensively in the past due of their simple design and low control complexity. L-filters are first order filters and thus a significant inductance is often required for adequate attenuation of switching harmonics. As a result, L-filters are bulky and will increase conduction losses, particularly in high power applications. From a control perspective, L-filters

make for a slow dynamic behaviour of load-side currents. Modern applications require LCL-filters due to smaller component sizes and higher attenuation of switching harmonics when compared to L and LC-filters. The LCL-filter is a third order filter which requires smaller inductance values than lower order filters. The transfer function of an LCL-filter is given in equation 2.33. It can be deduced that there exists a resonance frequency ω_{res} where the impedance to the current is zero, causing the current to increase uncontrollably. Figure 9 shows bode plots of an L and LCL-filter that are comprised of the same inductance. The behaviour of both filters at low frequency is similar; their magnitudes rolls off at 20dB per decade as the frequency approaches the resonance frequency. After the resonance spike, the magnitude of the LCL-filter rolls off at 60db per decade. The result is higher order frequencies associated with switching harmonics are attenuated more, for an LCL-filter. Therefore, the dominant dynamic behaviour of the load-side currents is like that of a filter consisting of just the two inductances L_{f1} and L_{f2}, which are smaller than the inductances which would typically be used in an L-filter.

$$H_{LCL} = \frac{i_g}{v_{in}} = \frac{1}{\left(L_{f1} + L_{f2}\right)s + C_f L_{f1} L_{f2} s^3} \tag{2.33}$$

$$\omega_{res} = \sqrt{\frac{L_{f1} + L_{f2}}{C_f L_{f1} L_{f2}}} \tag{2.34}$$

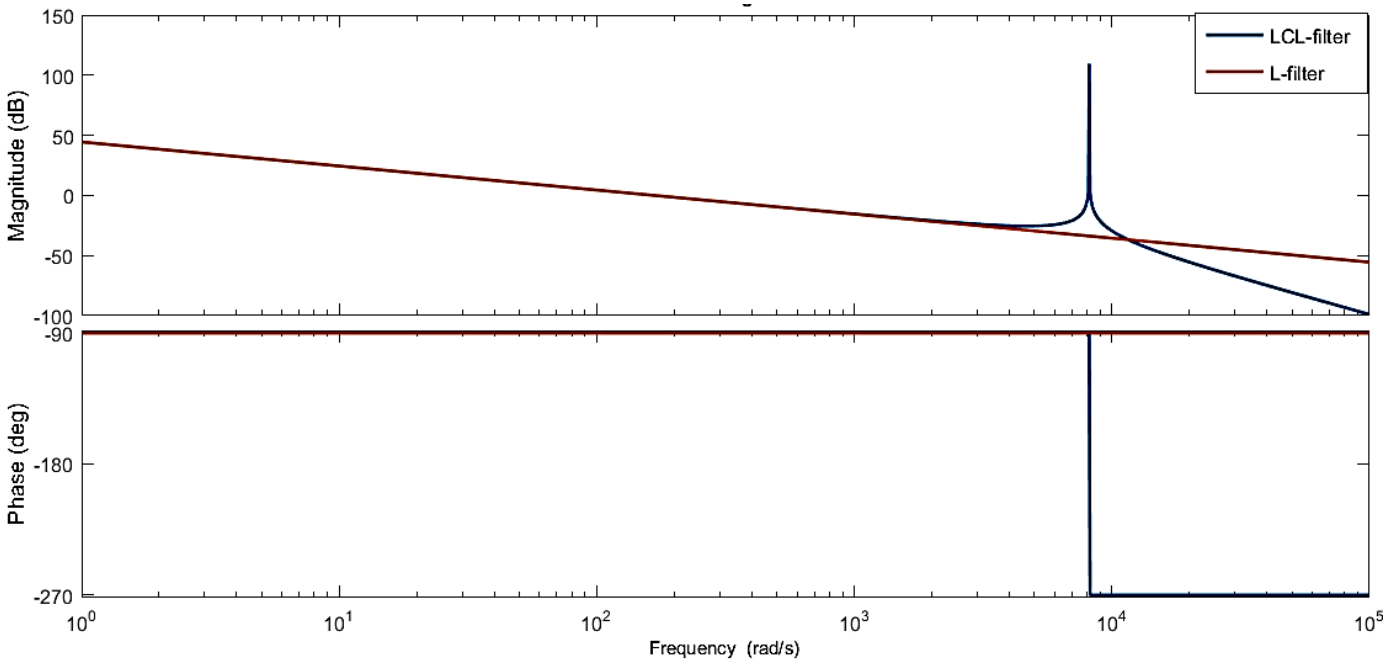

Figure 9: Bode diagram of an L and LCL-filter

The resonance spike poses a control problem because unlike and L-filter, the LCL-filter is not globally stable. Damping techniques are used to reduce the magnitude of the spike; they fall into two categories: active and passive damping. Active damping involves monitoring of the filter capacitor current or voltage in figure 10. Its objective is to add an s^2 term in the denominator of equation 2.33 by controlling the filter capacitor current. This gives a damped current response. The filter capacitor current and voltage is usually measured with a sensor, but estimation techniques can be employed that eliminate the need for a sensor. The success of the estimation techniques depends on the accuracy of the model used. Inductor values vary according to the amount of current they are conducting; therefore, estimation techniques may be difficult to implement practically. A review of active damping techniques is provided in [48]. Passive damping involves physically adding the s^2 term by placing a resistor R_f in series with the filter capacitor as shown in figure 10.

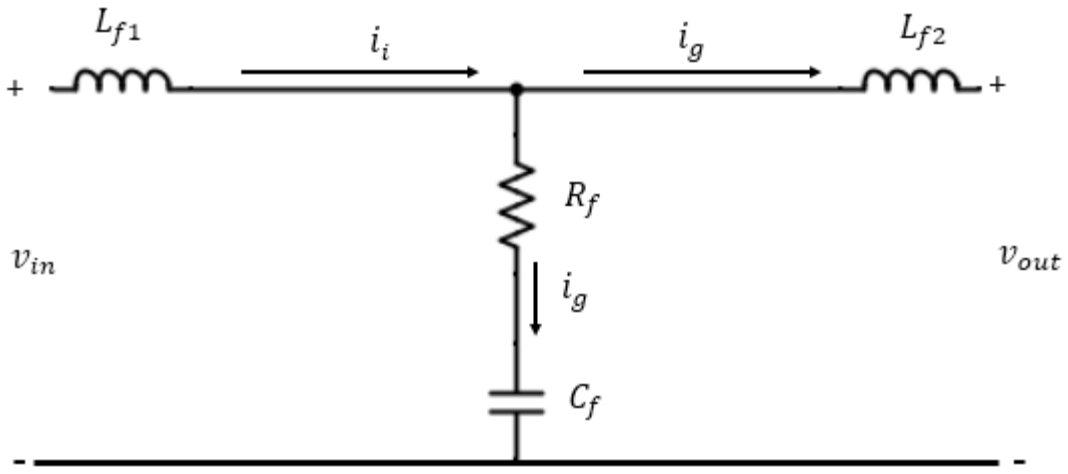

Figure 10: LCL-filter topology

This changes the transfer function of the LCL-filter to equation 2.35. The resistor must be chosen depending on the damping factor required as well as to minimize the conduction losses in the resistor. Figure 11 illustrates that large damping resistors minimise the effects of resonance. However, the gain margin of the LCL-filter is still negative which indicates instability. To ensure stability, several design considerations must be undertaken; they include the placement of the resonance peak, the determination of the damping resistor, and the determination of the bandwidth of the load-side system.

$$H_{LCL} = \frac{1}{(L_{f1} + L_{f2})s + (L_{f1} + L_{f2})C_f R_f s^2 + C_f L_{f1} L_{f2} s^3} \tag{2.35}$$

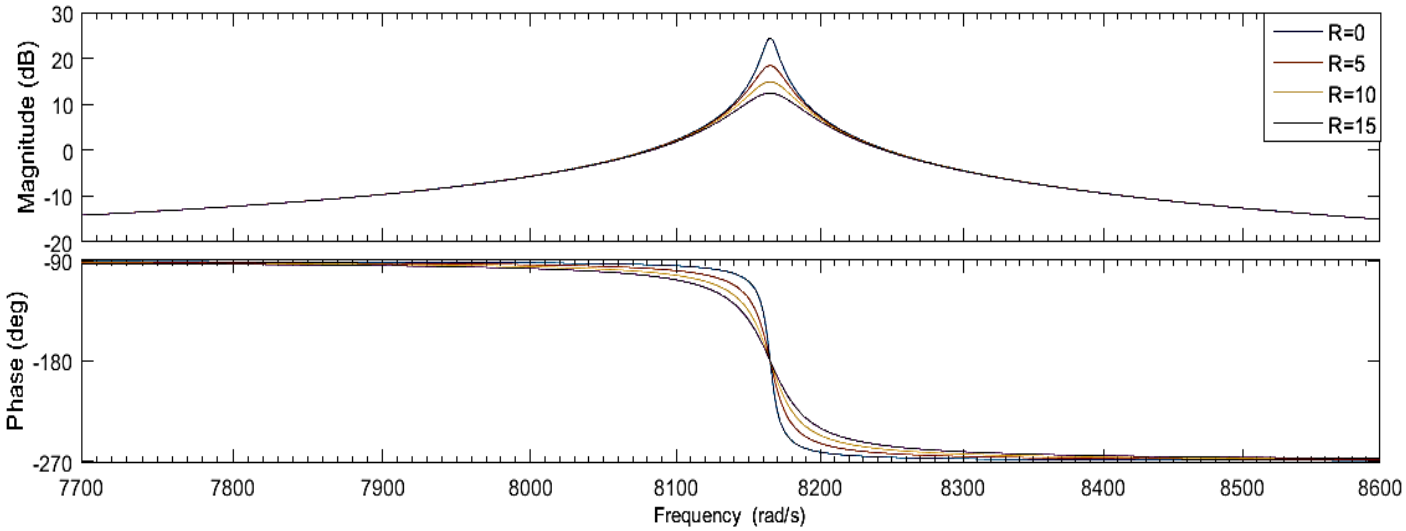

Figure 11: Effect of damping resistor on the bode plot of an LCL-filter

Figure 9 demonstrates that at low frequencies the behaviour of an L and LCL-filter is similar. Therefore, by limiting the bandwidth of the load-side system to frequencies lower than the resonance frequency the dynamic behaviour of the system can be approximated as a first order system. In the same manner as in section 2.3, the space vector representation of the load-side is given by equation 2.36.

$$\overrightarrow{e_g}e^{j\omega_g t} = \frac{d\overrightarrow{\lambda_f}e^{j\omega_g t}}{dt} + R\overrightarrow{i_g}e^{j\omega_g t} + \vec{V}e^{j\omega_g t} \tag{2.36}$$

The d-axis and q-axis equations of the load side are given below. The magnitude of the load voltage is e_{gd}, the q-axis component is zero. In isolated operation, the voltage across the load will decrease to zero should the load-side converter fail to regulate it. The d-axis and q-axis currents determine the active and reactive powers respectively.

$$\frac{d\lambda_{fd}}{dt} = -e_{gd} - \omega_g\lambda_q + R_f i_d + V_d \tag{2.37}$$

$$\frac{d\lambda_{fq}}{dt} = -\omega_g\lambda_d - R_f i_q - V_q \tag{2.38}$$

$$\lambda_{fd} = \lambda_{fq} = Li_d = Li_q = (L_{f1} + L_{f2})i_d = (L_{f1} + L_{f2})i_q \tag{2.39}$$

$$P_{load} = \frac{3}{2}v_{sd}i_{sd} \tag{2.40}$$

$$Q_{load} = \frac{3}{2}v_{sd}i_{sq} \tag{2.41}$$

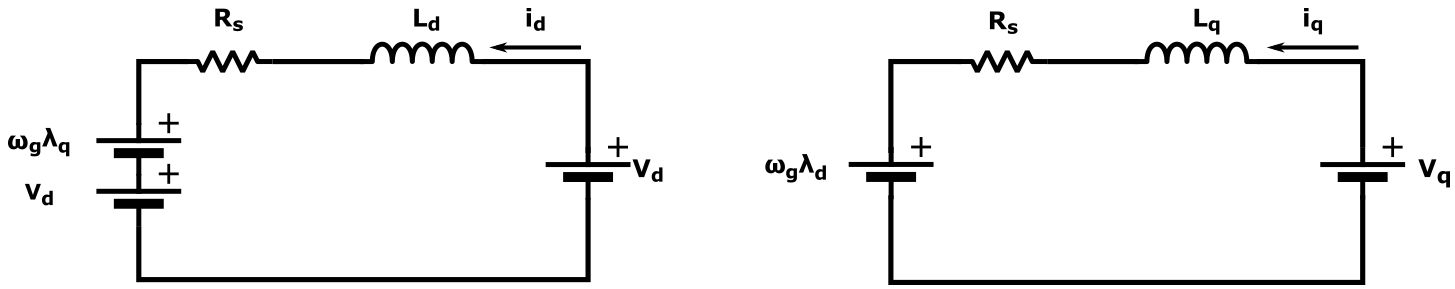

Figure 12: load-side equivalent circuit

The DC-link voltage of the converter is determined by the difference in the power flow to and from itself. Equation 2.42 describes the relationship between the generator-side and load-side currents with the DC-link voltage and current respectively [49].

$$i_{dc} - \frac{3}{2}(s_q i_q + s_d i_d) = C\frac{d}{dt}V_{dc} \tag{2.42}$$

Chapter 3

3. Control of a gas turbine generator

The vector control of an IPM is discussed extensively in this chapter before simulations are carried out in chapter 4. Methods of frequency synchronization on the generator-side and load-side systems are discussed first. Generator parameters are then determined and an LCL-filter for load integration is designed. Vector control is achieved through a cascaded PI controller structure. After which, the main control strategies that can be implemented on an IPM are discussed and proven.

3.1 Synchronisation

3.1.1 Generator Synchronisation

Vector control requires that three-phase quantities be transformed to their space vector equivalents and then into d-axis and q-axis quantities. Only then can control technique be implemented. To achieve this, the angle of the space vector must be made available, which is an integer multiple of the rotor angle. The angle of the generator can be determined with a use of a sensor or 'sensorless' analytical methods. Sensorless methods can be classified in to those that estimate the induced EMF of the PMSG and those that use high frequency signal injection to determine the rotor angle [50]. Estimation of the induced EMF will show poor performance at low speeds due to the low induced EMF. On the other hand, methods involving signal injection can operate throughout the whole speed range of the generator. Both methods make use of the model of PMSG which can become inaccurate under different speeds, temperatures and loading. Methods involving sensors to determine the rotor angle of the generator include the use of hall effect sensors, resolvers and encoders. For this work an incremental encoder is employed.

The Incremental quadrature encoder outputs three pulses as shown in figure 13. The A and B pulses are 90 degrees out of phase. A simple logic table can be used to decode the phase of the encoder. An increase in the value of the phase indicates movement in the clockwise direction and a decrease indicates a movement in the opposite direction. The Z pulse indicates the 'zero' position of the encoder, from this point the rotor angle can be calculated.

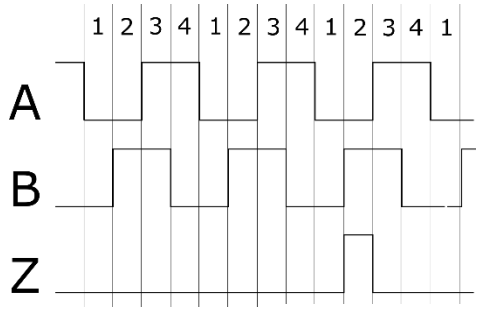

Phase	A	B
1	0	0
2	0	1
3	1	1
4	1	0

Figure 13:Encoder pulse traces

3.1.2 Load-side synchronisation

The grid angle is required for the d-q transformation on the load-side of the system. The usual method of obtaining the grid angle is with use of a Phase-locked loop (PLL). In [51], a comparison of popular algorithms of Synchronous Reference-Frame (SRF) PLL's is presented. It is shown that most PLL's have a similar structure, with additional features that add to the robustness of the algorithm. The SRF-PLL works by initially estimating the grid angle and performing a d-q transformation on the measured grid voltages. Subsequent grid angles are determined by choosing a grid angle that forces the q-component of the grid voltage to zero; this is achieved with a PI controller. A simple SRF-PLL is illustrated in figure 14.

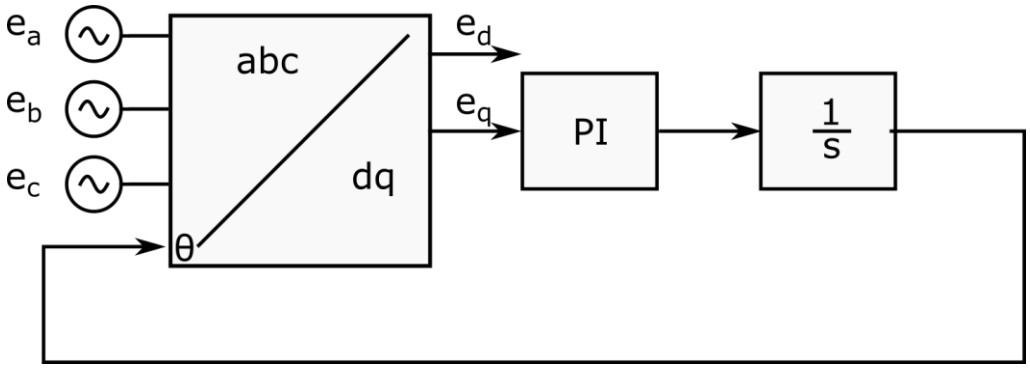

Figure 14: SRF-PLL

The SRF-PLL does not require any grid parameters and has a simple structure, which makes it a popular choice for grid synchronization. Figure 15 (a) illustrates the typical output of the SRF-PLL. The q-axis of the voltage is zero and the d-axis voltage takes the value of the peak of the grid's phase voltage. The SRF-PLL works best for a balanced 3-phase system. This is illustrated in figure 15 (b) where a magnitude unbalance of 6% and 16% is introduced on two of the grid voltage phases. Such an unbalance can be represented by a set of balanced positive sequence grid voltages, and a set of balanced negative sequence voltages which rotate in

opposite directions in the alpha-beta plane. The SRF-PLL locks on to the positive sequence voltage, however within the synchronous positive sequence references-frame, a negative sequence component oscillating at twice the grid frequency will exist. The oscillation will propagate throughout all the d-q transformations and can cause control issues.

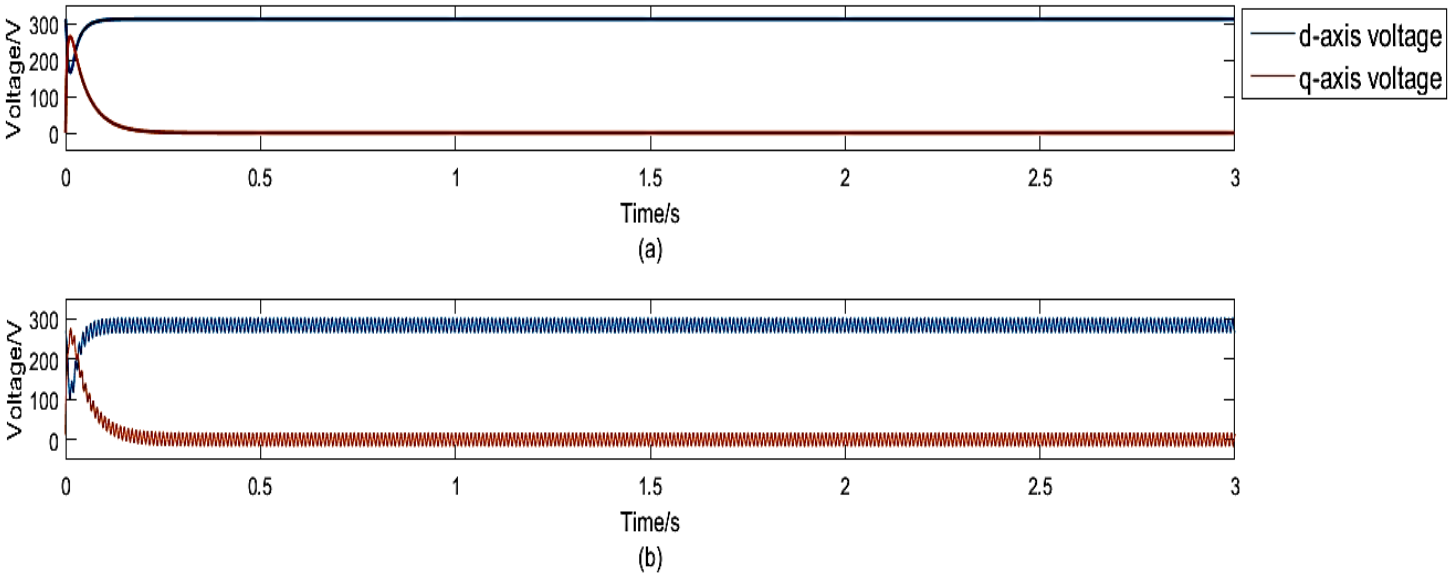

Figure 15:(a) d-q grid voltages under balanced conditions. (b) d-q grid voltages under unbalanced conditions

A method of extracting the positive and negative sequence synchronous components is developed next. Extraction of positive and negative sequence components is required for the implementation of control during grid voltage unbalance. The recursive least squares (RLS) algorithm, that can be found in [52], [53] is used for this purpose.

Consider a vector $\boldsymbol{y}$ of measured outputs, where $\boldsymbol{\varphi}$ represents the input data matrix and $\boldsymbol{\theta}$ represents a matrix of unknown parameters. The vector $\boldsymbol{n}$ represents random disturbances that are unmodeled.

$$\boldsymbol{y} = \boldsymbol{\varphi\theta} + \boldsymbol{n} \tag{3.1}$$

More than often, system parameters are unknown and must be estimated $\widehat{\boldsymbol{\theta}}$ to map an input data matrix to an output vector. The result is an output estimate $\widehat{\boldsymbol{y}}$ which can be compared to the true output $\boldsymbol{y}$ of the system after each estimation. The difference between the estimate and the true value is the error $\boldsymbol{e}$.

$$\widehat{\boldsymbol{y}} = \boldsymbol{\varphi}\widehat{\boldsymbol{\theta}} \tag{3.2}$$

$$\boldsymbol{e} = \boldsymbol{y} - \boldsymbol{\varphi}\widehat{\boldsymbol{\theta}} \tag{3.3}$$

The least squares algorithm involves squaring an error vector $\boldsymbol{e}$ and finding a set of parameters that will minimise the square of the error vector. Appendix A provides a list of identities related to the derivatives of matrices that are used in the following equations.

$$C = \boldsymbol{e^T e} = \left(\boldsymbol{y} - \boldsymbol{\varphi}\widehat{\boldsymbol{\theta}}\right)^T \left(\boldsymbol{y} - \boldsymbol{\varphi}\widehat{\boldsymbol{\theta}}\right) \tag{3.4}$$

$$C = \boldsymbol{y^T y} - \boldsymbol{y^T \varphi}\widehat{\boldsymbol{\theta}} - \widehat{\boldsymbol{\theta}}^{\boldsymbol{T}}\boldsymbol{\varphi^T y} + \widehat{\boldsymbol{\theta}}^{\boldsymbol{T}}\boldsymbol{\varphi^T \varphi}\widehat{\boldsymbol{\theta}} \tag{3.5}$$

$$\frac{dC}{d\hat{\theta}} = -2\boldsymbol{\varphi^T y} + 2\boldsymbol{\varphi^T \varphi}\widehat{\boldsymbol{\theta}} = 0 \tag{3.6}$$

$$\widehat{\boldsymbol{\theta}} = (\boldsymbol{\varphi^T \varphi})^{-1}\boldsymbol{\varphi^T y} \tag{3.7}$$

The parameter vector that minimises the error is provided in equation 3.7. This form of the least squares uses batch processing, which considers all the previously available data to calculate the parameter matrix. The consequence of batch processing is a high computation effort and long processing times. Recursive least squares algorithm was developed to address this shortcoming.

The idea behind recursive least squares is that by calculating the parameter vector after every iteration in time, the next iteration of parameters $\widehat{\boldsymbol{\theta}}(k+1)$ can be calculated from the data from the current error based on the k^{th} parameter estimation. The previous equations are discretized and fundamental vectors are defined in equations 3.8-3.12.

$$\boldsymbol{P}(k) = (\boldsymbol{\varphi}^{\boldsymbol{T}}(k)\boldsymbol{\varphi}(k))^{-1} \tag{3.8}$$

$$\widehat{\boldsymbol{\theta}}(k) = \boldsymbol{P}(k)\boldsymbol{\varphi}^{\boldsymbol{T}}(k)\boldsymbol{y}(k) \tag{3.9}$$

$$\boldsymbol{y}(k) = \begin{pmatrix} \boldsymbol{y}(1) \\ \boldsymbol{y}(2) \\ \vdots \\ \boldsymbol{y}(k) \end{pmatrix} \tag{3.10}$$

$$\boldsymbol{\varphi}(k) = \begin{pmatrix} \boldsymbol{\varphi}(1) \\ \boldsymbol{\varphi}(2) \\ \vdots \\ \boldsymbol{\varphi}(k) \end{pmatrix} \tag{3.11}$$

$$\boldsymbol{P}(k) = [(\boldsymbol{\varphi}^{\boldsymbol{T}}(1)\boldsymbol{\varphi}(1) + (\boldsymbol{\varphi}^{\boldsymbol{T}}(2)\boldsymbol{\varphi}(2) + \cdots + (\boldsymbol{\varphi}^{\boldsymbol{T}}(k)\boldsymbol{\varphi}(k)]^{-1} \tag{3.12}$$

From equation 3.10 and 3.11 an expression for the parameter estimation for the $(k+1)^{th}$ iteration is defined in equation 3.13.

$$\widehat{\boldsymbol{\theta}}(k+1) = \boldsymbol{P}(k+1)\left(\boldsymbol{\varphi}^{\boldsymbol{T}}(k)\boldsymbol{y}(k) + \boldsymbol{\varphi}^{\boldsymbol{T}}(k+1)\boldsymbol{y}(k+1)\right) \tag{3.13}$$

$$\boldsymbol{P}(k)^{-1}\widehat{\boldsymbol{\theta}}(k) = \boldsymbol{\varphi}^{\boldsymbol{T}}(k)\boldsymbol{y}(k) \tag{3.14}$$

Equation 3.9 is rearranged to form equation 3.14. The result is inserted into equation 3.13.

$$\widehat{\boldsymbol{\theta}}(k+1) = \widehat{\boldsymbol{\theta}}(k) + (\boldsymbol{P}(k+1)\boldsymbol{P}(k)^{-1} - \boldsymbol{I})\widehat{\boldsymbol{\theta}}(k) + \boldsymbol{P}(k+1)\boldsymbol{\varphi}^{\boldsymbol{T}}(k+1)\boldsymbol{y}(k+1)) \tag{3.15}$$

From equation 3.12, equation 3.16 can be derived and then inserted into equation 3.15.

$$\boldsymbol{P}(k)^{-1} = \boldsymbol{P}(k+1)^{-1} - \boldsymbol{\varphi}^{\boldsymbol{T}}(k+1)\boldsymbol{\varphi}(k+1) \tag{3.16}$$

$$\widehat{\boldsymbol{\theta}}(k+1) = \widehat{\boldsymbol{\theta}}(k) - \boldsymbol{P}(k+1)\boldsymbol{\varphi}^{\boldsymbol{T}}(k+1)\boldsymbol{\varphi}(k+1)\widehat{\boldsymbol{\theta}}(k) + \boldsymbol{P}(k+1)\boldsymbol{\varphi}^{\boldsymbol{T}}(k+1)\boldsymbol{y}(k+1) \tag{3.17}$$

The result is an expression for the current estimation of parameters based on the previous estimation.

$$\widehat{\boldsymbol{\theta}}(k+1) = \widehat{\boldsymbol{\theta}}(k) + \boldsymbol{P}(k+1)\boldsymbol{\varphi}^{\boldsymbol{T}}(k+1)\left[\boldsymbol{y}(k+1) - \boldsymbol{\varphi}(k+1)\widehat{\boldsymbol{\theta}}(k)\right] \tag{3.18}$$

It is reiterated here that unbalanced three phase voltages can be represented as a sum of balanced three phase positive and negative sequence voltages. Equation 3.19 maps alpha-beta grid voltages to their symmetrical counterparts through a modified inverse Park's transform. Note that the transformation includes positive and negative sequence synchronous voltages.

$$\begin{bmatrix} e_\alpha \\ e_\beta \end{bmatrix} = \begin{bmatrix} \cos(\theta) & -\sin(\theta) & \cos(\theta) & \sin(\theta) \\ \sin(\theta) & \cos(\theta) & -\sin(\theta) & \cos(\theta) \end{bmatrix} \begin{bmatrix} e_d^+ \\ e_q^+ \\ e_d^- \\ e_q^- \end{bmatrix} \tag{3.19}$$

The structure of equation 3.19 is the same as the one in equation 3.1. The objective of the algorithm will be to estimate future values of the grid voltage. The estimated grid voltages will then be compared to the measured grid voltages once they become available. Since future quantities are estimated, an incremental component of the model is added to equation 3.19. The incremental part is given in equation 3.20 and the full model is given equation 3.22.

$$\begin{bmatrix} \delta e_\alpha \\ \delta e_\beta \end{bmatrix} = \frac{\partial}{\partial \theta} \begin{bmatrix} \cos(\theta) - \sin(\theta) + \cos(\theta) + \sin(\theta) \\ \sin(\theta) + \cos(\theta) - \sin(\theta) + \cos(\theta) \end{bmatrix} \delta\theta \tag{3.20}$$

$$\begin{bmatrix} e_{\alpha+1} \\ e_{\beta+1} \end{bmatrix} = \begin{bmatrix} e_{\alpha} \\ e_{\beta} \end{bmatrix} + \begin{bmatrix} \delta e_{\alpha} \\ \delta e_{\beta} \end{bmatrix} \tag{3.21}$$

$$\begin{bmatrix} e_{\alpha+1} \\ e_{\beta+1} \\ \delta\theta \end{bmatrix} = \begin{bmatrix} \cos(\theta) & -\sin(\theta) & \cos(\theta) & \sin(\theta) & -2\sin(\theta) \\ \sin(\theta) & \cos(\theta) & -\sin(\theta) & \cos(\theta) & -2\sin(\theta) \\ 0 & 0 & 0 & 0 & 1 \end{bmatrix} \begin{bmatrix} e_d^+ \\ e_q^+ \\ e_d^- \\ e_q^- \\ \delta\theta \end{bmatrix} \tag{3.22}$$

The positive and negative sequences are estimated by comparing measured alpha-beta voltage to the estimated ones.

$$\hat{\theta} = \begin{bmatrix} \widehat{e_d^+} \\ \widehat{e_q^+} \\ \widehat{e_d^-} \\ \widehat{e_q^-} \\ \widehat{\delta\theta} \end{bmatrix} \quad \varphi = \begin{bmatrix} \cos(\theta) & -\sin(\theta) & \cos(\theta) & \sin(\theta) & -2\sin(\theta) \\ \sin(\theta) & \cos(\theta) & -\sin(\theta) & \cos(\theta) & -2\sin(\theta) \\ 0 & 0 & 0 & 0 & 1 \end{bmatrix} \tag{3.23}$$

$$e = \begin{bmatrix} e_a \\ e_b \\ \delta\theta \end{bmatrix} - \varphi\hat{\theta} \tag{3.24}$$

The positive and negative sequence grid angles can be obtained through an arctangent function using the alpha-beta voltages, for use in a Park's transforms. The algorithm does not make use of any system parameters, which adds to the algorithm's robustness. This method can also be extended to include phase shifts in the grid voltages since any periodic signal can be decomposed into a sum of sinusoids. However, the focus of this work is limited to grid voltage magnitude unbalance.

When grid voltage magnitudes are balanced, the positive sequence components in figure 16(a) are the same as those in 15 (a). In addition, the negative sequence synchronous components in 16(b) are zero. Figures 16 (c) and (d) show the successful extraction of positive and negative sequence synchronous components during unbalanced grid voltage conditions. The d-axis positive sequence grid voltage component takes on a value slightly below the rated value, while the negative sequence components take on non-zero values.

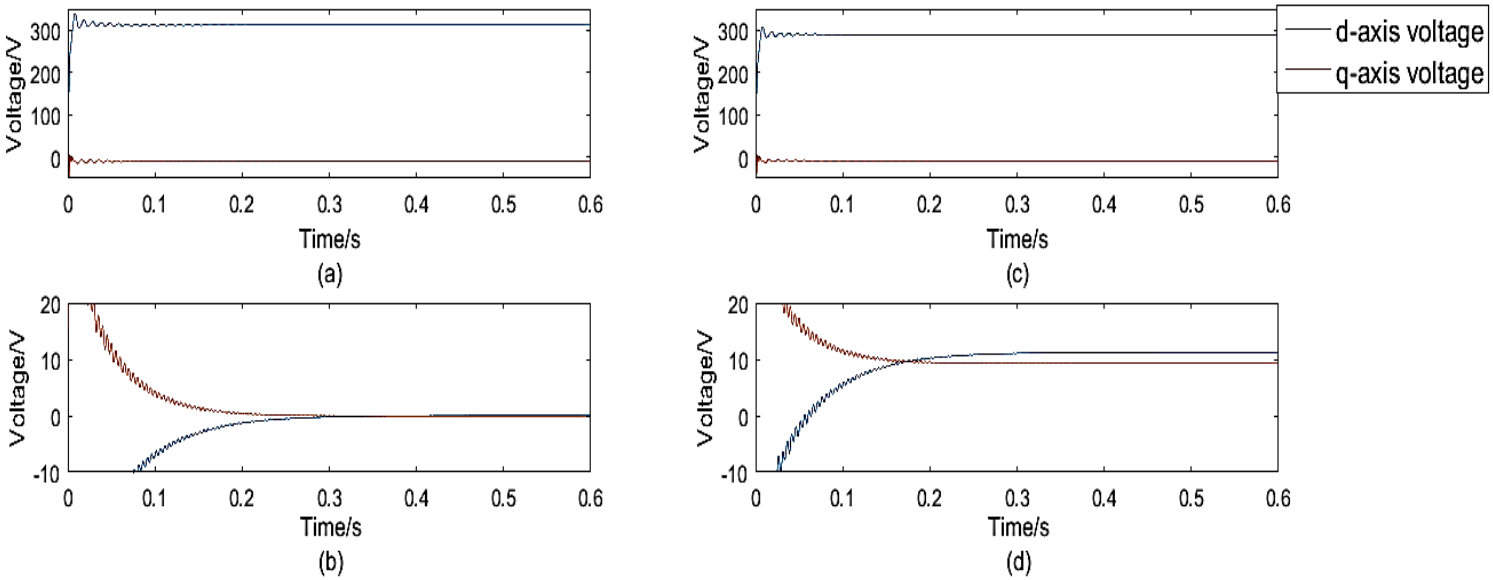

Figure 16:(a) Positive sequence d-axis and q-axis grid voltages during balanced conditions (b) Negative sequence d-axis and q-axis grid voltages during balanced conditions (c) Positive sequence d-axis and q-axis grid voltages during unbalanced conditions (d) Negative sequence d-axis and q-axis grid voltages during unbalanced conditions

This method requires no grid parameters and very little tuning. The benefits of this method come at a cost of high computation, as several matrices are inverted and multiplied. Fast FPGA's, which can perform multiple operations in parallel will see computation time decrease significantly for such applications.

3.2 Generator parameter determination and LCL-filter design

Controllers are designed according to the parameters of the system. In this section, the parameters of the IPM are determined experimentally. The LCL-filter is then designed. Finally, the controllers for the generator-side and load-side are designed.

3.2.1 Generator parameter determination

A review of methods of determining the synchronous inductances is provided in [54]. In this work, a DC current is stepped though the stator windings to determine the d-axis and q-axis parameters. The time taken for the current to reach 63% of its steady state value is called the electrical time constant. The time constant can be used to calculate the system parameters. The configurations of the experiments are illustrated in figure 17. This method is accurate and simple to implement, which makes it a popular method of determining generator parameters.

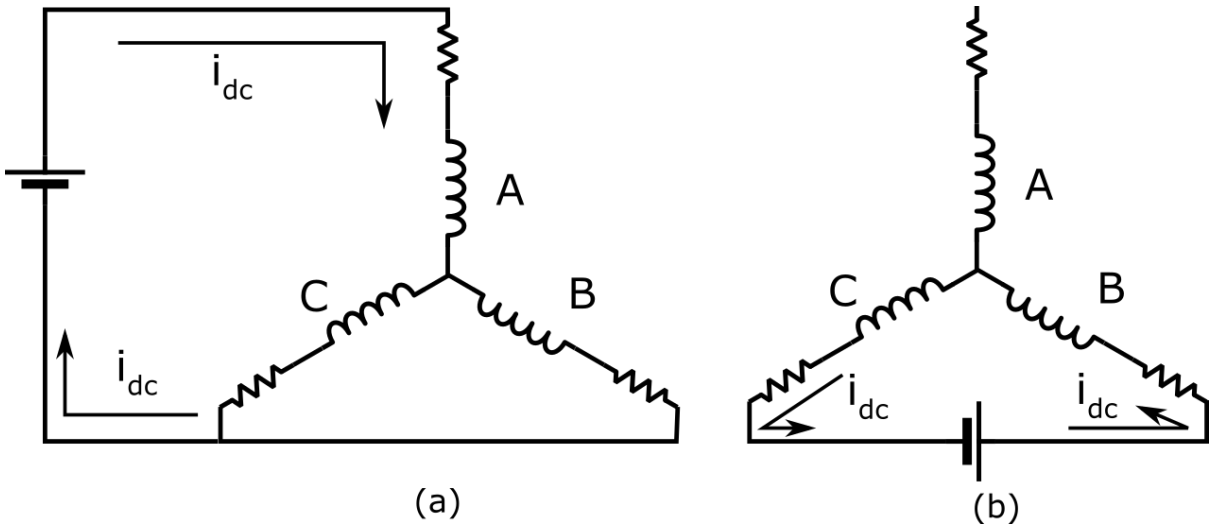

Figure 17: (a) Configuration to determine d-axis inductance (b) Configuration to determine q-axis inductance

The basic transfer function for the stator current of a PMSG is given in equation 3.25. The d-axis and q-axis electrical time constants of the stator are a ratio of the synchronous inductances to the stator resistance. To determine the synchronous inductances, the stator resistance is firstly measured using an ohmmeter. Next, the circuits in figure 17 experience a step increase or decrease in stator current. The time it takes the current to reach 63% of its steady state value τ_{dq}, is recorded. According to equation 3.25, once the time constants and the stator resistance are determined, the synchronous inductances can then be calculated. The generator parameters are given in table 2.

$$i_{dq} = \frac{1}{1 + s\frac{L_{dq}}{R}} = \frac{1}{1 + s\tau_{dq}} \tag{3.25}$$

Table 2: IPM parameters

Time constant	Resistance	Synchronous inductance
$\tau_d = 0.015s$	5Ω	$L_d = 0.075$
$\tau_q = 0.024s$	5Ω	$L_q = 0.120$

Next, the magnet flux-linkage must be determined to fully represent the total flux-linkage in the stator of the PMSG according to equation 2.22. The induced EMF in the stator terminals is proportional to the speed of the generator. This can be deduced from equation 2.20 where the q-axis stator equation becomes equation 3.26 for no load conditions. The generator speed is gradually increased at no load while the stator voltage is measured. The constant of

proportionality is the magnetic flux-linkage. The generator is driven from 0rad/s to 114rad/s, the voltage induced is shown in figure 18. The slope of the graph represents the magnetic flux-linkage in the PMSG.

$$V_q = \omega_e \lambda_{sd} \tag{3.26}$$

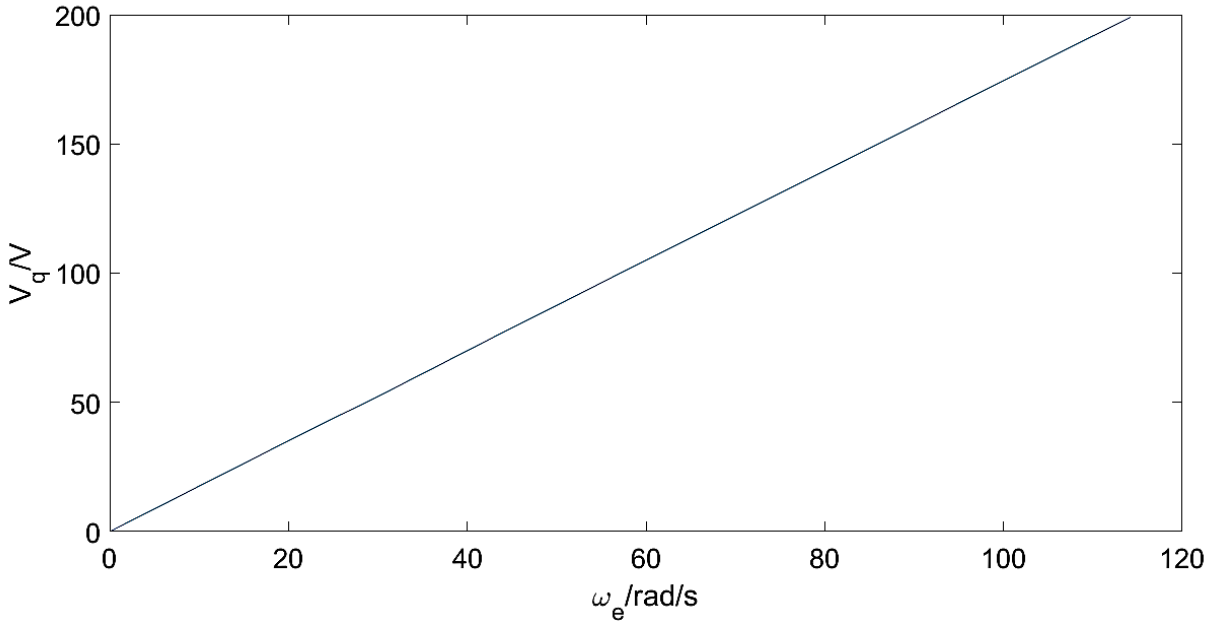

Figure 18: Induced stator voltages at different generator speeds

$$\lambda_{pm} = 1.75Wb \tag{3.27}$$

3.2.2 LCL-filter design

LCL-filters must be designed to optimise the filter performance while minimising filter component sizes, reactive power production, switching losses and conduction loses. Large inductances must be avoided as this will result in significant impedances at low frequencies. Consequently, large converter voltages will be required to drive current through the high impedance. The large changes in voltage levels that will result when switching, reduces the lifetime of the switches and increase switching loses. A large DC-link voltage may also be required to achieve the high converter voltages, which could result in the need for a larger DC-link capacitor. The filter capacitor size must also be kept as low as possible. A large LCL-filter capacitor is not desirable because it becomes a source of reactive power [36], [55].

Selection of the filter components determines the resonance frequency according to equation 2.34. The resonance frequency must not be contained within the bandwidth of the load-side

system to avoid instability. The bandwidth of the system is not easily determined, as it is dependent on the controller parameters in addition to the filter components. Most literature will estimate the bandwidth of the load-side system to be 10 times the grid frequency. The switching frequency must be greater than the resonance frequency for greater attenuation of switching harmonics along the 60dB/decade slope. Secondly, the sampling frequency must be at least twice the resonance frequency according to the Nyquist criterion. This is done so that the resonance frequency is not aliased. Symmetrical switching is used in this work; thus, the switching frequency and the sampling frequency are the same. A comprehensive discussion on synchronous switching is presented in section 5.5. Equation 3.28 shows the limits that are imposed by the Nyquist criterion on the system bandwidth, resonant frequency and switching frequency.

$$f_b < f_{res} < \frac{f_{sw}}{2} \tag{3.28}$$

The selection of the filter capacitor is usually done to limit the production of reactive power to below 5% of the base value. This leaves the designer with the task of determining the inductor values. Equation 2.34 is rearranged to give equation 3.29 [36].

$$C_f(L_{f1} + L_{f2}) = \frac{\left(\frac{f_{sw}}{f_{res}}\right)^2}{4\pi^2 f_{sw}^2} \cdot \frac{\left(1 + \frac{L_{f2}}{L_{f1}}\right)^2}{\frac{L_{f2}}{L_{f1}}} = \frac{k^2}{4\pi^2 f_{sw}^2} \cdot \frac{(1+\mu)^2}{\mu} \tag{3.29}$$

The aim of the design is to reduce $C_f(L_{f1} + L_{f2})$ as much as possible. In figure 19, k is set to 2 and the switching frequency is 4kHz. For an arbitrary filter capacitor and inductors, the value of μ that minimises $C_f(L_{f1} + L_{f2})$ is 1. Thus, a strong argument can be made for making L_{f1} and L_{f2} equal, which result when μ is 1.

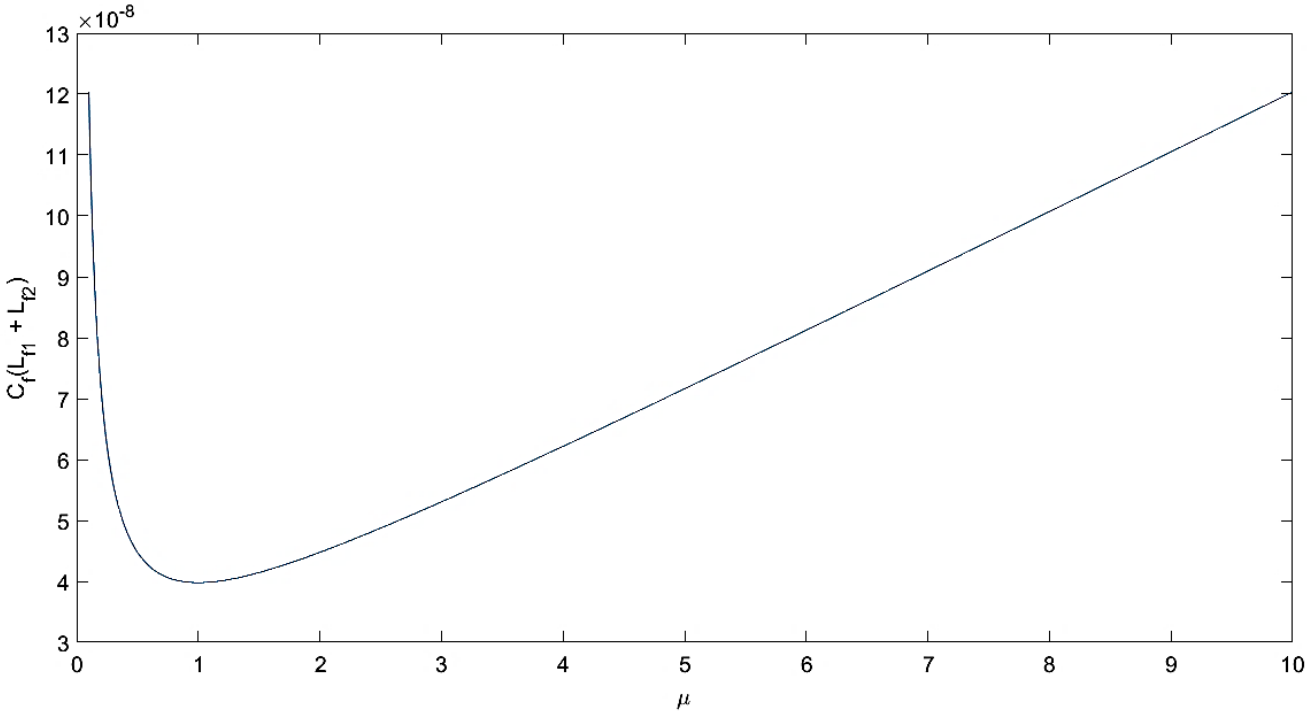

Figure 19: The effect of μ on filter component size

For an accelerated design process, some designers will place the resonance frequency at the geometric mean of the system bandwidth and the switching frequency [36], [56]. This ensures that the resonance frequency does not fall within the system bandwidth and that aliasing of the resonance peak does not occur. However, by predetermining the resonance frequency, certain design criteria may not be met because of the limited inductor and capacitor values one can chose from. One such design criteria involves keeping the total inductance of the filter below 10% of the base inductance of the system [57]. The base values are calculated from the load power P, the line-to-line RMS voltage of the grid and the grid frequency ω_g. The base quantities and maximum permissible component values are given in table 2.

$$Z_b = \frac{\bar{e}_{gLL}{}^2}{P} \tag{3.30}$$

$$L_b = \omega_g Z_b \tag{3.31}$$

$$C_b = \frac{1}{\omega_g} Z_b \tag{3.32}$$

Table 3: LCL-filter base values and parameter limits

Quantity	Value
Z_B	$28.8427/\Omega$
L_b	$91.8091/mH$
C_b	$110.34/\mu F$
$\left(L_{f1}+L_{f2}\right)_{max}$	$9.1809/mH$
C_{fmax}	$5.5180/\mu F$

The total filter inductance is limited to maximum inductance of $9.1809mH$ and the maximum filter capacitors is limited to maximum of $5.5180\mu F$. A switching frequency of 4kHz gives a maximum permissible resonance frequency of 12 560 rad/s according to the Nyquist criterion. Figure 20 shows the relationship between the filter capacitor, total inductances and the resonance frequency. The inductance size must be chosen such that the filter capacitor adheres to the size constraint in table 3. When the filter inductance is increased, the filter capacitor size can be reduced to maintain a constant resonance frequency, which is in line with equation 3.29. Secondly, for an already significant filter inductance, the larger the inductances become, the smaller the impact on the capacitor size becomes, while maintaining a constant resonance frequency. For the range of inductances between $1.2mH$ and $3.0mH$ the filter capacitor changes from 9.8μF to 4.5μF. For the range of inductances between $5mH$ and $8mH$ the filter capacitance changes from 2.58μF to 1.59μF. This indicates that excessively increasing the filter inductance has a diminishing effect on the filter capacitor size. Therefore, inductors must be increased considering the filter capacitor size reduction that will result. Figure 20 also illustrates that increases in the filter capacitor moves the resonance frequency to lower frequencies. This increases the likelihood of the resonance frequency falling within the bandwidth frequency. Thus, providing another reason for the use of small capacitors in the LCL-filter.

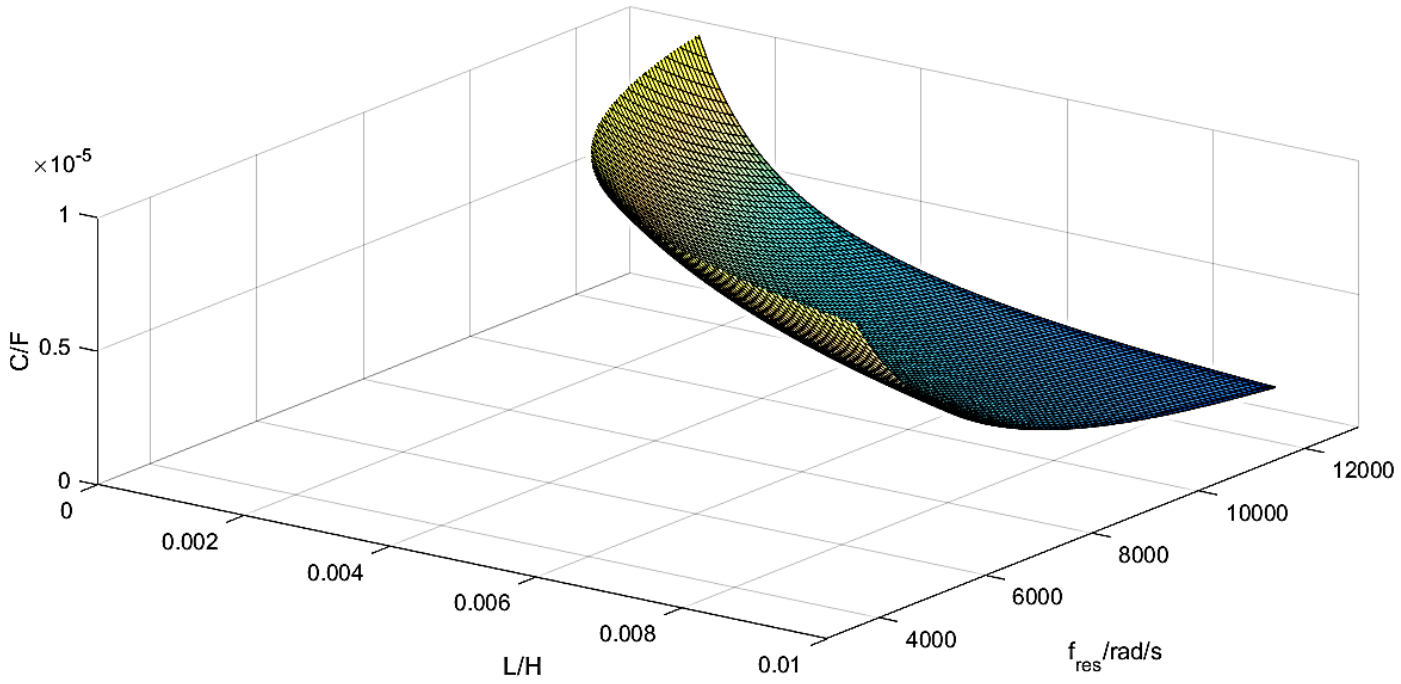

Figure 20: The relationship between the filter capacitor, inductor and resonance frequency in the design of an LCL-filter

The attenuation of load-side current harmonics can be found by taking the magnitude of equation 2.33. The attenuation at different harmonics ω_h can therefore be calculated.

$$a_h = \frac{1}{\left|2\omega_h\left(L_{f1} + L_{f2}\right) - {\omega_h}^3\left(L_{f1} + L_{f2}\right)^2 C_f\right|} \tag{3.33}$$

Figure 21 illustrates that the attenuation factor as a function of inductance at the resonance frequency. The attenuation of the resonance frequency serves as an indicator of the minimum attenuation within the whole frequency spectrum. Figure 21 illustrates that a higher resonance frequency will diminish the effects of resonance due to greater attenuation at higher frequencies. The filter capacitor can be calculated from figure 21 for each resonance peak using equation 2.34.

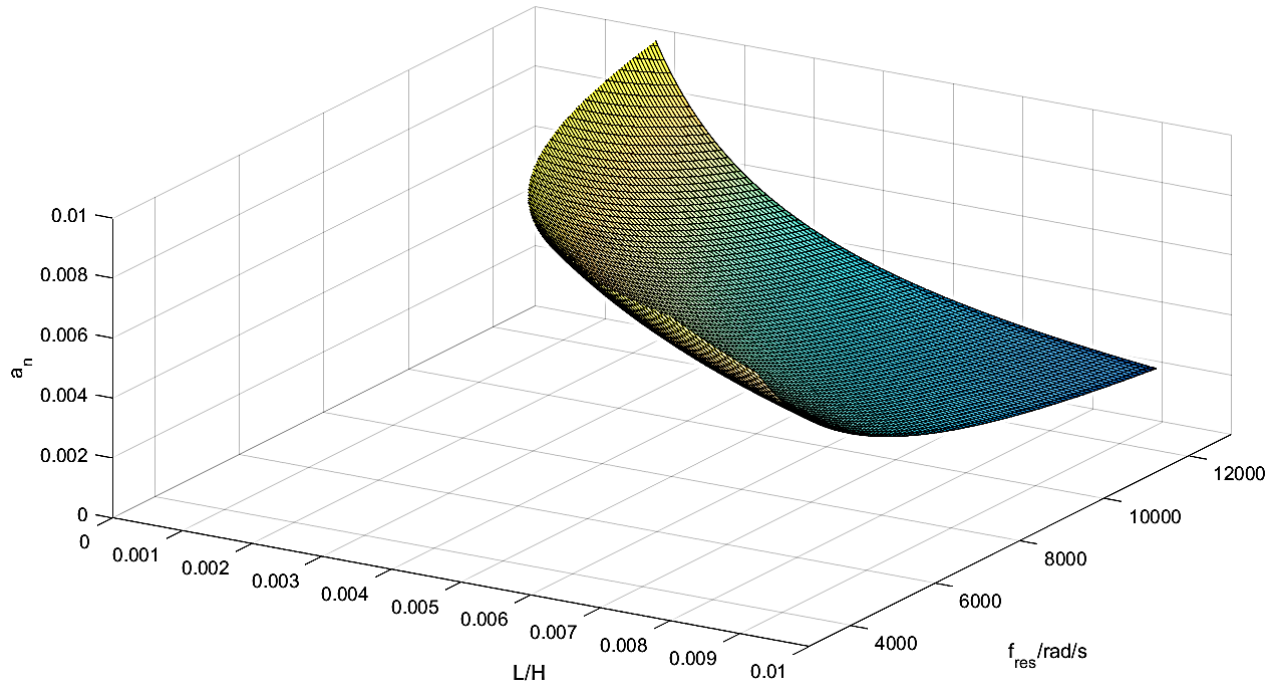

Figure 21: Attenuation of the LCL-filter a s function of inductance and frequency

Most values for the filter inductance and capacitors ensure adequate harmonic attenuation according to the IEEE-519 standard. The filter capacitors and inductances chosen for this work are given in table 3.

Table 4: Filter component values

Quantity	Value
$L_{f1} = L_{f2}$	$3mH$
C_f	$5/\mu F$

The total filter inductance is significantly lower than the inductor limit given in table 3. The filter capacitor was chosen to lower the resonance frequency of the load-side system, while still adhering to the limit given in table 3. The resonance frequency is found to be 11 547 rad/s and its location is less than half the switching frequency as required by the Nyquist criterion. The design meets the criteria mentioned earlier. The resonance frequency results in a gain of 106dB which can be reduced to 1.58dB with the use of a 100Ω damping resistor.

3.2.3 PI controller design

PI controllers are the easiest and most common method of achieving vector control. In vector control, generator and load currents are manipulated to achieve control objectives. This section demonstrates the structure of the control algorithm and determines its parameters.

The generator models in equations 2.19 and 2.20 show the presence of cross-coupling between the d-axis and q-axis stator models. The result is a nonlinear model that cannot have control techniques applied to it until it is linearized. Figure 22 illustrate that linearization is achieved by feeding the speed terms of the d-axis and q-axis model forward and subtracting them from the outputs of the controllers. The generator currents, speed and synchronous inductances are known; therefore, the speed terms can be calculated. The result is a stable first order system shown in equation 3.34.

$$\frac{1}{1+s\frac{L_{dq}}{R}} = \frac{1}{1+s\tau_{dq}} \tag{3.34}$$

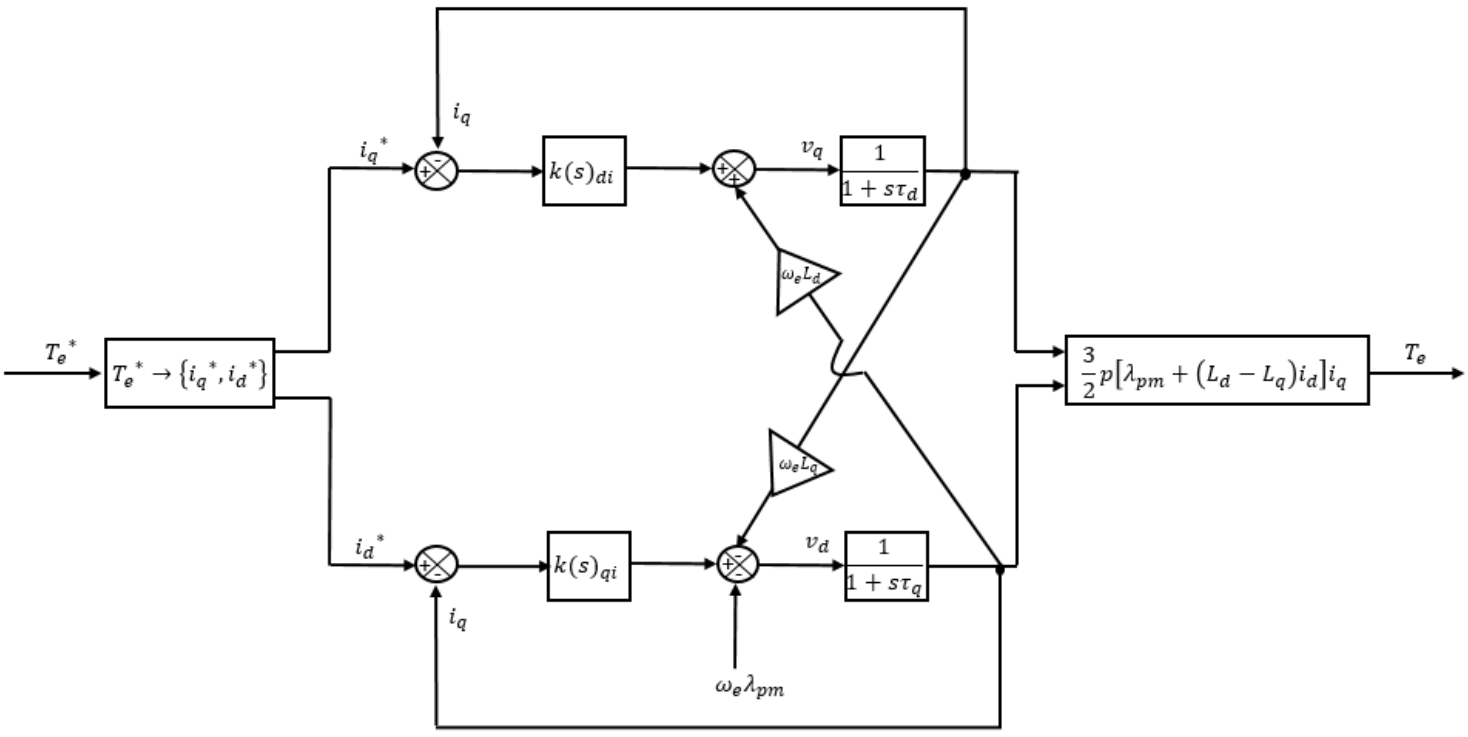

Figure 22: Control structure of generator-side control

The current references $i_d{}^*$and $i_q{}^*$ are determined from a function or look up table that map them from the electromagnetic torque reference $T_e{}^*$.

The determination of the PI controller parameters is done according to the models in equation 3.34. Because the system is stable, controller parameters will be determined by the desired system bandwidth and disturbance rejection. Generator inductances are known to vary due to changes in the rotor position, generator loading and temperature [58]. Therefore, a range of values from half the nominal values to twice the nominal values are considered in the design. The stator resistance is also varied by ±20%. Because the IPM used in this project has a large inductance, a high control bandwidth would result in large stator voltages. Therefore, a bandwidth of no greater than 1000 rad/s is chosen for a settling time of 0.01s. The d-axis and q-axis system responses are illustrated in figure 23. The responses of the currents track the output reference within 0.0085s for all generator parameter variations, which is close to the desired bandwidth. The bode diagram in figure 23 (d) and 23 (h) show that that the system is globally stable, even as the system parameters vary. Figure 23 (f) shows the system's response to an input disturbance of 100% of the set point. The disturbance peaks at 1% of the setpoint and is quickly attenuated to zero. Figure 23 (g) shows the system's response to an output disturbance of 100% of the setpoint. The initial effect of the disturbance on the output is large because it happens at the output of the system, but is attenuated to zero within 0.01s. The system is deemed to be both fast and robust.

$$K_d = 80 + \frac{3440}{s} \qquad K_q = 68 + \frac{4740}{s} \tag{3.35}$$

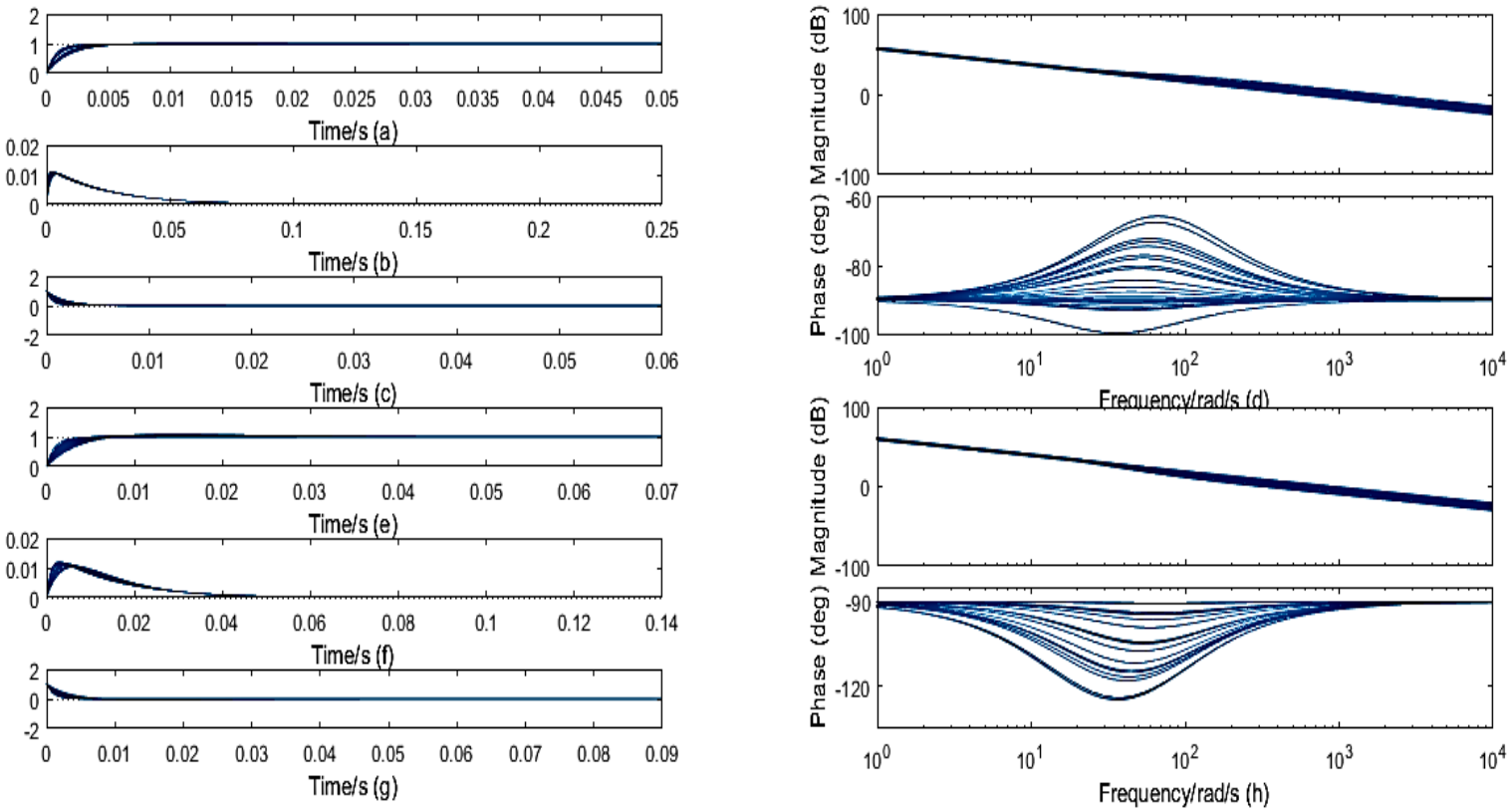

Figure 23: d-axis generator system response (a) step response of generator-side system (b) Input disturbance response (c) Output disturbance response (d) Bode plot. q-axis generator system response (e) step response of generator-side system (f) Input disturbance (g) Output disturbance response (h) Bode plot

Typically, the load-side system is responsible for the regulation of the DC-link. A fast current response is required to achieve this. The control structure in figure 24 is derived from the models in equations 2.37, 2.38 and 2.42. The load-side system also has speed coupling terms in each of the current model; therefore, the decoupling method used on the generator-side control system is also applicable on the load-side system. As discussed in section 2.4, the LCL-filter model is approximated by a first order system as shown in equation 3.36 for the design of the PI controllers. However, when simulated in MATLAB in figure 25, the LCL-filter's third order model is used to validate the effectiveness of the control system.

$$\frac{1}{1+s\frac{L_{dq}}{R}} = \frac{1}{1+s\tau_e} \tag{3.36}$$

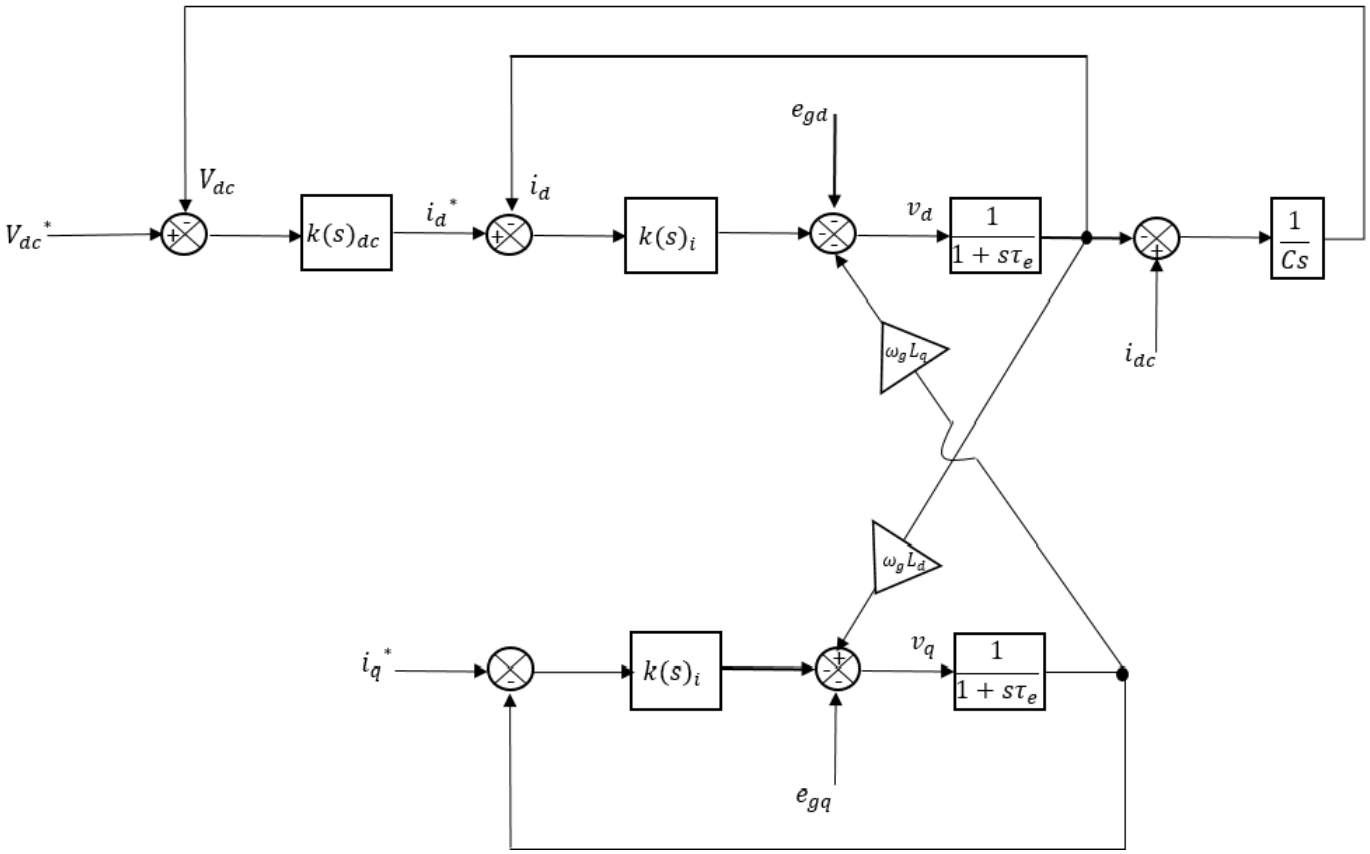

Figure 24: Control structure of the load-side system

The control structure comprises of an inner-loop that controls the current and an outer-loop that regulates the DC-link voltage. The inner and outer-loop control parameters can be designed separately if the inner-loop control response is significantly faster that the outer-loop control. Most literature recommend that the inner-loop control system be at least 10 times faster to limit the inner-loop's effect on the outer-loop control system [59]. The d-axis and q-axis inductances on the load-side are the same, thus, only one controller for the inner-loop needs to be designed. The load-side inductances and resistance are made to vary in the same manner as the generator parameters. The current and DC-link controllers in equation 3.37 give the system response in figure 25. The inner-loop current control in figure 25 (a) is 20 times faster than the outer-loop DC-link voltage control in figure 25 (e), which allows for a smooth DC-link voltage response. The currents response was made 20 times faster than the DC-link voltage response to accommodate any unforeseen delays that could happen during the experiments. Figure 26 (d) shows that the gain margin of the inner current loop is 15dB due to the system being a third order system. Thus, large stator voltage demands can cause instability to the system. If this is the case during the experiments, due to unmodeled behaviour such as sampling and switching, then the gains of the controllers will be lowered.

The current input disturbance response does not exceed 5% and the output disturbance is attenuated within 0.005 seconds as shown in figure 25 (b) and (c) respectively. While the output disturbance response of the DC-link shows satisfactory performance, the input disturbance takes 8s to reject a step disturbance. Therefore, the current input into the DC-link must not be varied too rapidly to avert significant input disturbances that may occur.

$$K_i = 18 + \frac{2916}{s} \qquad K_{DC} = 0.3 + \frac{0.1}{s} \tag{3.37}$$

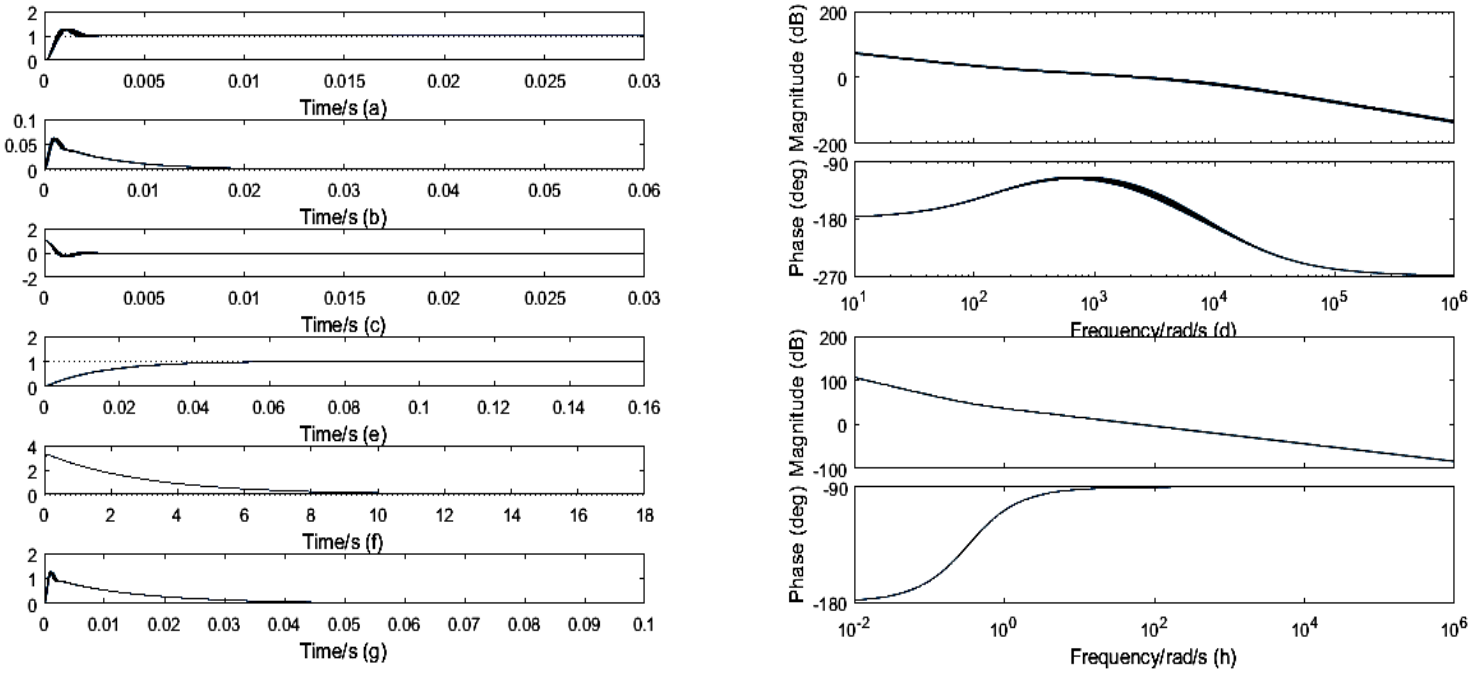

Figure 25: load-side system response (a) step response of load-side system (b) Input disturbance response (c) Output disturbance response (d) Bode plot. DC-link response (e) step response of generator-side system (f) Input disturbance (g) Output disturbance response (h) Bode plot

3.3 Analysis on the control of an IPM

The IPM provides a host of control possibilities due to it being a salient pole machine. This section provides an analysis of different control strategies that are possible for an IPM.

Equation 2.27 gives the expression for the electromagnet torque developed by an IPM. The torque expression is highly nonlinear and is dependent on both the d-axis and q-axis currents. As a result, the same current magnitude can result in different developed electromagnetic torque depending on its phase. Figure 26 shows the relationship between the developed torque and the synchronous stator currents. A contour map shows regions of the same torque

magnitude. It is shown that the optimum torque is developed when the torque angle is between 90° and 270°(second and third quadrant) depending on the direction of the torque.

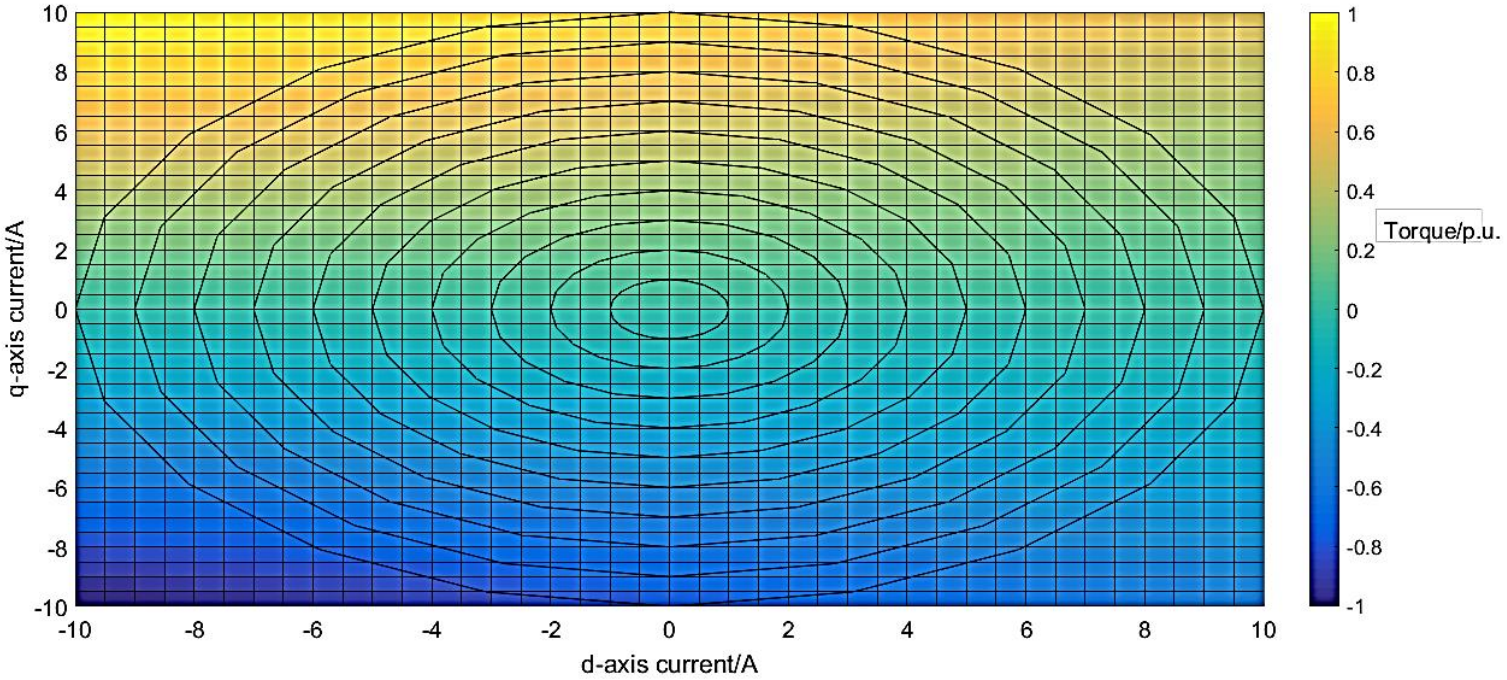

Figure 26:Developed torque as result of stator currents

In the second and third quadrants, the d-axis current is negative, as a result, a magnetic flux-linkage opposite to that created by the rotor magnets is developed in the stator. This is called flux weakening. A positive d-axis current results in an increase in the magnet-flux-linkage and can lead to the saturation of the machine, increasing core losses in the process. It also makes for a poor voltage utilisation as will be seen later in this discussion.

The torque expression in equation 2.27 is written in terms of the stator current magnitude and the torque angle in equation 3.40.

$$i_d = I_s cos\theta_t \tag{3.38}$$

$$i_q = I_s sin\theta_t \tag{3.39}$$

$$T_e = \frac{3}{2} p \left[\lambda_{pm} I_s sin\theta_t + \frac{\left(L_d - L_q\right) I_s^2 sin2\theta_t}{2} \right] \tag{3.40}$$

By taking the derivative of the ratio between torque and current magnitude relative to the torque angle and equating it to zero the torque angle that maximises the toque-current magnitude ratio is found.

$$\frac{d}{d\theta_t}\left(\frac{T_e}{I_s}\right) = \frac{3}{2}p\left[\lambda_{pm}I_s cos\theta_t + \left(L_d - L_q\right)I_s^2 cos2\theta_t\right] = 0 \tag{3.41}$$

$$\theta_{to} = cos^{-1}\left[\frac{\lambda_{pm}}{4\left(L_d - L_q\right)I_s} \pm \sqrt{\left(\frac{\lambda_{pm}}{4\left(L_d - L_q\right)I_s}\right)^2 + \frac{1}{2}}\right. \tag{3.42}$$

Equation 3.42 gives two solutions, which is consistent with figure 26. One solution will result in the increase of the magnet flux-linkage which is not desirable and the other will result in its decrease. The result is a torque angle θ_{to}, that results in maximum torque per ampere (MTPA).

The equivalent circuits in figure 7 are simulated in MATLAB, the torque angle is varied from $0°$ to $180°$ and the stator current magnitude is also varied according to figure 27. At lighter loads, the developed torque does not vary much with the torque angle. However, a maximum torque value exists for all current magnitudes as shown in figure 27 (a). The difference becomes more apparent as the load is increased.

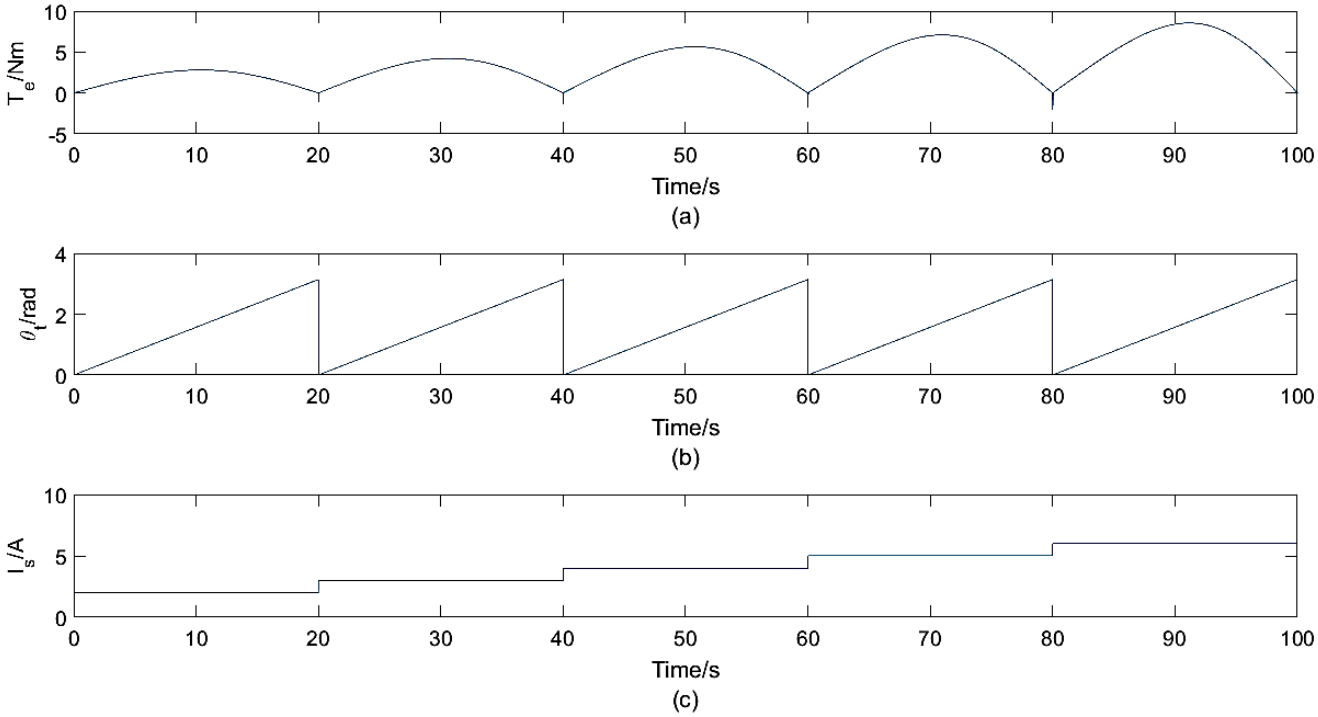

Figure 27:(a) Developed electromagnetic torque (b) torque angle (c) stator current magnitude

The MTPA torque angle θ_{to} is calculated using equation 3.42. For low loading, the optimal torque angle is near $90°$ gradually changing to $100°$ as the load current increases, as shown in figure 28.

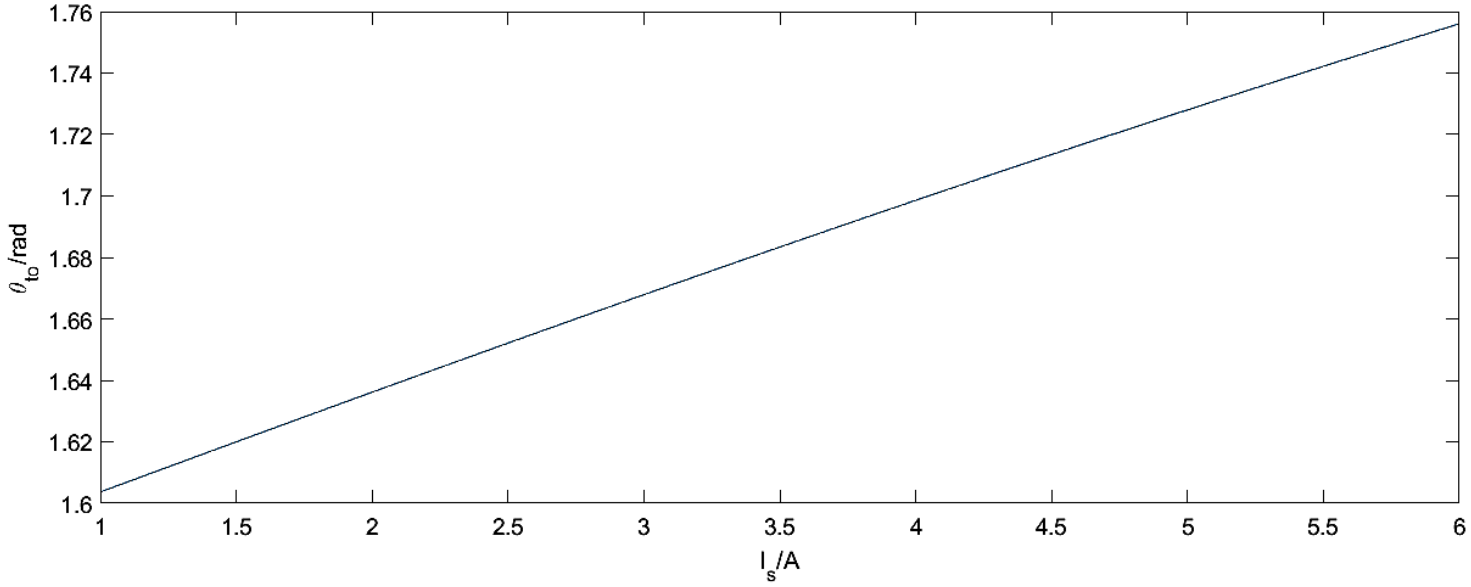

Figure 28: Optimal torque angle values

Figure 29 shows the stator terminal voltage magnitude required to drive current through the stator at a different torque angles, this is referred to as DC-link voltage utilisation. The name is derived from the fact that the converter sources its voltage from the DC-link. The maximum output phase voltage of the converter is $\frac{V_{dc}}{\sqrt{3}}$. Exceeding this voltage results in converter saturation, which leads to an increase in the THD from the converter and possible loss of control capability.

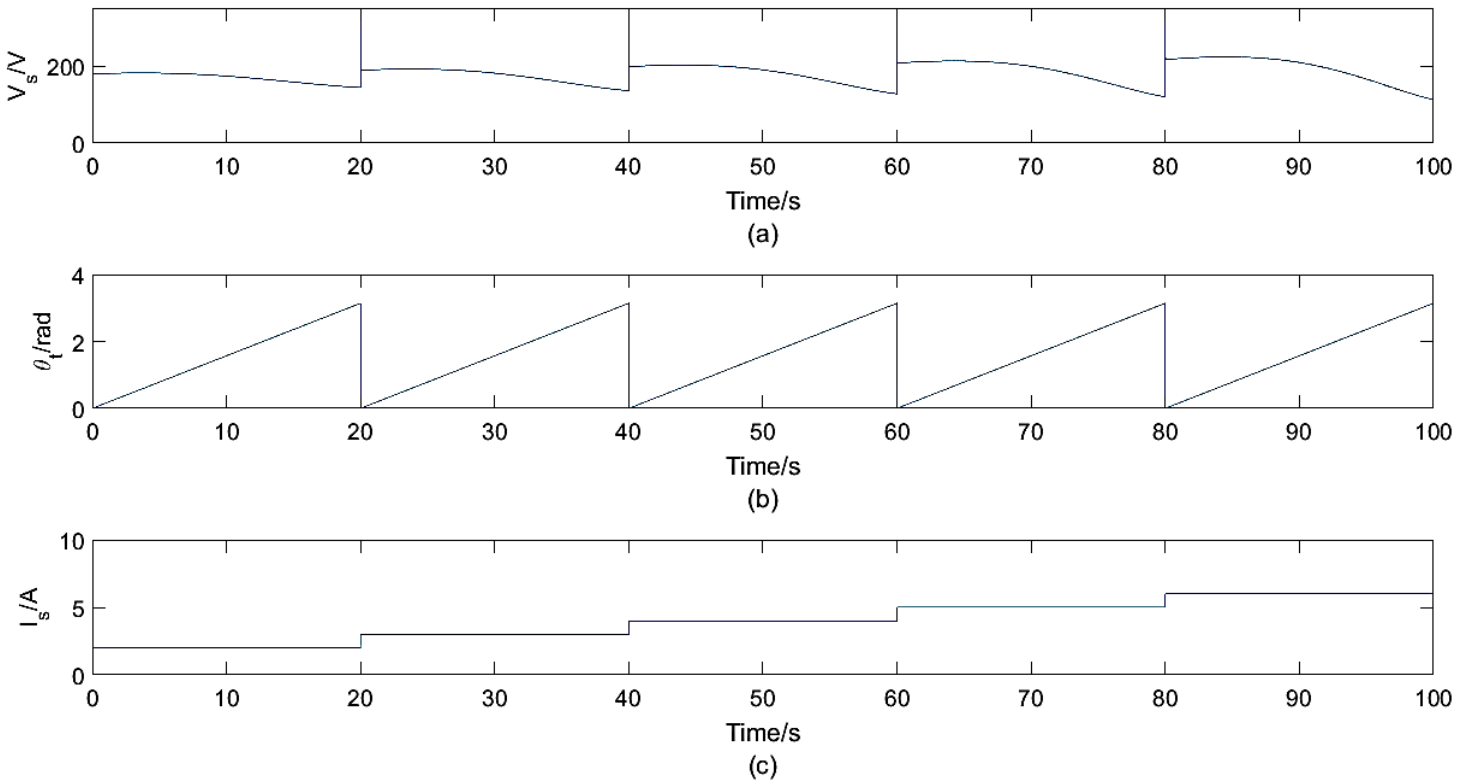

Figure 29:(a) Stator terminal voltage (b) Torque angle (c) Stator current magnitude

The DC-link utilisation is highest at a torque angle of $0°$ and decreases as the torque angle increases towards $180°$. A torque angle between $0°$ and $90°$ means that the d-axis current is greater than zero, which adds to the magnetic flux-linkage and in turn induces a high EMF in the IPM. The converter voltage required to drive current against the induced EMF will be high, which explains the high DC-link utilisation. A torque angle between $90°$ and $180°$ results in field weakening and a smaller DC-link utilisation will be observed. A torque angle of θ_{to} has a high DC-link utilisation, despite the improved conduction loses associated with MTPA control. Therefore, switching losses are not at a minimum with MTPA control.

The effect of the torque angle on the power factor of the generator is illustrated in figure 30. Torque angles lower than the $90°$ result in the lowest power factor. A torque angle of θ_{to} results in a power factor close to unity. The power factor profile in figure 30 (c) shows that the power factor varies little near unity power factor. There exists a sizable range of torque angles that result in a near unity factor around the maximum power factor.

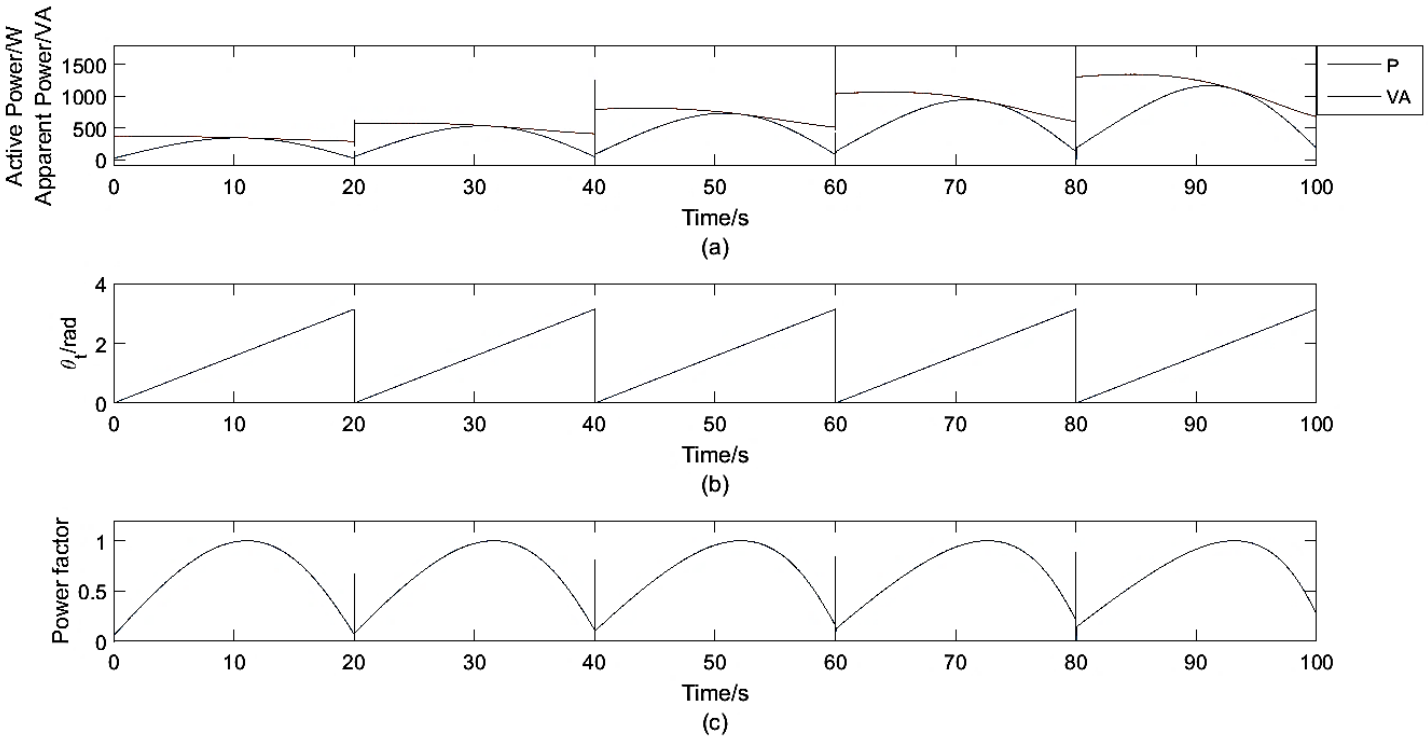

Figure 30: (a) Active and reactive power production (b) torque angle variation (c) Subsequent power factor variation

Unity power factor (UPF) control refers to production of power by the generator at unity power factor. The torque angle that results in the production of power at unity power factor θ_{tu}, is larger than the MTPA torque angle. Equations 2.19 and 2.20 are expressed in terms of the torque angle below.

$$V_d = R_s I_s \cos\theta_t - \omega_e L_q I_s sin\theta_t \tag{3.43}$$

$$V_q = R_s I_s sin\theta_t + \omega_e L_d I_s cos\theta_t + \omega_e \lambda_{pm} \tag{3.44}$$

To achieve unity power factor, the stator voltages and currents must be in phase.

$$\frac{V_q}{V_d} = \frac{sin\theta_t}{cos\theta_t} \tag{3.45}$$

Equation 3.43 is substituted into equation 3.44 to form a quadratic expression for the cosine of the torque angle. The equation is subsequently solved and a formula for θ_{tu} is derived in equation 3.48.

$$\lambda_{pm} cos\theta_t + I_s\left(L_d cos^2\theta_t + L_q sin^2\theta_t\right) = 0 \tag{3.46}$$

$$I_s\left(L_d - L_q\right)cos^2\theta_t + \lambda_{pm} cos\theta_t + I_s L_q = 0 \tag{3.47}$$

$$cos\theta_{tu} = \frac{-\lambda_{pm} \pm \sqrt{{\lambda_{pm}}^2 - 4L_q{I_s}^2(L_d - L_q)}}{2{I_s}^2 L_q(L_d - L_q)} \tag{3.48}$$

Only the positive sign in equation 3.48 is considered as it gives real solutions in the second quadrant. Figure 31 shows the torque angle required for the realisation of UPF control for different stator current magnitudes.

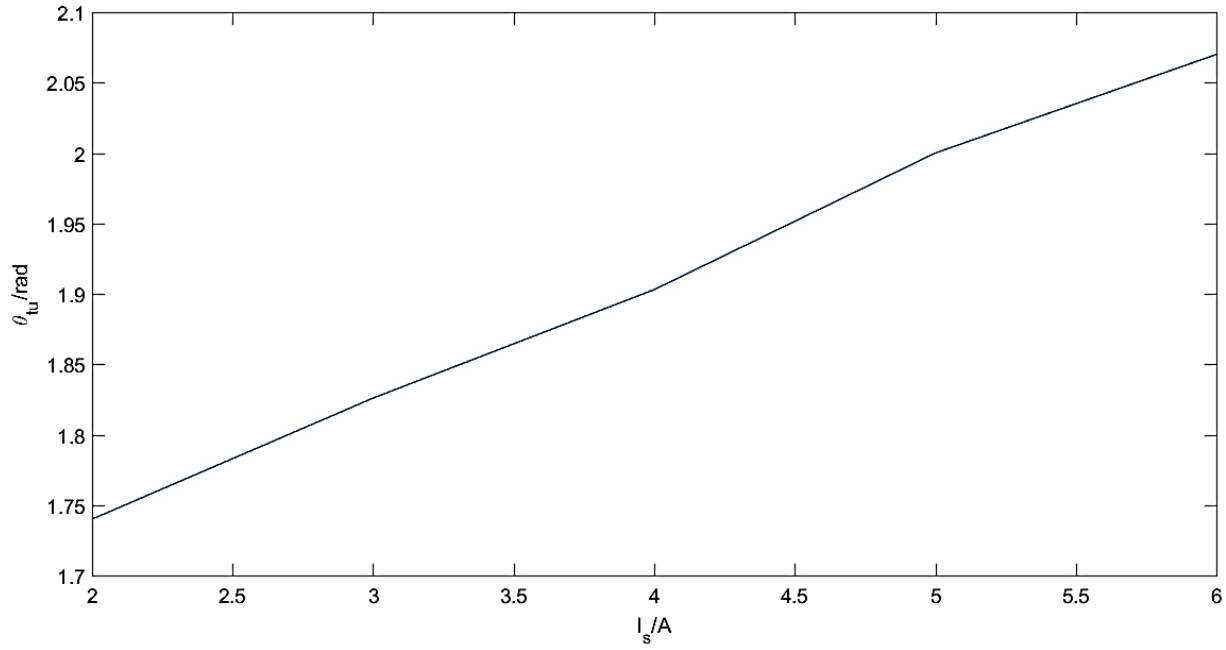

Figure 31:Torque angles required for the realisation of UPF control

UPF control does not result in the optimal production of Torque, but results in a smaller DC-link utilisation, due to a larger negative d-axis current component. As a result, the constant torque region of the IPM is extended.

The previous discussion may deceptively suggest that optimal torque control will result in the most efficient operation of the IPM due to a minimisation of conduction losses. However, this argument does not include other losses, such as core and windage losses, which are difficult to model. A truly optimal control scheme can only be investigated experimentally, and would minimise all losses associated with the generator and mechanical losses resulting from being coupled with the turbine emulator. One such control scheme is developed in chapter 6.

Chapter 4

4. Simulations

This section discusses simulations carried out prior to the lab experiments. MATLAB/Simulink is used to simulate each component of the system individually, to assess each's performance. The models are based on the d-q models discussed in section 2.4. The Simulink models offered in the library allow for the effects of sampling and converter switching to be included in the analysis. Therefore, more accurate result can be obtained as compared to those found in chapter 3. The system is comprised of the gas turbine emulator, the generator-side system and the load-side system. Due to a malfunctioning encoder, the PMSG could not be driven faster than 1100RPM. This limitation is considered in the simulations carried out, for an analysis that will bear similar results to the practical experiment.

4.1 Gas Turbine model

The turbine gas generator comprises of two parts: the gas turbine and the IPM. The two systems have separate control systems according to the discussion in section 2.2, which makes this application unconventional. The focus of this work is concerned with the effect of the gas turbine on the IPM. Therefore, the gas turbine emulation requirements will include the turbine's torque, speed and acceleration as well as the behavior of its control system. The turbine will be assumed to be operating under ideal conditions in terms of temperature and gas generator turbine (refer to figure 1) operation. Thus, the control of gas-turbine system is solely dedicated to the control of the free-turbine speed and acceleration.

There is no attempt to modify the structure of the turbine model or its controls in this report. Therefore, the dynamic behavior of the turbine can only be influenced through the control of IPM. Figure 32 shows the response from the gas turbine under a loading of 3Nm and 6Nm at 20 seconds and 40 seconds respectively. After a sharp deceleration, the turbine's speed governor regulates the turbine's speed back to its reference value of 94rad/s. This is done by changing the free-turbine torque T_{ft} according to the load torque from the generator.

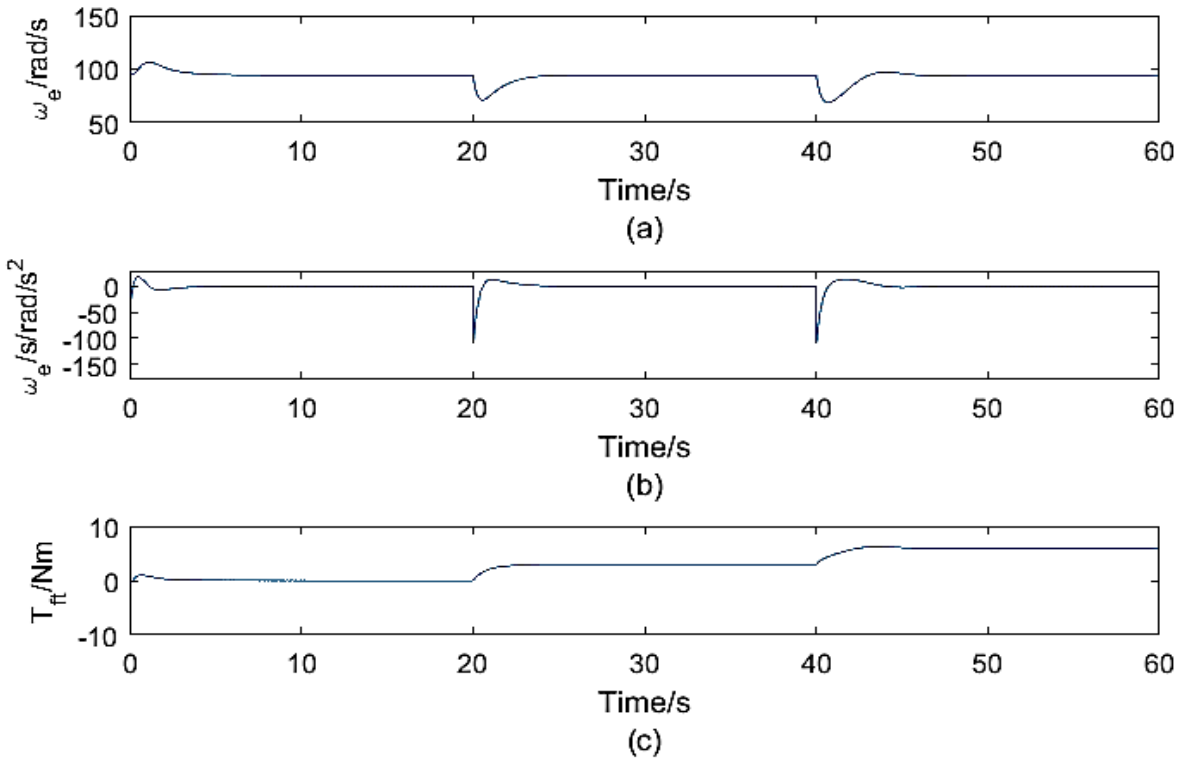

Figure 32: Free-turbine (a) speed regulation (b) acceleration regulation (c) Torque response

Loading the turbine suddenly causes large deceleration of the free-turbine. The turbine control system reacts by increasing torque production dramatically, causing an overshot in the speed. On the generator-side this would result in a sudden increase in power production. In isolated mode of operation, the excess power may have no way to go except to the DC-link, where large voltages could damage the DC-link capacitor. This issue is alleviated by gradually increasing the load torque from the IPM, which would result in a gentler deceleration. In figure 33 the load torque from the IPM is gradually increased which results in better response. However, the speed deviation lasts longer than in the previous case, but is not as large. Therefore, instead of an overproduction of power, there may exist a shortage of power for a short time period, which in most cases would not cause damage.

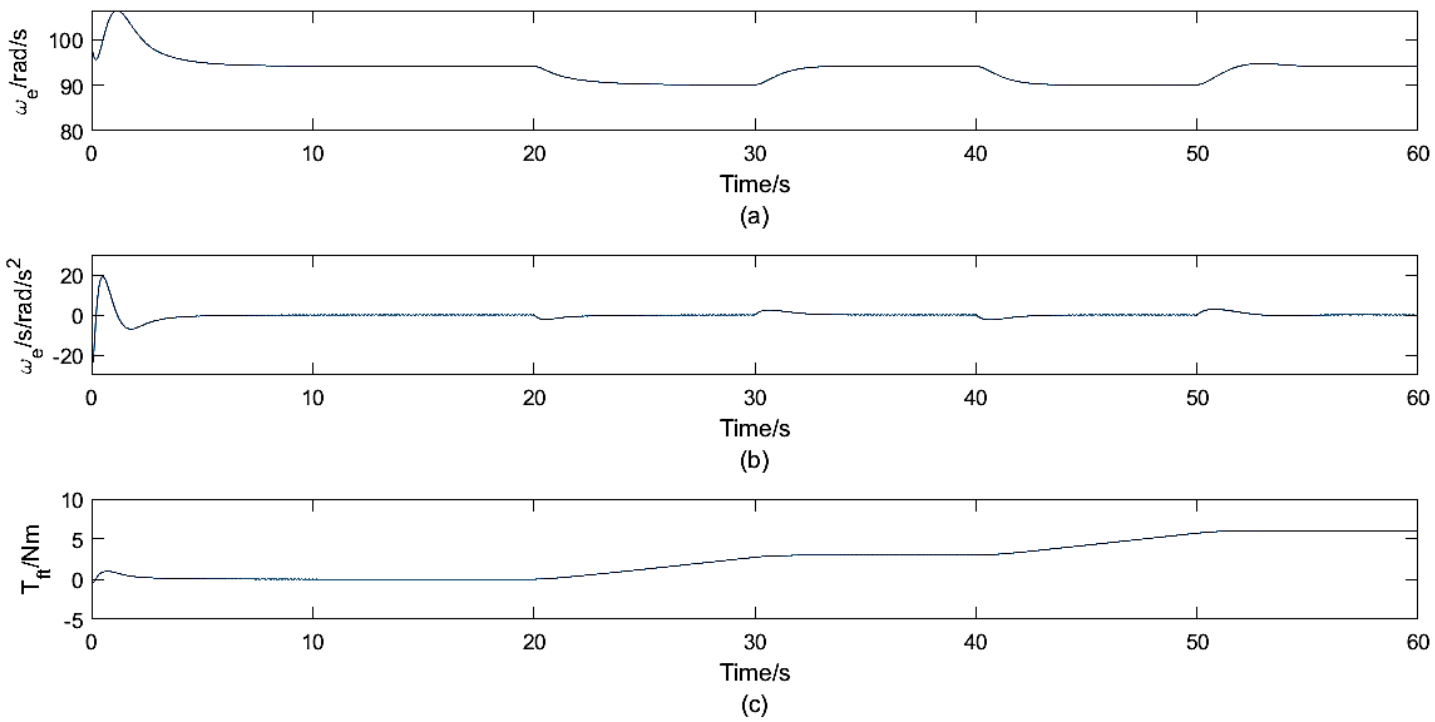

Figure 33: Free-turbine (a) speed regulation (b) acceleration regulation (c) Torque response

4.2 Generator control

In section 3.3, a detailed analysis of the various control strategies for an IPM is made. The results of this section can be compared with those found in section 3.3 and experimentally in chapter 6.

4.2.1 Generator current control

Stator currents determine the electromagnetic torque and torque angle of the IPM, which in turn is used to form the bases of all AC generator control strategies. Thus, current control forms the inner-loop control of all control strategies. The outer-loop control is used to achieve the control objective, and has the current control loop nested within itself. A fast and robust current control scheme is required for implementation into a cascaded control structure. The simulation setup is illustrated by figure 34. A DC source is used in the place of the DC-link, therefore as much current can be sourced from it as required. The DC voltage is set to 400V to match the DC-link voltage used during experimentation. Generator speed is regulated by the gas turbine. From figure 33, it is noted that any variations in speed are slow. Therefore, for simulation purposes the speed is considered constant at 120rad/s.

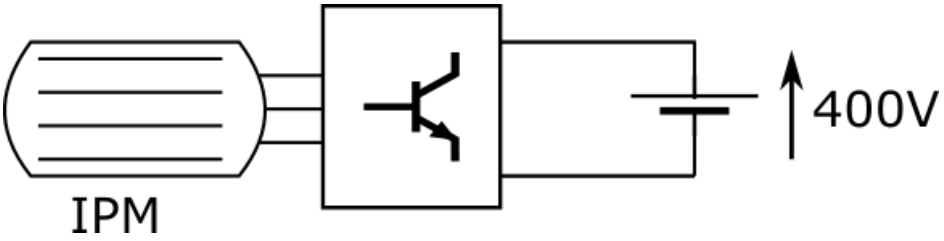

Figure 34: Generator simulation setup

Figure 35 shows the d-axis and q-axis current response to two changes in the current reference points at 0 seconds and 0.1 seconds respectively. The current responses take no more than 0.05 seconds to reach their respective references. The d-axis settling time is within the same order of magnitude as that in figure 23 in section 3.2.3. The slight delay in the settling time in figure 35 can be attributed to delays associated with sampling and switching. The q-axis inductance is significantly larger than the d-axis inductance. Therefore, it is expected that the q-axis current response will be slower than d-axis current response. The overshoot can also be attributed to the slow response of the q-axis current due to the higher inductance. The simulations section 3.2.3 are done in the synchronous reference frame with pure DC quantities. The control in this ideal scenario result in fast current responses. Simulink includes the conversion of AC quantities to DC quantities through the park's transform and includes harmonics generated from the converter. Therefore, the implementation of control voltages by the converter will not be as effective as in section 3.2.3, and differences in the synchronous inductances will have more of an effect on stator current responses.

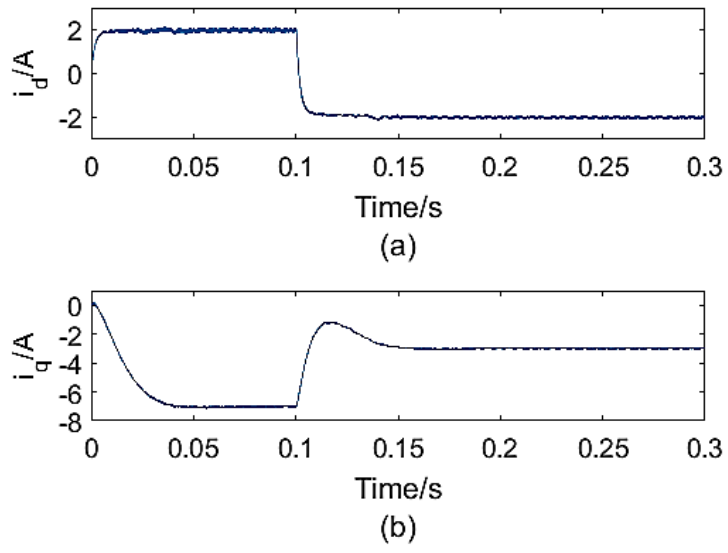

Figure 35: (a) d-axis current step response (b) q-axis current step response

4.2.2 Comparison of control strategies

The control strategies in section 3.3 are performed in Simulink and revaluated with previously unmodeled behaviour included in the analysis.

In figure 36 the stator current magnitude is kept constant for 0.5 seconds and then increased. The torque angle is varied to observe the change in developed torque. As in section 3.3, lower loading shows little variation in the developed torque as a function of the torque angel. The presence of a peak torque for each current magnitude can readily be seen. The torque angles for MTPA control are found to be $\theta_{to} = [1.78 : 2.08]\, rad$. This differs with the optimal torque angle in figure 28 of section 3.3 where θ_{to} varies from 1.6rad to 1.76rad. The torque angles for MTPA control θ_{to} are given in figure 37.

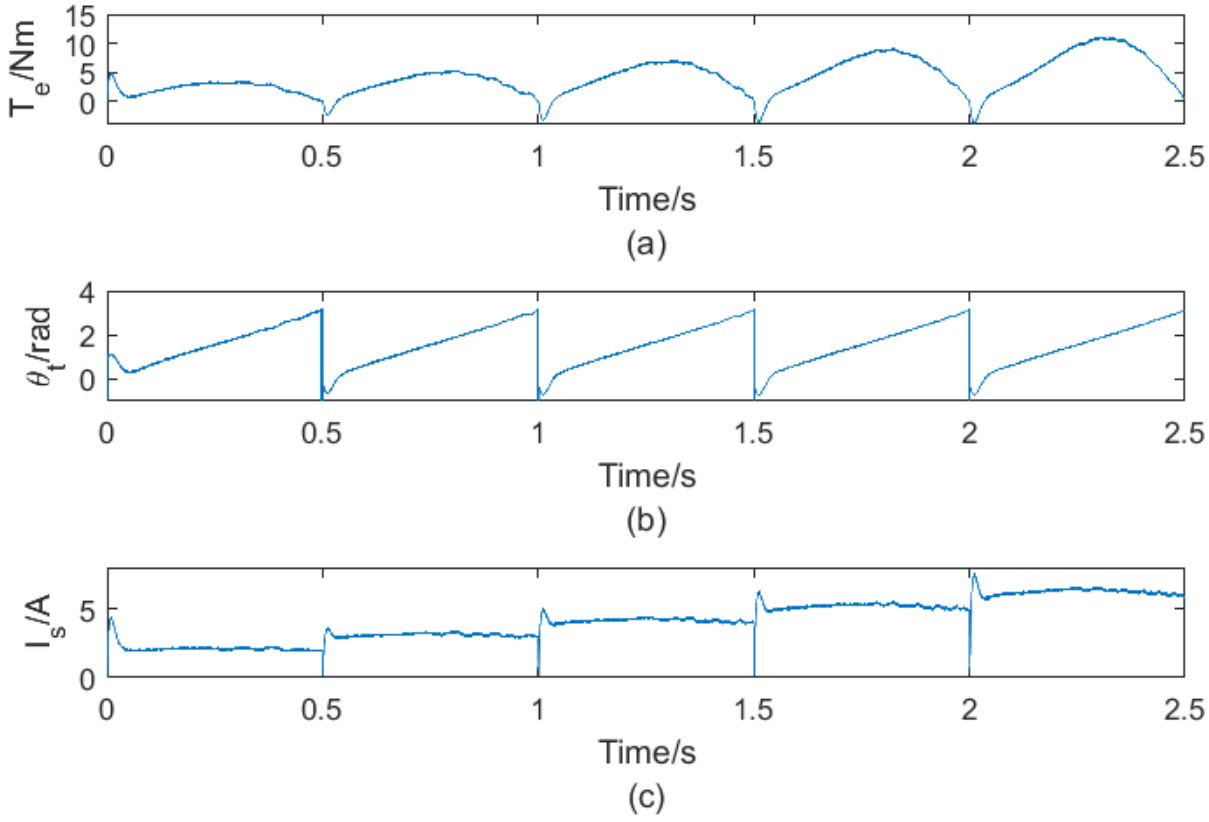

Figure 36:(a) Developed electromagnetic torque (b) torque angle (c) stator current magnitude

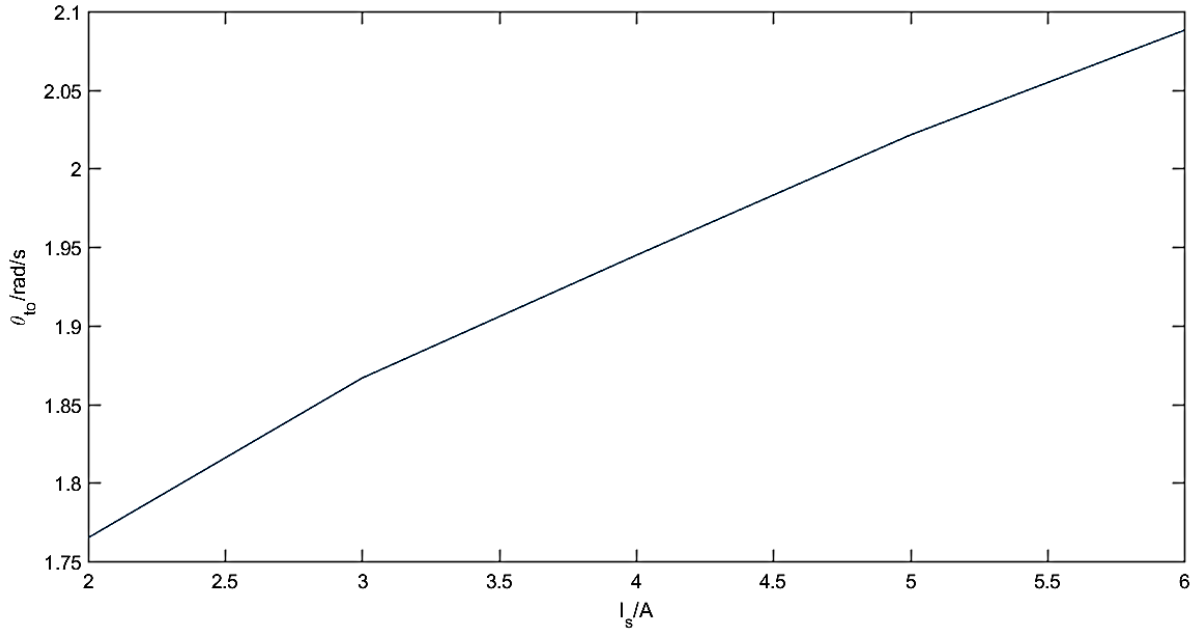

Figure 37: Optimum torque angles for MTPA control

While the optimal torque angle increases as the stator current increases in the same manner as in figure 28 in section 3.3, the MTPA torque angles found in this section show a greater variation. Analysing d-q models on their own is not sufficient to provide clarity on generator behaviour.

The DC-link utilisation is associated with the modulation index of the converter, the larger the required converter voltage the larger the DC-link utilisation and thus the modulation index. The space vector modulation (SVPWM) technique incorporates an equivalent to a third harmonic injection into the modulation signals. This allows for a higher DC-link utilisation than sine wave modulation (SPWM). However, during overmodulation, the SVPWM injects significant harmonics into the system and can cause system instability. In [60], a review of overmodulation techniques is given. Figure 38 shows typical SVPWM duty cycles under different modulation indexes. Once the duty cycle exceeds unity, overmodulation occurs. In this work operation during overmodulation is not considered. Therefore, it is required that control objectives be achieved without the converters going into over modulation. Therefore, control techniques that require lower DC-link utilisation gain additional importance in this circumstance because an overmodulation strategy is not considered.

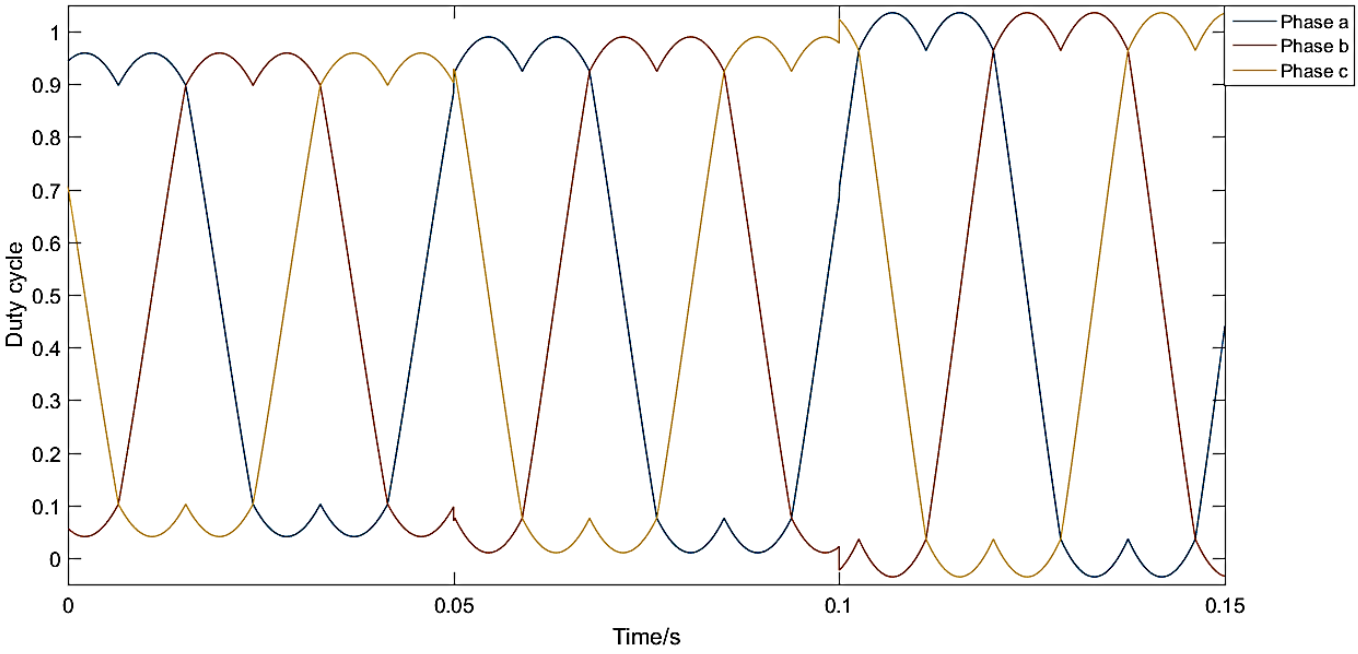

Figure 38: Duty cycles under different modulation indexes

A negative d-axis current reduces the induced EMF in the generator as previously stated. Thus, the lower the induced voltage, the lower the voltage required from the converter to implement current control. This is illustrated in figure 39; as expected, torque angles larger than $90°$ result in a significant reduction in the stator terminal voltages required to drive each current magnitude. Torque angles below $90°$ result in a positive d-axis current and show the largest required stator terminal voltage. Secondly, larger current magnitudes show a greater variation in the stator terminal voltage as a function of the torque angle. The findings are consistent with the results in section 3.3 in figure 29.

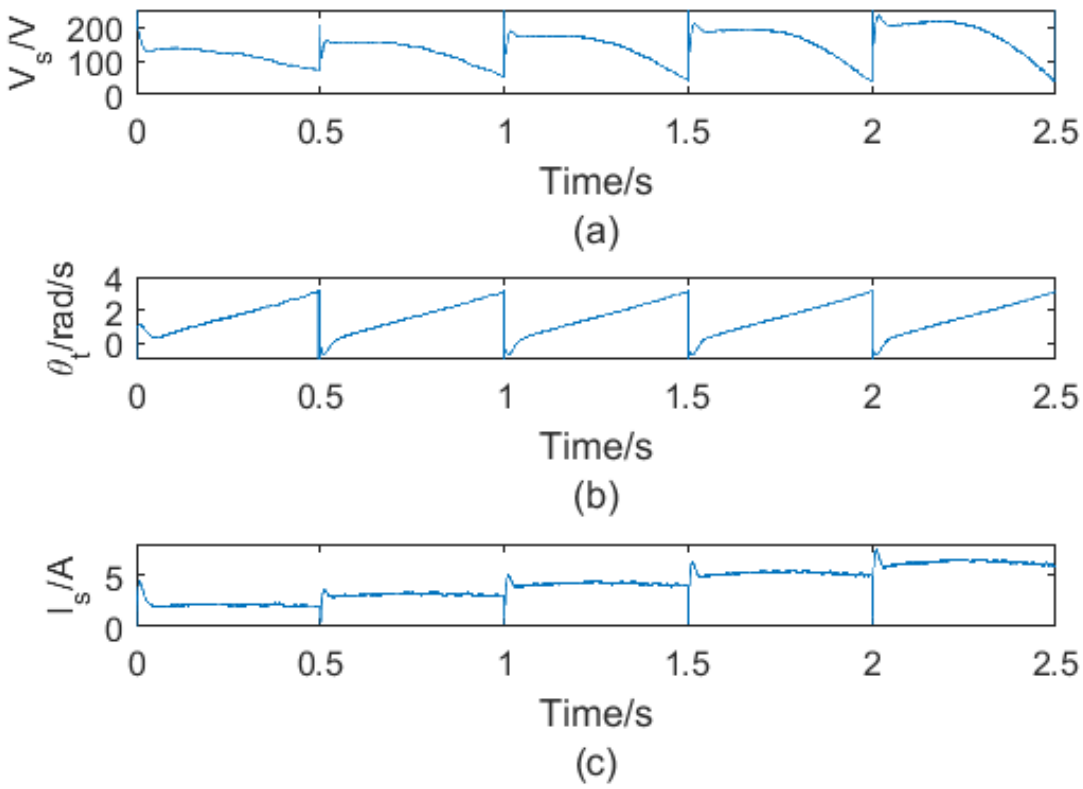

Figure 39: (a)Stator terminal voltage (b) Torque angle (c) Stator current magnitude

The effect of the torque angle on power production and power factor is illustrated in figure 40. Torque angles lower than $90°$ shows power production at a low power factor. Secondly, the power factor displays little variation near unity power factor. For example, for a stator current of 5A, for the range of torque angles $\theta_t = [2.403: 2.900]rad$, the power factor varies from 0.976 to unity. The torque angles required for UPF control θ_{tu} are given in figure 41. The trend of the torque angle against the stator current takes a similar shape to that discussed in section 3.3 in figure 31.

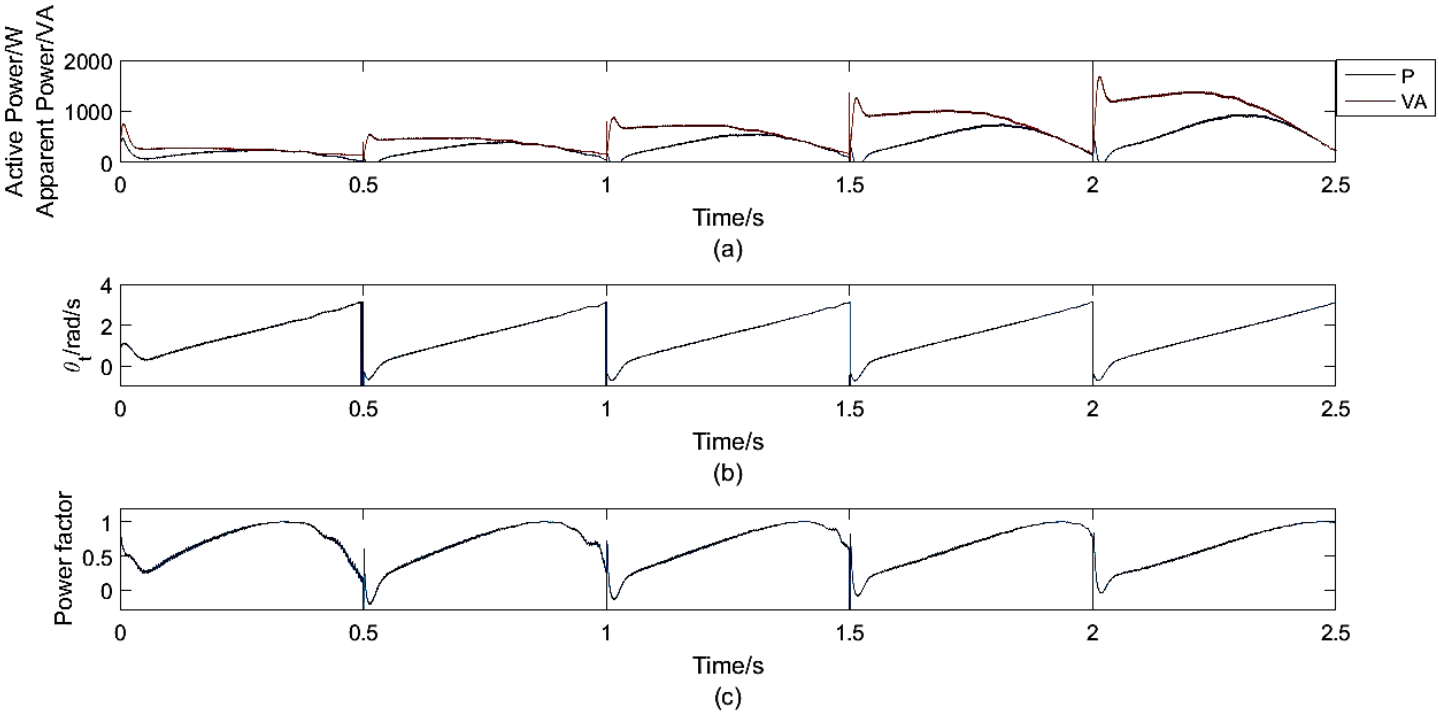

. Figure 40: (a) Active and reactive power production (b) torque angle variation (c) Subsequent power factor variation

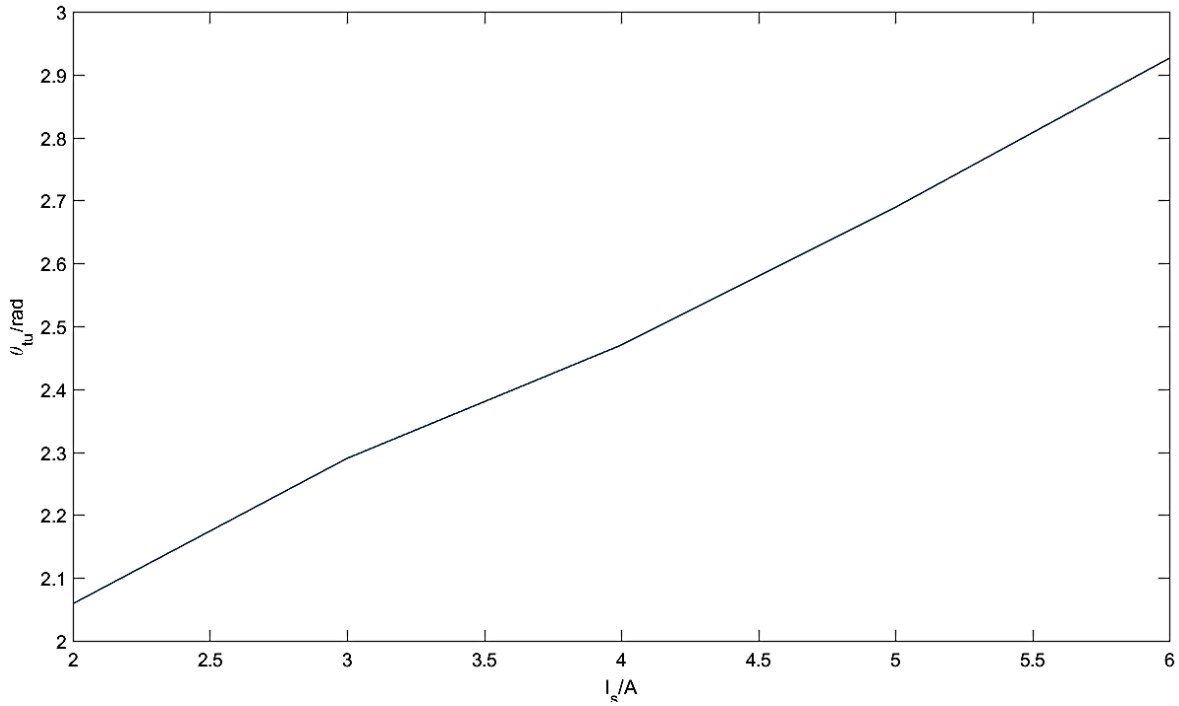

Figure 41: Torque angles required for the realisation of UPF control

A comparison of the performance of the control strategies is given in figure 42. The control strategies are compared in terms of their developed torque, DC-link utilisation and power factor. The generator stator current magnitude is regulated to 6A. NTA control is the most

popular control strategy due to its simplicity, and is implemented first. In NTA control the reluctance torque is set to zero by regulating the d-axis current to zero. The q-axis current is solely responsible for producing of electromagnetic torque. Next, MTPA control is implemented, this done by setting the torque angle according to figure 37. Lastly, UPF control is implemented by setting the torque angle according to figure 41. MTPA shows the highest torque production of three control strategies. It also displays, a lower stator terminal voltage requirement and a higher power factor than NTA. UPF control shows the lowest stator terminal voltage requirement, the highest power factor and a torque production higher than NTA. NTA ranks last in all three categories.

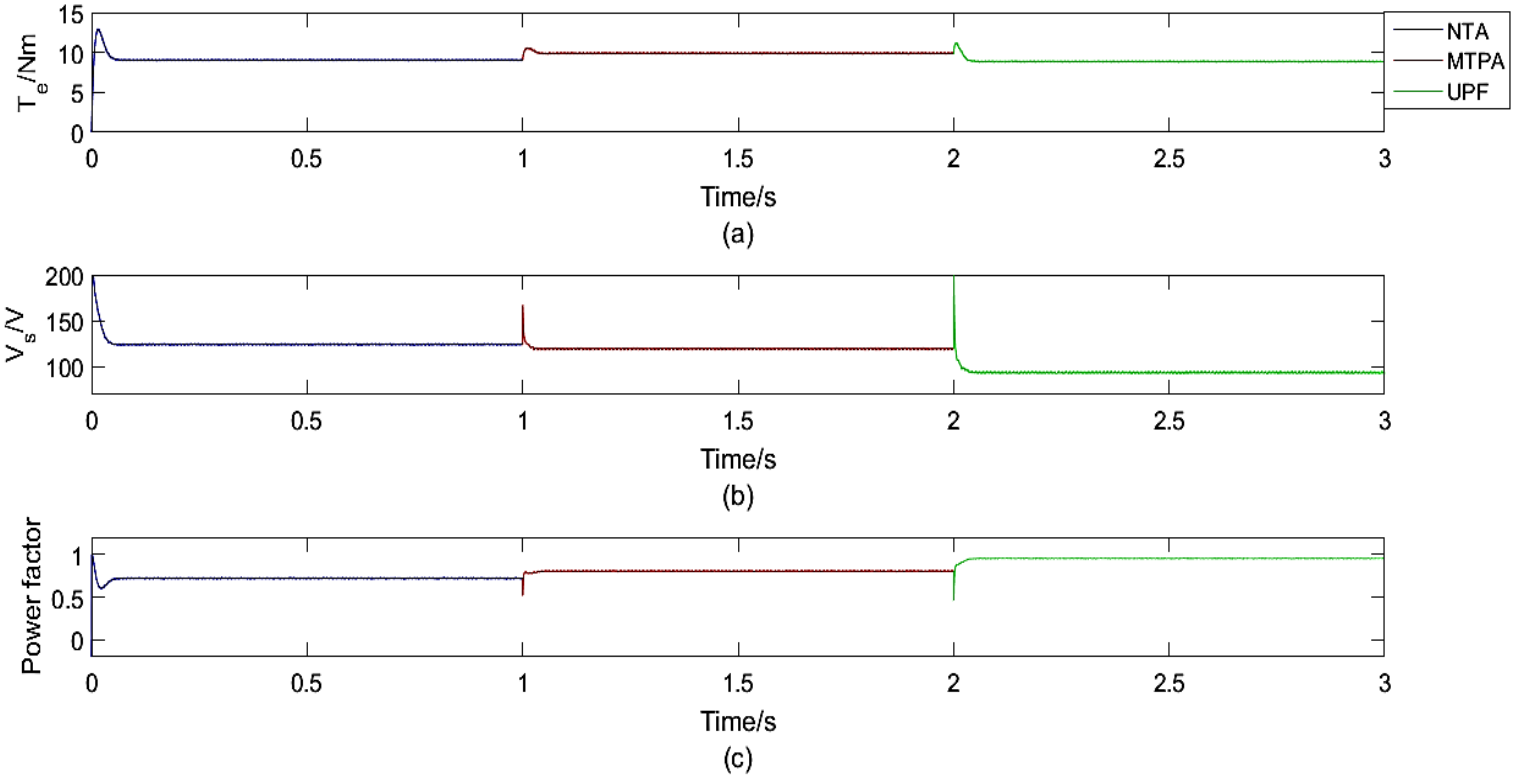

Figure 42: (a) Torque production (b) Stator terminal voltage (c) Power factor

A similar simulation is conducted where the developed torque is kept constant at 10Nm. The current magnitude required to sustain the developed torque is compared across the control strategies. MTPA as expected shows the smallest current required to sustain the developed torque, followed by UPF. Again, NTA ranks last in this category, requiring the most stator current to achieve the same developed torque as MTPA and UPF. The result is shown in figure 43.

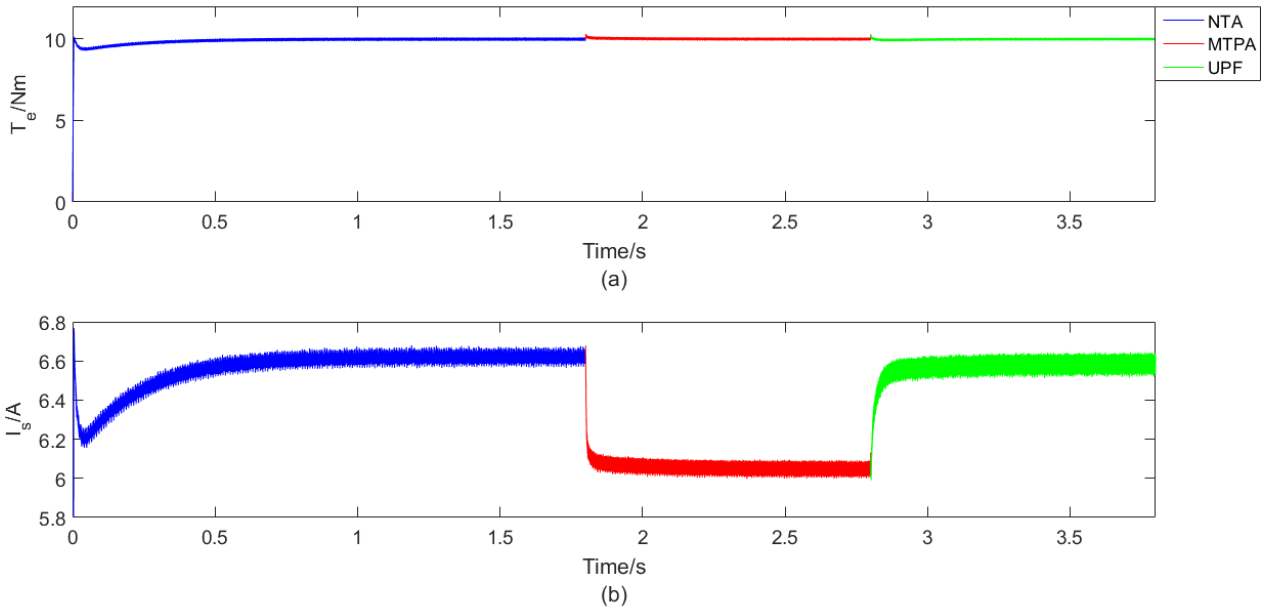

Figure 43: (a) regulation of developed torque (b) stator current magnitude required for torque regulation

The Simulink model does not incorporate core and windage losses of the IPM. Losses associated with the coupling of the generator and the gas turbine are also not taken into consideration. A control strategy that minimises all the losses associated with the generator-gas turbine system will be discussed in chapter 6.

4.3 Load-side control

In this section load-side control strategies are simulated for grid-tied, isolated and unbalanced grid conditions.

4.3.1 load-side current control in grid-tied operation

In figure 25 (a) the grid-tied current control loop is the fastest out of all the control loops. The small inductance allows for fast variations of current from small converter voltage changes. To test the performance of the current loop a DC power source replaces the DC-link as shown in figure 44.

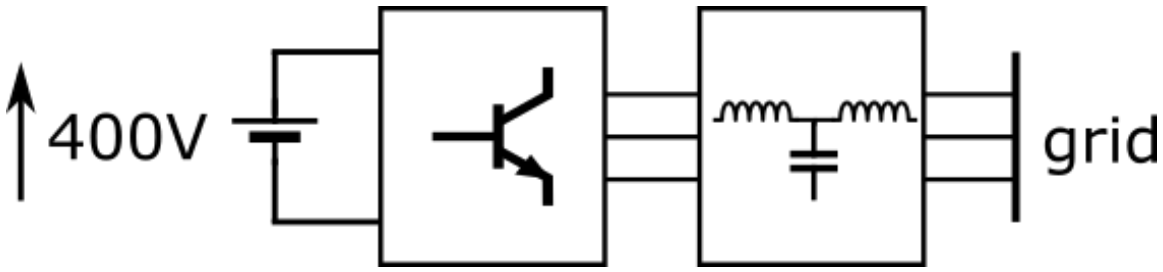

Figure 44: Load-side system setup for grid-tied operation

In figures 45 and 46 the performance of the control is displayed; the effect of the damping resistor is also made apparent from the simulations. Figure 45 shows the current response using a damping resistor of 5Ω and figure 46 shows the response using a damping resistor of 100Ω. Figure 45 displays large current oscillations that can result in the destabilisation of the load-side system. For this reason, multiple resistances were simulated and a damping resistor of 100Ω displayed acceptable performance.

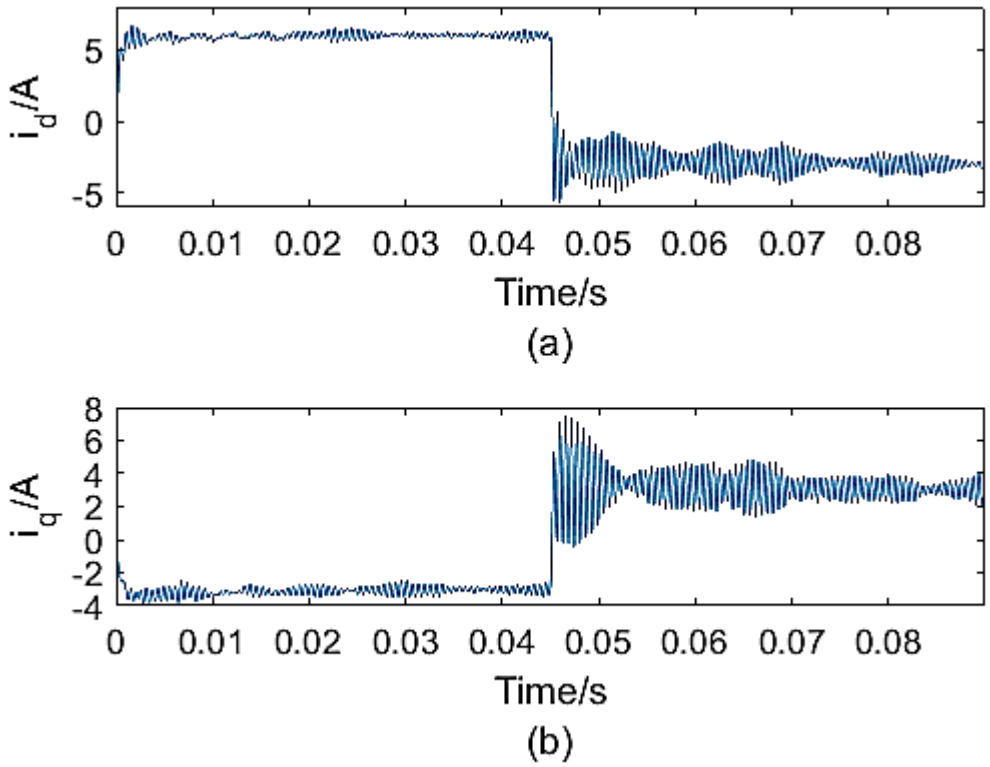

Figure 45: current response using damping resistor of 5Ω (a) d-axis current (b) q-axis current

The current response from figure 46 is within the same order of magnitude as the response shown in figure 25 (a). This ensures a quick current response that can later be used as an inner current loop to regulate the DC-link voltage. According to equation 2.40 and 2.41, the controllability of the d-axis and q-axis current is also displayed, which is necessary when

defining the power factor. The delay in the response times as compared to figure 25 (a) is attributed to the delay associated with sampling and switching. The response times of the d an q-axis currents are similar because the synchronous inductances are the same.

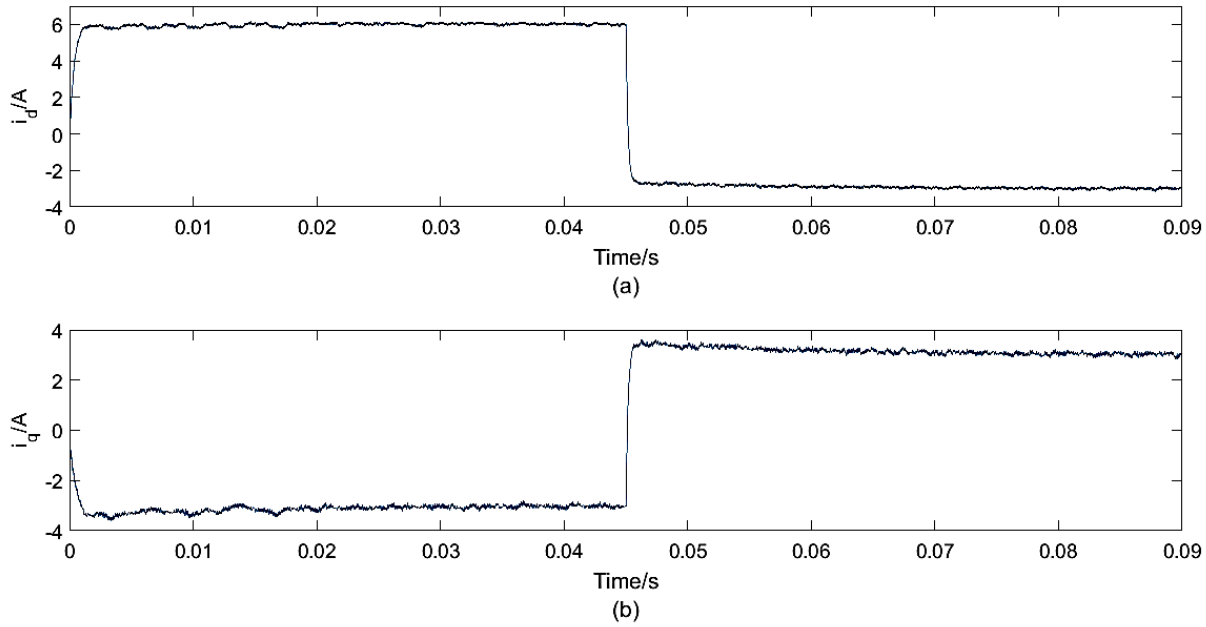

Figure 46: current response using damping resistor of 100Ω (a) d-axis current (b) q-axis current

4.3.2 load-side current control in isolated mode of operation

The load-side current simulations were conducted according to figure 47. The isolated load refers to a resistive load that the load-side system must supply with power. In isolated operation the load-side converter regulates the load voltage. The converter can source as infinite amount of power from the DC source; therefore, voltage regulation can easily be achieved. Voltage regulation will be discussed in detail in chapter 6.

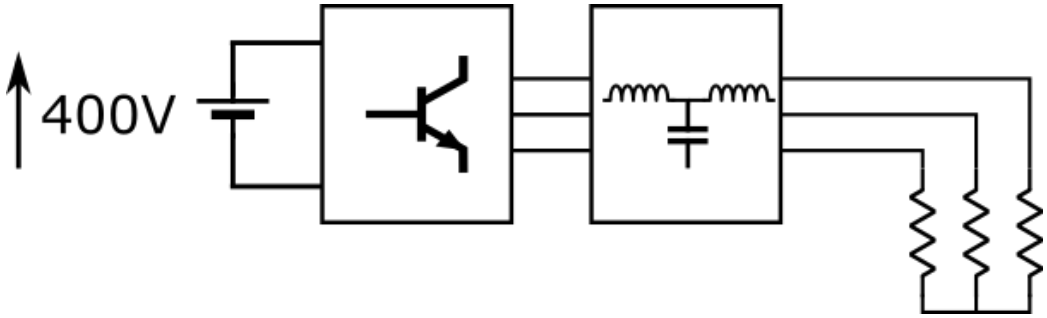

Figure 47: load side system setup in isolated operation

The current response is much slower than response of the current in the of the grid-tied system. The additional resistance from the load provides additional damping the load

currents. This means a smaller damping resistor can be used for the filter. Figure 48 shows the current response from using a damping resistor of 5Ω. The slow dynamics of the current make it difficult for an outer-loop control scheme to be implemented. In [27]-[29], a scheme using the load-side current control as the inner loop control and the DC-link control as the outer-loop control is proposed. However, this would only be successful for a very slow varying DC-link voltage according to the findings of this section. Hence, for a smaller DC-link capacitor, a different control scheme is required, which will be discussed in detail in section 4.4.

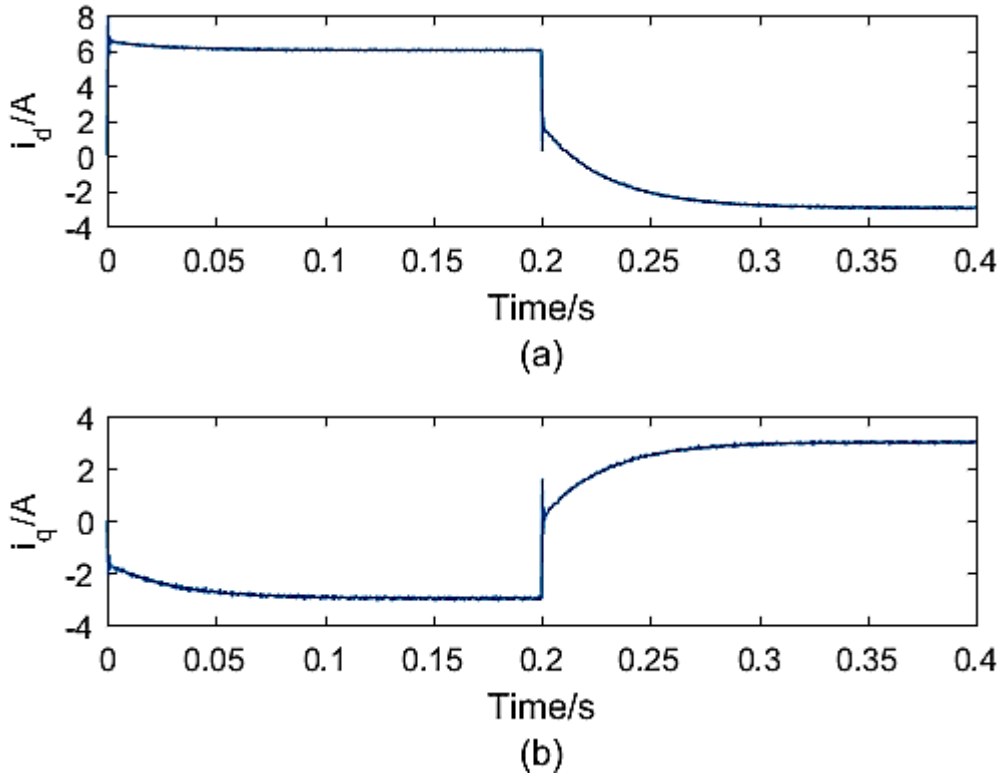

Figure 48: load-side current response in isolated mode of operation

4.3.3 load-side current control during unbalance

In weak or isolated network, grid voltage unbalance can occur because of unequal loading of the phases. This will cause significant oscillations in the d-axis and q-axis current which can hinder the effectiveness of the control system. Oscillations in the current will result in oscillations of the same frequency in the DC-link voltage. The oscillating capacitor current can cause heating of the capacitor and eventually damage it. Figure 49 shows current response during unbalance; phase a, b and c are at 180V, 145V and 120V RMS respectively. A 100Hz component is observed on top of the expected d-axis and q-axis positive sequence values.

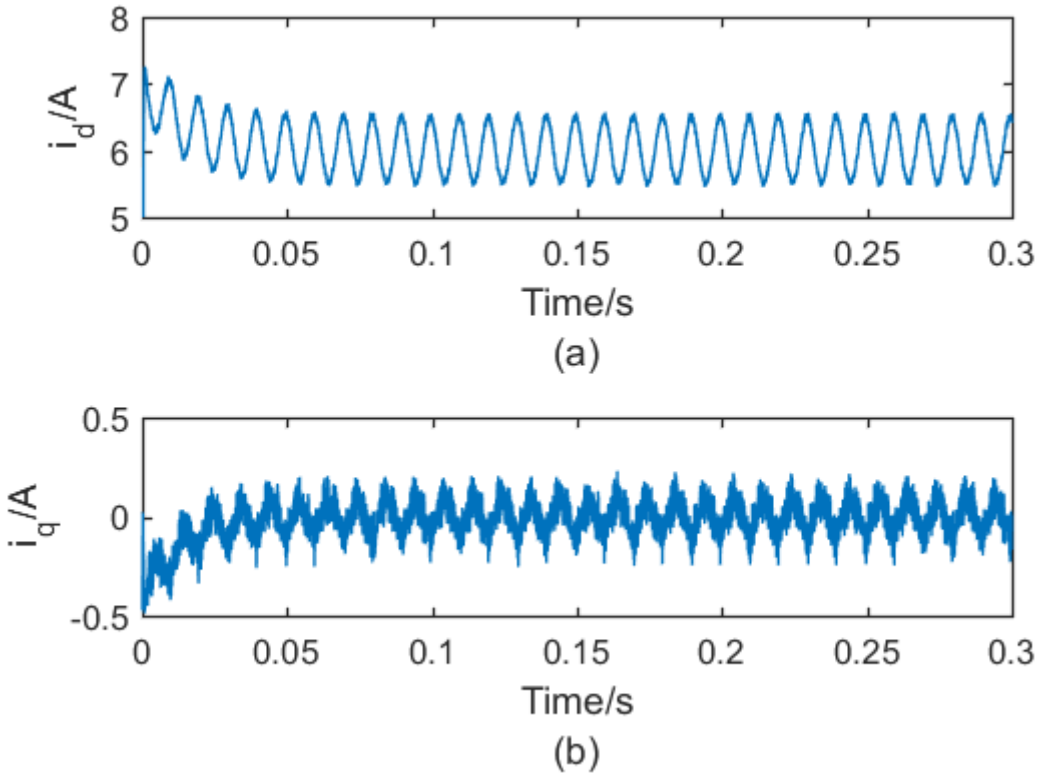

Figure 49: Current responses during unbalanced conditions (a) d-axis current (b) q-axis currents

An RLS algorithm that extracts positive and negative sequence quantities was proposed in section 3.1. The synchronous positive and negative sequence components of figure 49 are given in figure 50. A small negative sequence d-axis and q-axis current component can be observed. The RLS algorithm acts as a filter, producing pure tones at 50Hz and -50Hz.

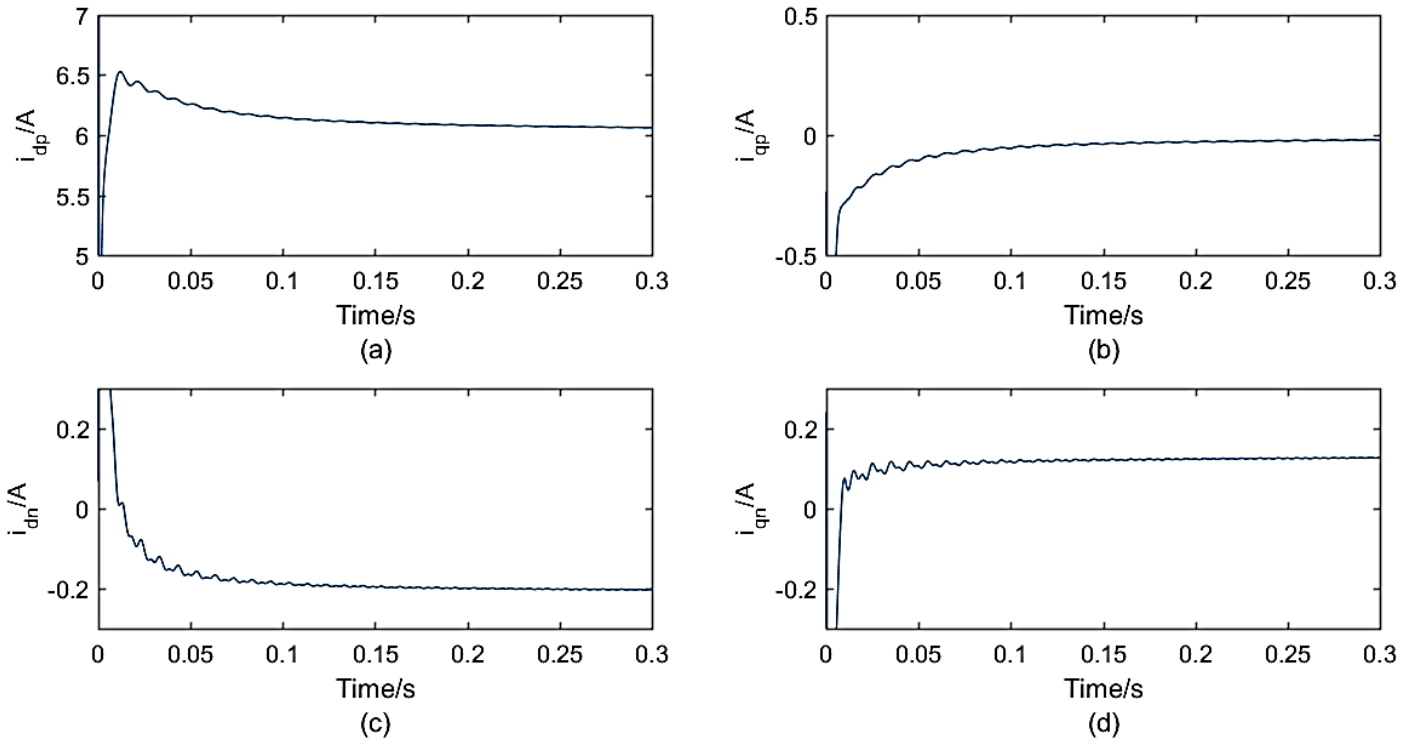

Figure 50: Synchronous components (a) d-axis positive sequrnce current (b) q-axis positive sequrnce current (c) d-axis negative sequence current (d) q-axis negative sequence current

The proposed control scheme during grid voltage unbalance is twofold. Firstly, the unbalanced grid voltage magnitudes must be matched before grid integration, this happens during synchronisation. Doing this minimises the amount negative sequence current in the load-side system. Figure 51 (a) and (b) show the d-axis and q-axis negative sequence components without matching the converter voltages to the unbalanced grid voltages. Figure 51 (c) and (d) show the same quantities which result from matching the converter voltages to the unbalanced grid voltages. The latter shows a significant reduction in negative sequence components.

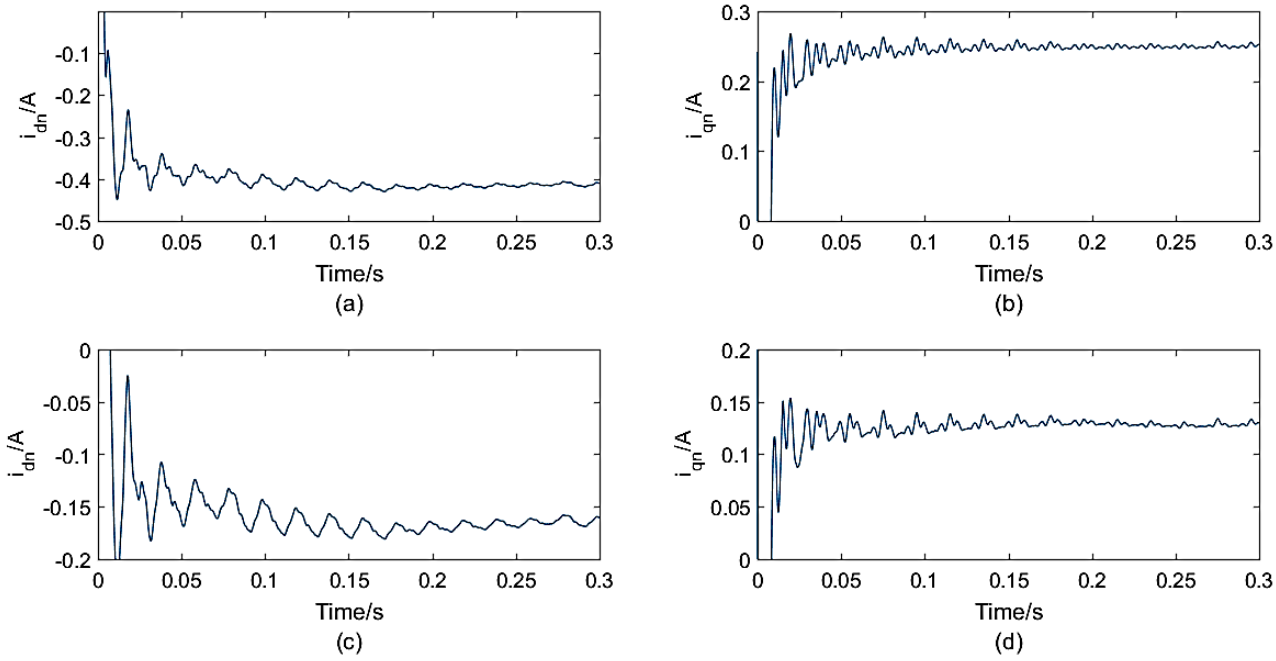

Figure 51: negative sequence synchronous components (a) d-axis current (b) q-axis current (c) d-axis current under grid voltage matching (d) q-axis current under grid voltage matching

The next step is to use the positive sequence grid angle to transform the current into its d-axis and q-axis components. The RLS algorithm can produce an undistorted positive sequence angle without any changes in phase, unlike regular filters. The positive sequence grid angle is required to control the dominant positive sequence current components. This results in balanced phase currents and negative sequence current components are greatly reduced as shown by figure 52.

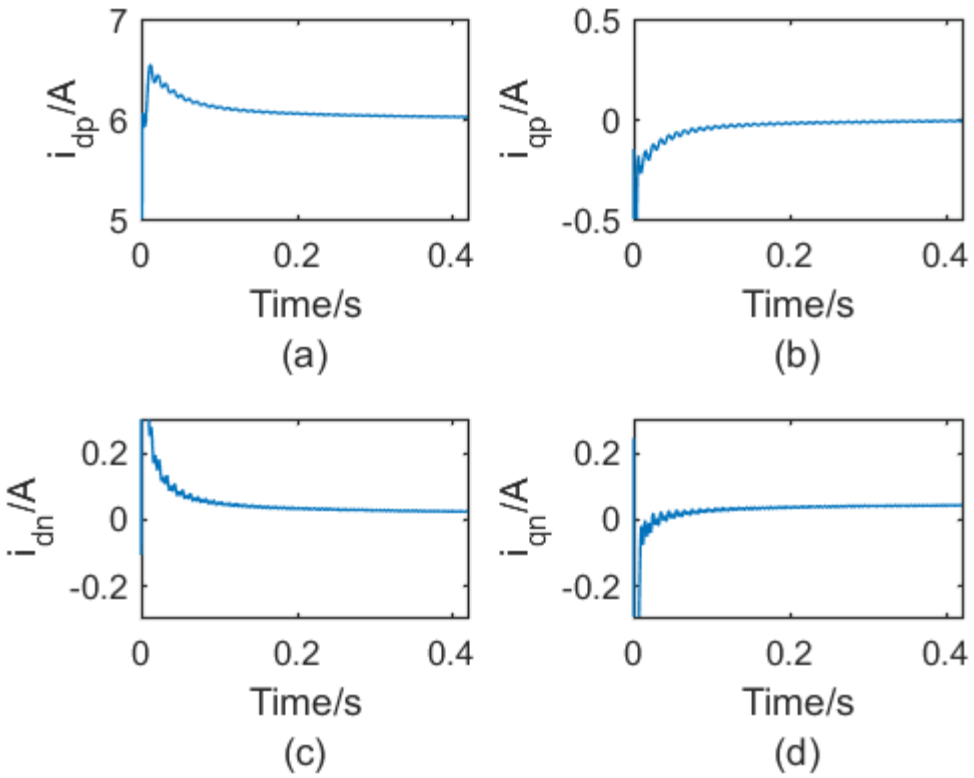

Figure 52: (a) positive sequence d-axis current (b) positive sequence q-axis current (c) negative sequence d-axis current (d) negative sequence q-axis current

Since the converter voltage magnitudes will differ and the currents will be the same in each phase, the power dissipated by each switch pair on a converter leg will differ. This may result in a pair of switches on a phase failing before another pair on a different leg. The d-axis and q-axis converter voltages are given in figure 53. The unbalanced output voltages are represented by the 100Hz component on top of the d-axis and q-axis voltage component. While the RLS algorithm is computationally burdensome on the control system, the implementation is simple. It does not require additional control loops to suppress negative sequence components, meaning converter saturation is less likely and larger grid unbalances can be accommodated than the conventional methods in [30], [31].

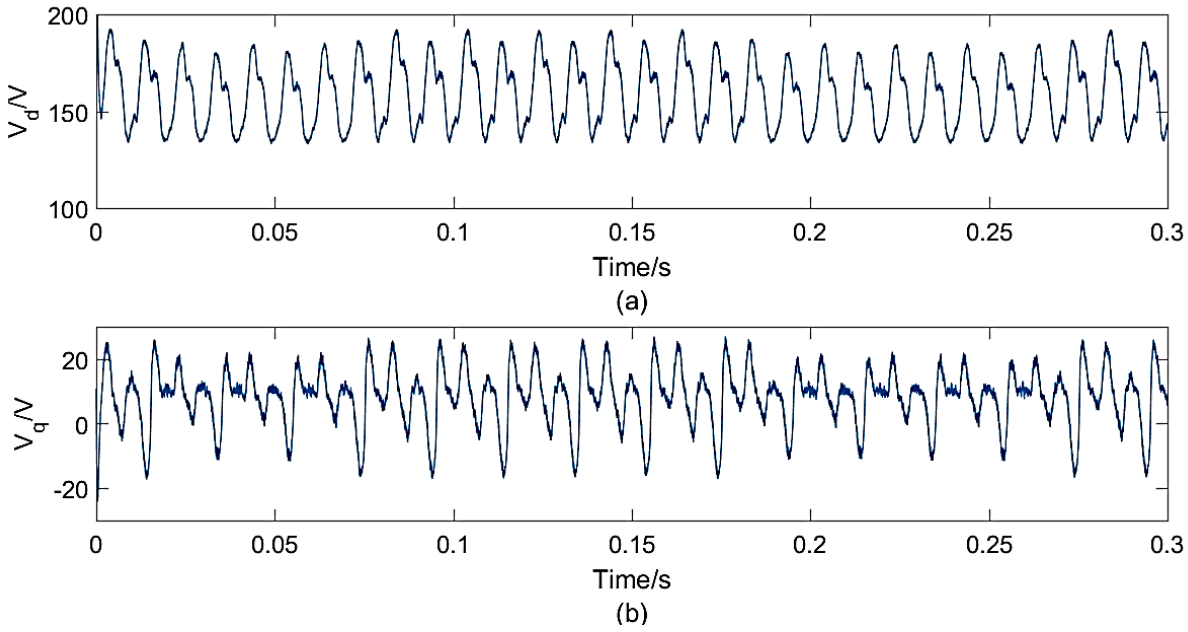

Figure 53: Converter voltages (a) d-axis converter voltage (b) q-axis converter voltage

4.4 Outer-loop control

Usually the load-side is responsible for regulation of the DC-link voltage. Its small inductance allows for a large control bandwidth and fast response times as discussed in section 4.3. However, in instances requiring reactive power compensation from the generator system, isolated operation or during unbalance, it is advantageous to regulate the DC-link through the generator-side. This section highlights the possible outer-loop control arrangements and their advantages and shortcomings.

4.4.1 DC-link voltage regulation by the load-side converter

To begin with, the load-side converter regulates the DC-link. Figure 54 shows the DC-link voltage response when the load-side is in grid-tied mode. Power is delivered to the grid at unity power factor. This ensures that the DC-link is regulated using the minimum current required to do so. The settling time in figure 54 is within the same order of magnitude as in figure 25 (c). The DC-link voltage response is significantly slower than response of the grid currents in figure 46. This ensures a smooth transition of the DC-link voltage to its reference value.

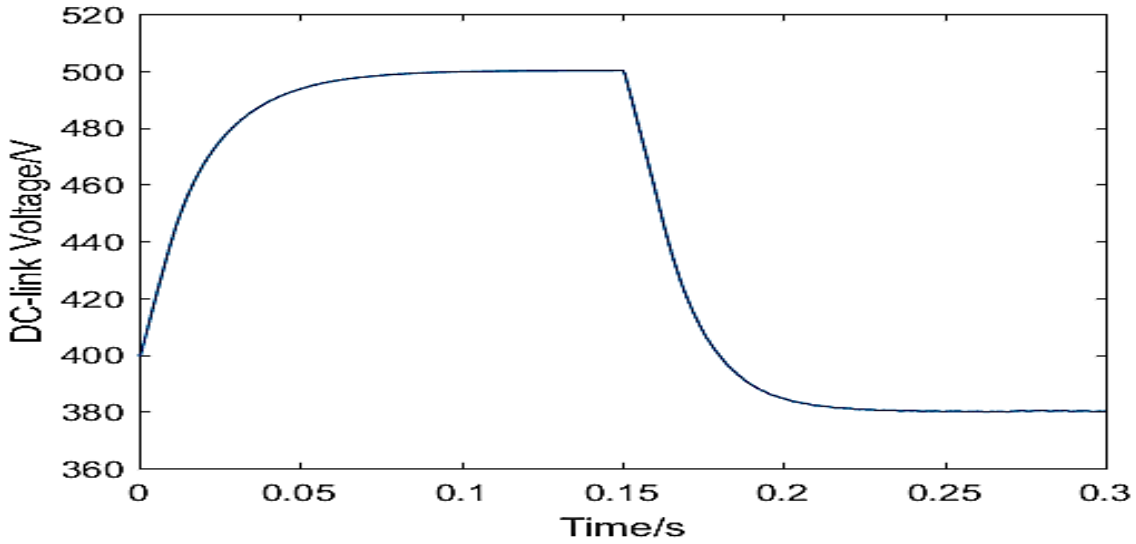

Figure 54: DC-link voltage step response

Active power is used to regulate the DC-link voltage. As stated in equations 2.40 and 2.41 the reactive and active power are proportional to the d-axis and q-axis load currents respectively. In the case of reactive power compensation, the q-axis current is non- zero. A lower power factor will result in higher load currents because of the additional active power producing current component (d-axis current) required for DC-ink voltage regulation. Figure 55 illustrates this; the power factor changes from 1 to 0.707 at 0.05 seconds and the DC-link voltage drops. To stabilise the DC-link voltage at constant voltage, the control increases the magnitude of the load current. To avoid converter saturation the current magnitude is limited to 7.5A. The DC-link voltage experiences a dip but stabilises at a lower voltage than the setpoint.

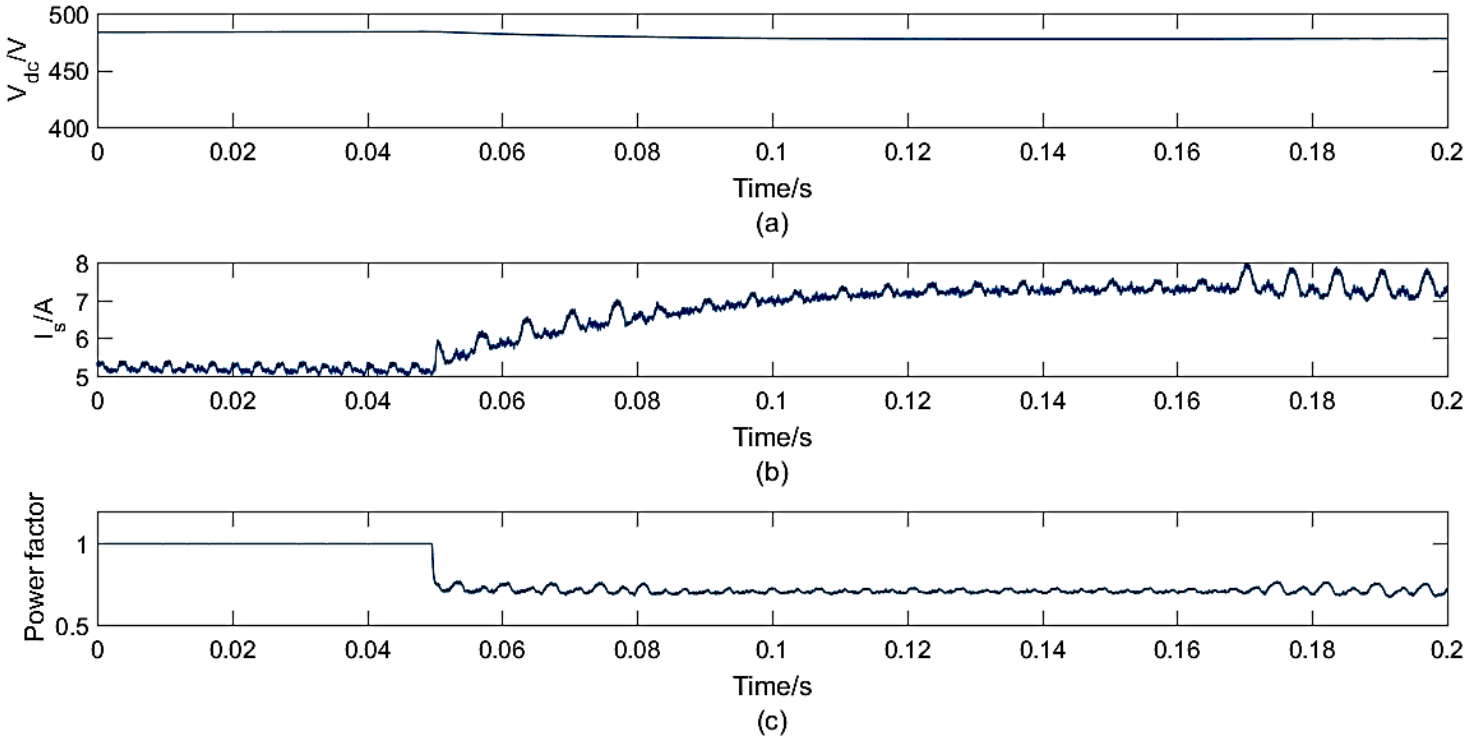

Figure 55:(a) DC-link voltage change (b) stator current magnitude change (c) power factor change

When the system is in isolated mode of operation, the outer-loop control must supply the load with power at rated voltage regardless of the size of the load. The outer-loop control in this case must be the load voltage control. However, this leaves the DC-link voltage unregulated. In[27]-[29] a scheme that alternates the outer-loop control between regulating the DC-link voltage and regulating the load voltage is presented. When the DC-link is above a threshold voltage the outer-loop control regulates the load voltage. When the DC-link is below the threshold voltage the outer-loop control regulates the DC-link. The problem with this controls scheme is that at certain instances the DC-link voltage is left to float. For small DC-link capacitors a fast controller-converter combination would be required. For these reasons, the next section explores controlling the DC-link from the generator-side.

4.4.2 DC-link voltage regulation by the generator-side converter

The generator can regulate its power production by varying its developed electromagnetic torque. The stator currents have slow dynamics according to figure 48. Therefore, the dynamics of the DC-link voltage must be at least 10 times slower. Figure 56 shows the successful regulation of the DC-link voltage by the generator-side system. The DC-link voltage

is controlled to 450V and then 400V. During each transition the electromagnetic torque varies to ensure DC-link voltage regulation.

UPF control is implemented because it has the lowest DC-link utilisation of the control strategies. The large generator inductance and resistance will result in a noticeable voltage drop across the stator. Therefore, the DC-link utilisation must be kept low to prevent converter saturation. The load-side system is now able to regulate the load voltage or to implement reactive power compensation without the added burden of DC-link voltage regulation.

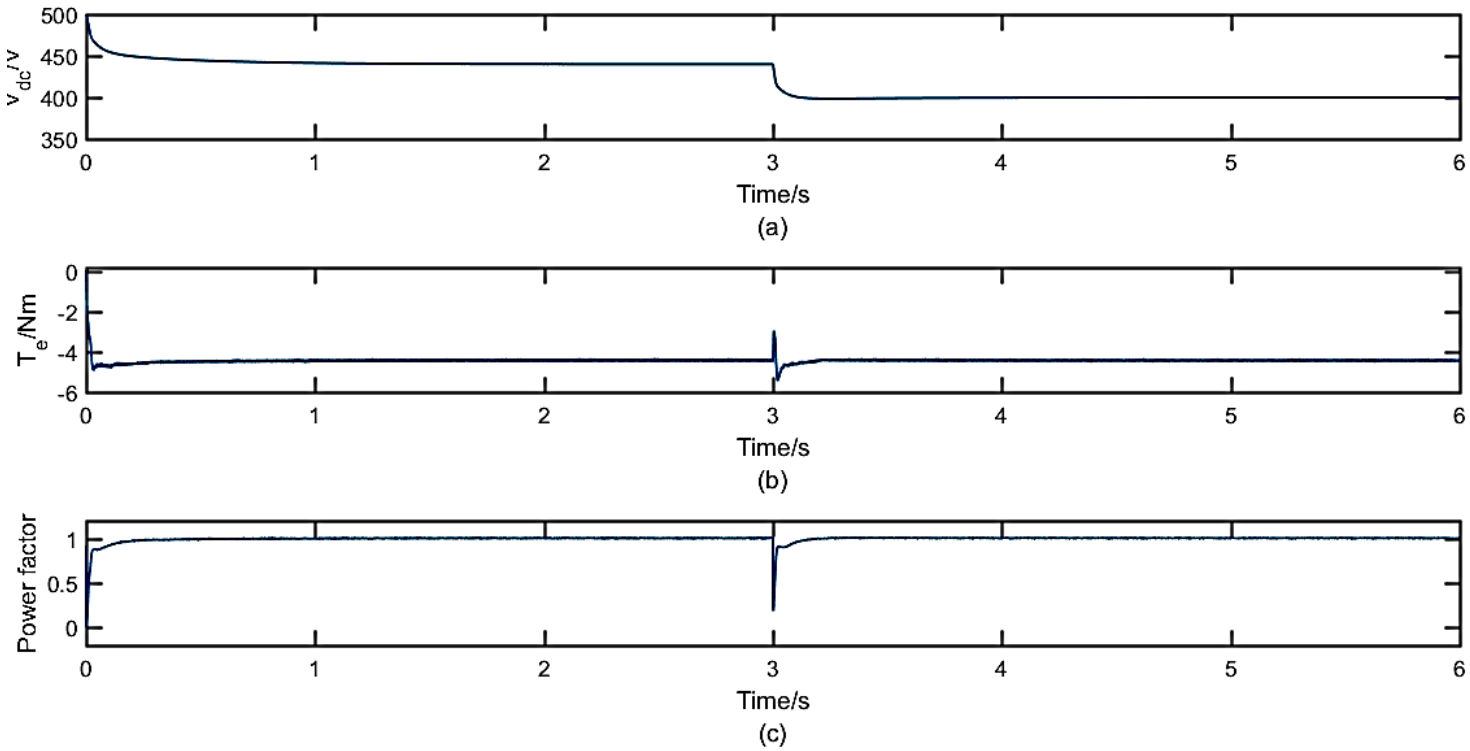

Figure 56: (a)DC-link voltage regulation (b) developed electromagnet torque (c) Power factor

Chapter 5

5. Experimental Setup

Part of the deliverable of this project is to produce a back-to-back converter that can control a gas turbine generator; figure 57 shows the converter. Additional peripheries had to be designed to interface a controller with the converter. They will be explained in the following sections.

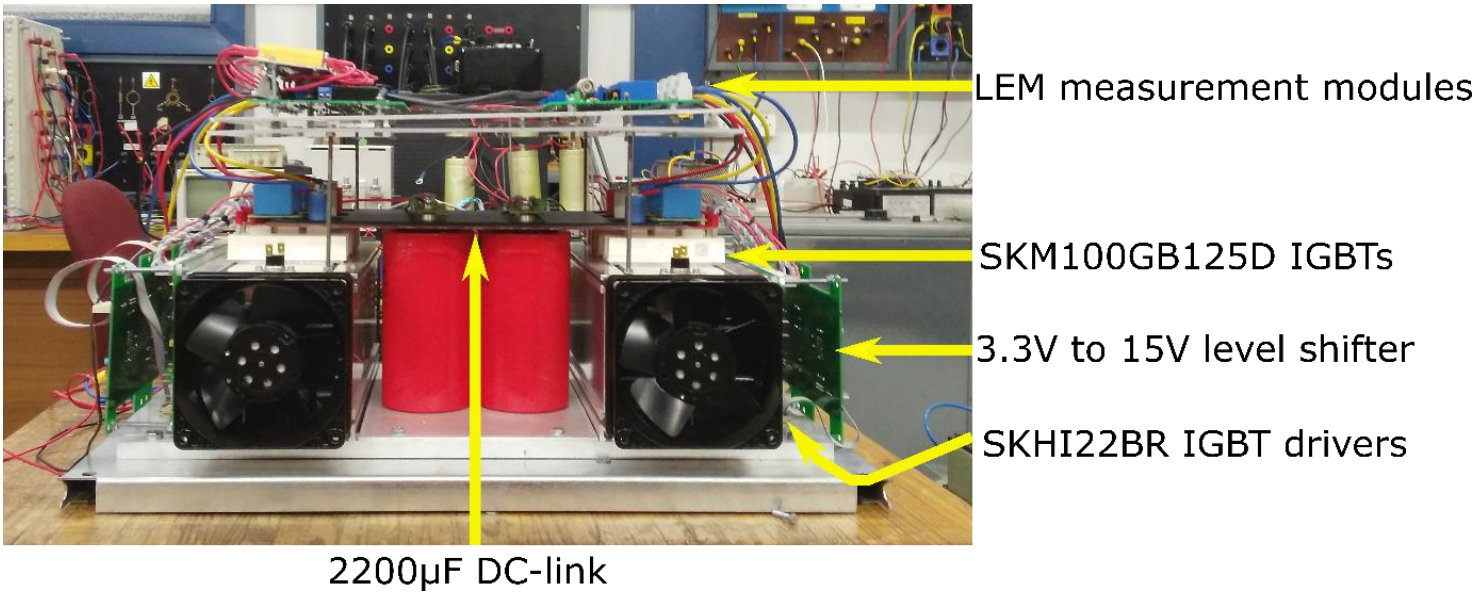

Figure 57: Converter with peripherals

The converter was integrated into a cabinet along with the protection and peripherals required for this type of application. The LEM voltage and current measurement modules are placed above of the converter with an aluminium plate providing shielding between the two. The Relays, LEM modules and IGBT drivers require a 24V, 12V and 15V supply respectively. Line filters are place on the power supplies to limit crosstalk, particularly from the switches and the operation of the contactors onto the LEM module power supply. CT's are used to display the current outside of the cabinet. The load-side filters are placed at the bottom of the cabinet. Figure 58 shows a photo of the set-up.

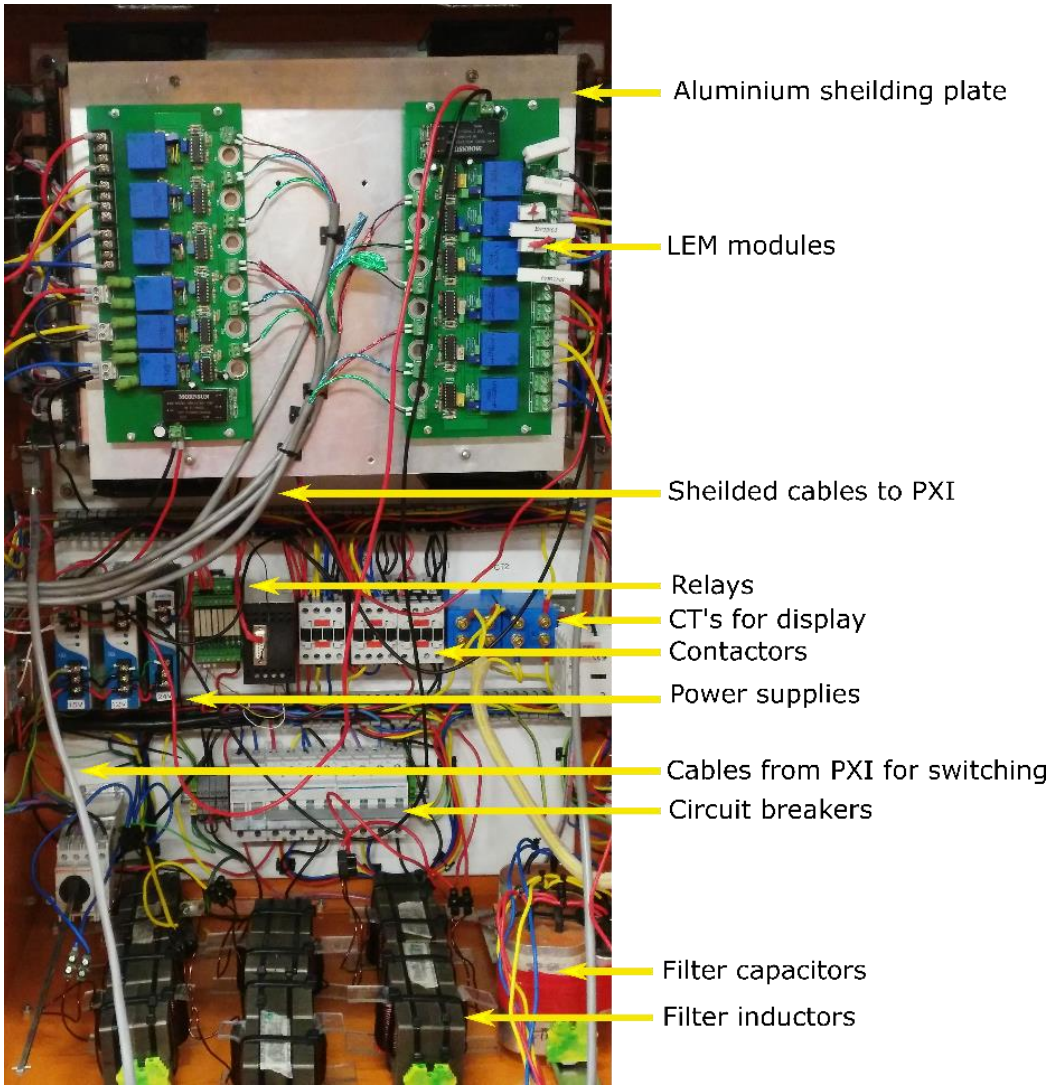

Figure 58: Converter system cabinet

The isolated load and grid are represented by a variable resistor bank and a three-phase variac. The variac is required to step the voltage down from utility voltage. A DC-machine is used to emulate the behaviour of a gas turbine. The DC-machine can accept both armature voltage and current references, hence, its speed and torque can be controlled. In [15], [37], it is shown that a DC-machines has a significantly higher inertia than a gas turbine of the same rating. Thus, emulation of a gas turbine by a DC-machine of the same rating is unlikely to work because of the high torque required. For this reason, a DC-machine with twice the rating of the IPM is used. The generator-side and load-side control will ensure over-loading of the generator or the load does not occur. The DC-machine and the IPM are coupled together. An encoder is secured in place by rod protruding from the rotor of the IPM and a bracket fixed to the IPM's outer casing. Figure 59 illustrates this arrangement.

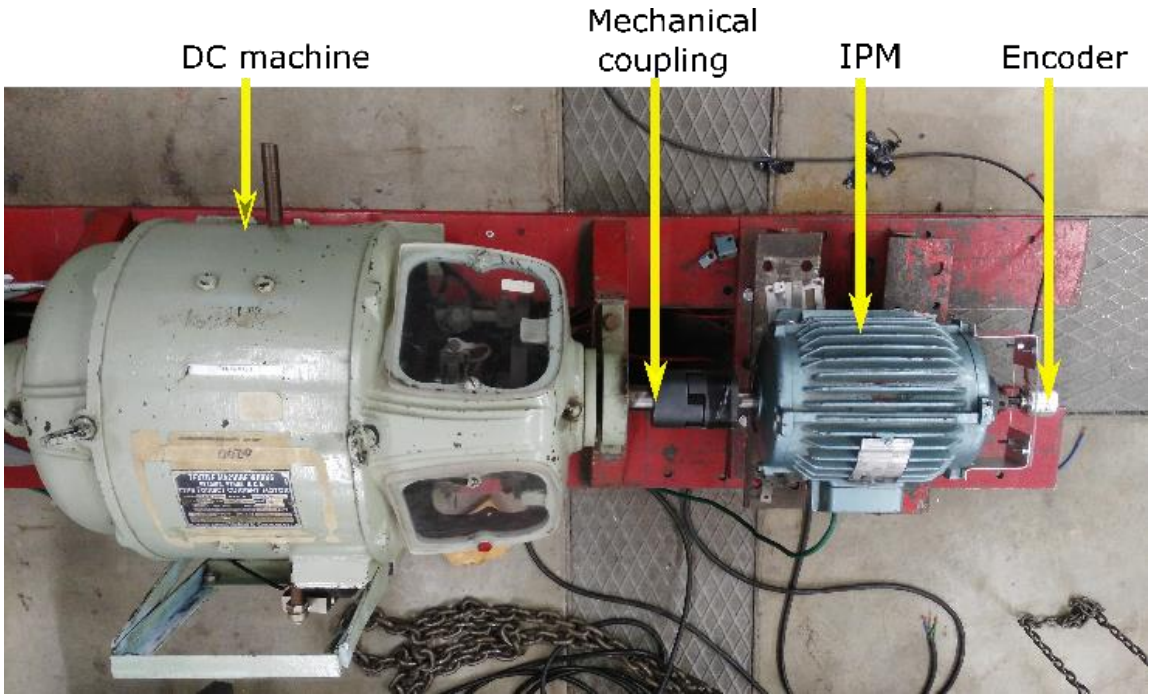

Figure 59: DC-machine and IPM

5.1 Voltage and current measurements

The LA-25 current transducers and LV-25 voltage transducers are used for voltage and current measurements. They work as current transformers, transforming the high generator and load currents on the primary side to lower currents on the secondary side. A measuring resistor R_m is placed along the path of the secondary current so a voltage measurement V_m can be read. A measurement voltage is required because the ADC's of the PXI can only read voltages. R_m is a variable resistor, and acts as a gain that varies V_m. An illustration of their basic operation is given in figure 60. The isolation provided by the current transformer protects the PXI from high power signals.

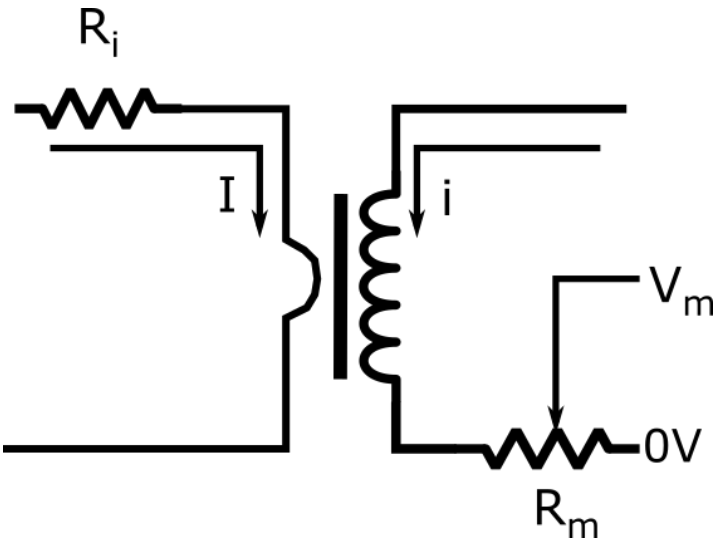

Figure 60: LA-25 and LV-25 operation

5.2 Push-pull differential encoder

The encoder used is an RE36 differential incremental encoder. The operation of an encoder has been explained in section 3.1.1, however, its interfacing with the PXI will be discussed here. The encoder produces three pulses X, Y and Z as well as their complimetns $\bar{X}, \bar{Y}$ and $\bar{Z}$. The high frequency switching of the converter emits significant electromagnetic radiation and results in the electromagnetic interference of the encoder outputs. It is safe to assume that all 6 outputs from the converter will pick up the same interference from the converter. By subtracting the signals from their compliments, noise and interference is cancelled from the result. The result will be three signals twice the amplitude of X, Y and Z. Figure 61 illustrates the operation of a differential transmitter and receiver.

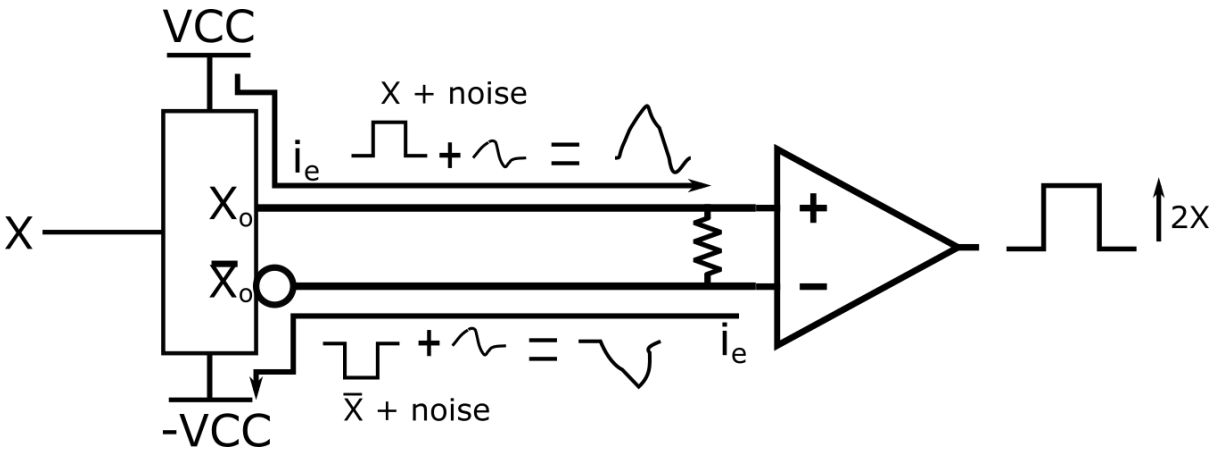

Figure 61: Differential transmitter and receiver of the signal X

The push-pull refers to current amplifier used to drive the encoder, which is illustrated in figure 62. The current amplification makes the signals less susceptible to interference, this is necessary when the cable length from transmitter is receiver is long.

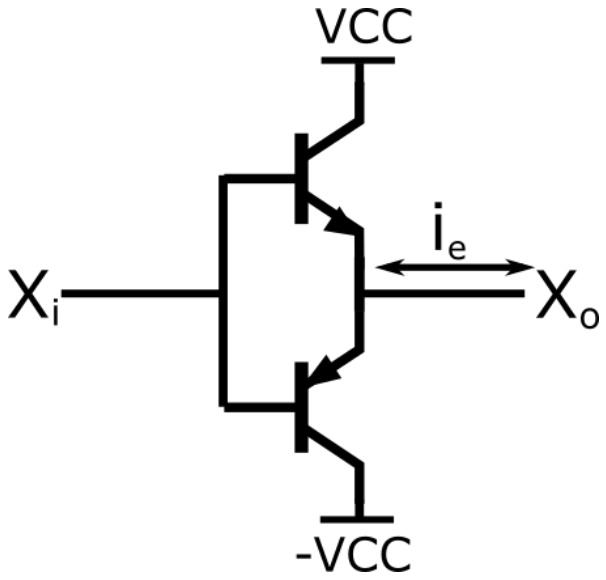

Figure 62:Push-pull amplifier

The transmitter of the encoder is built into the encoder casing, the receiver had to be made onto a veroboard as seen in figure 63. The AM26LS32 chip is a differential receiver that converts differential signals from the encoder transmitter to non-differential ones required by the PXI. The voltage regulator powers the AM26LS32 and ensures an output of 5V, required by the PXI's digital inputs.

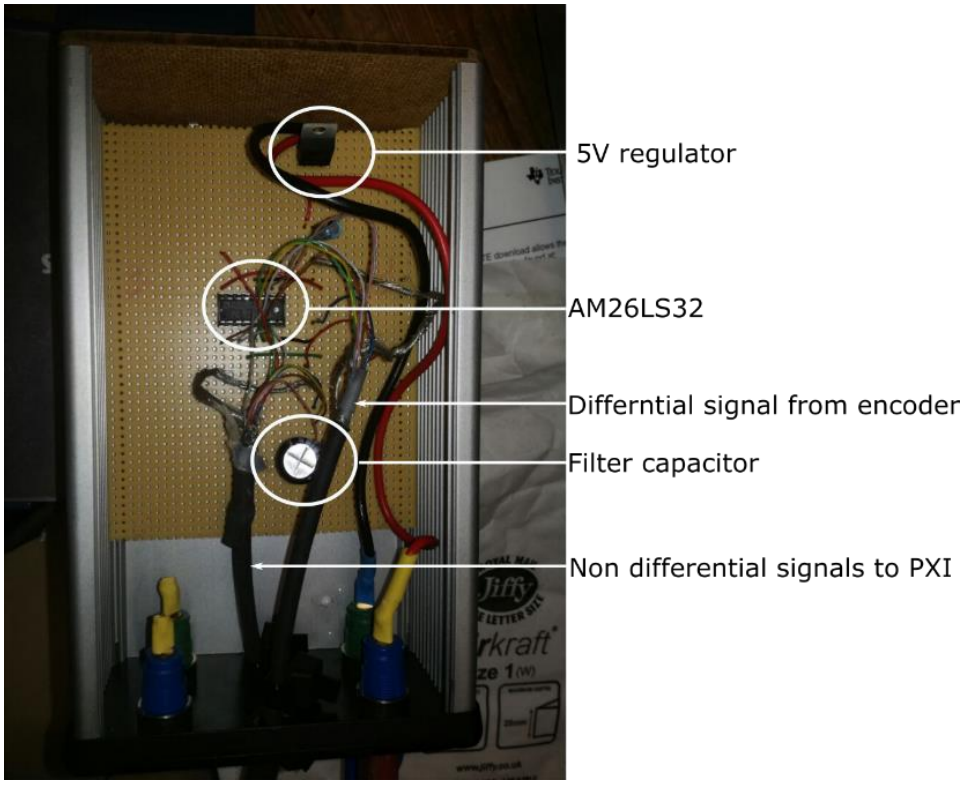

Figure 63: Differential receiver

5.3 IGBT switches and drivers

The SKM100GB125D IGBTs are used in the converter and the SKHI22BR drivers are used operate the them. The drivers allow the user to set gate input resistors, switching dead time and the V_{CE} threshold. Input resistors determine the speed at which the converter turns on and off. The resistors are in the path of the base current of the IGBT, low resistances results in fast responses. However, the lower the resistance the higher the base current and the greater the probability of overshoot and oscillations on the converter output. Figure 64 displays the output voltage of an IGBT with an input resistance of 4Ω. Oscillations are observed on the converter output, which will propagate to the DC-link voltage, the load-side current and generator-side current.

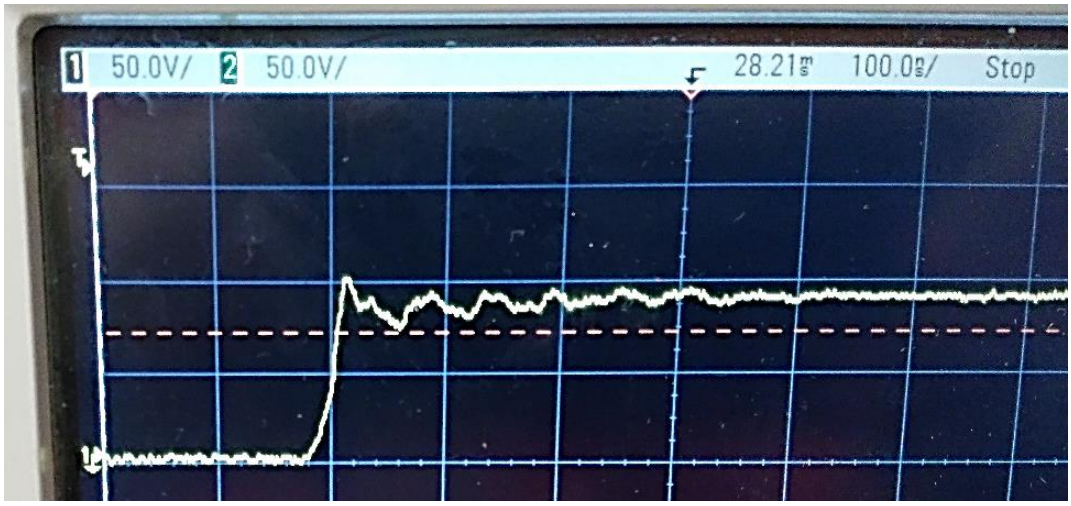

Figure 64: IGBT output for an input resistance of 4Ω

The IGBT does not instantly turn on and off. The behaviour of the collector and emitter can be likened to having a capacitor between the two. The SKM100GB125D takes 80ns to switch on and 360ns to switch off. It is important that when choosing a switching dead time that the delays in the switching are factored in. The switching dead time refers to a delay imposed by the driver in turning-on an IGBT. This results in a period where both the top and bottom switches on a single converter leg are off and acts as a precaution to prevent short circuits across the DC-link capacitor. A noticeable delay by the controller will affect the control the generator-side and load-side systems. The smallest dead time that can be set is 700ns; it is chosen to minimise the effect of the delay on the control system. Figure 65 shows the voltage across the top and bottom switches on the same converter leg. The dead time is consistent with the setting on the driver. The build-up of voltage across each switch is like that of a capacitor charging, thus causing a delay in the voltage build-up across the emitter and collector. The dead time is large enough to span the switches' on and off times, to the point where the only delay seen by the system is the dead time imposed by the driver. The dead time and switch-off and on times could not be included in the Simulink models in chapter 4. This will result in additional delay during the experiments.

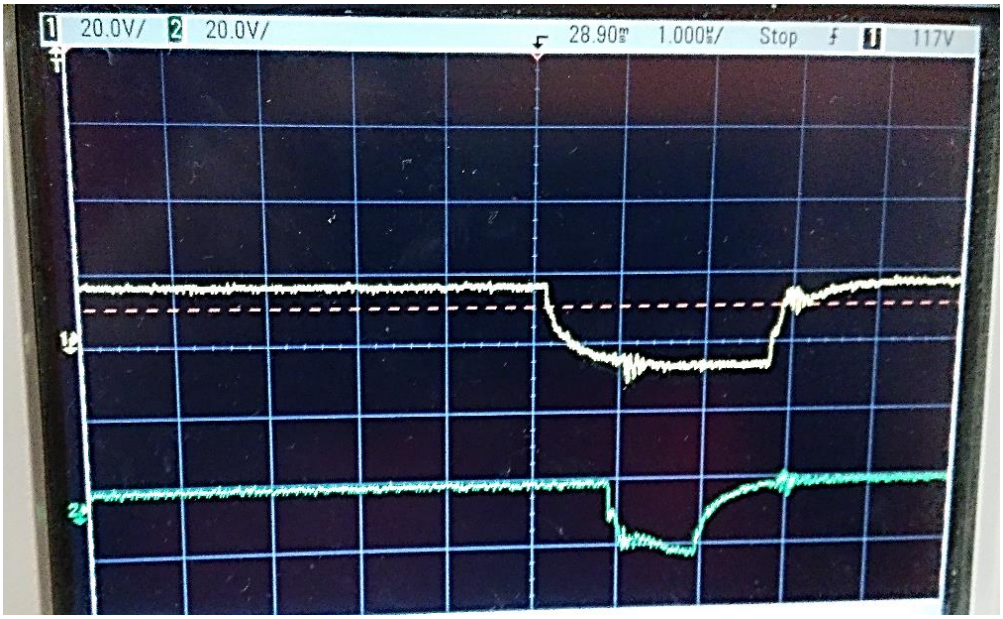

Figure 65: Top and bottom switches' on and off times

The V_{CE} setting on the drivers monitors the collector emitter voltage and is used to recognise shorts and sudden changes in current. If the voltage across the collector and emitter (V_{CE}) decreases too rapidly an error signal is produced and IGBT switching ceases. The rate at which V_{CE} decreases is set by an RC circuit, if V_{CE} dips beneath this value an error is produced.

5.5 Interfacing of drivers and PXI

The SKHI22BR driver receives switching signals from the PXI, which come in the form of a 3.3V TTL signal. Low voltage digital signals are susceptible to electromagnetic interference from the converter. During the experiments it was discovered that a higher digital signal level is required. The SKHI22BR driver allows for inputs of 3.3V and 15V, therefore the 15V input is chosen. To interface the PXI with the driver boards a voltage level shifting board was designed in kiCad for this project. Figure 66 shows the level shifter; the schematic is given in the appendix B. The switching signals from the level shifter take 1ns to reach their steady state value. This means their rise and fall times will not cause any notable delays in the switching of IGBTs.

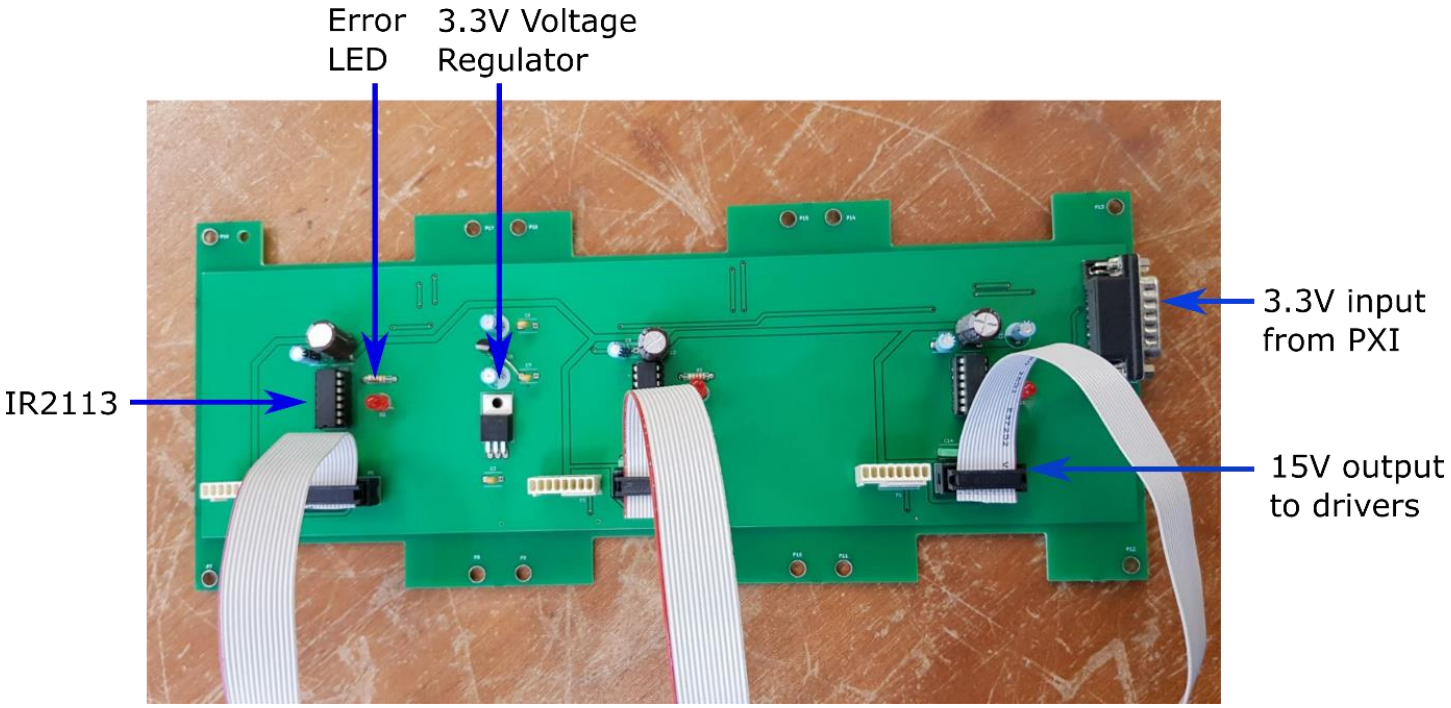

Figure 66: Voltage level shifter board

5.6 Synchronous sampling

Synchronous sampling is used in sampling all voltages and currents. This method synchronises the instances of switching and sampling. Sampling is not taken during converter switching to avoid interference. This also ensures that the control action at an instance is not sampled within the same instance, which would give a false impression of a much more controlled variable. Therefore, sampling in one sampling period will affect the control action in the next period. Sampling is triggered in the middle of a switching period to achieve these objectives. The implication is that the switching and sampling periods are the same and that the control algorithm has half a period to start, finish and implement the control action. Secondly, sampling in this manner is the equivalent of sampling an averaged value over a sampling period. This is advantageous as the control system will respond to lower frequency excursions of voltage and current without the need of physically filtering these quantities[61]-[63]. Employing filters can degrade the effectiveness of the control system because of added delays and unintended phase shifts. The Yokogawa T1800 was used to acquire the traces in figure 67. The top three traces show the on times of the three legs, while the bottom trace shows the trigger that initiates sampling and the control algorithm. The duration of the trigger pulse represents the duration the control action must sample and determine a control action. Note that sampling takes place when there is no switching change.

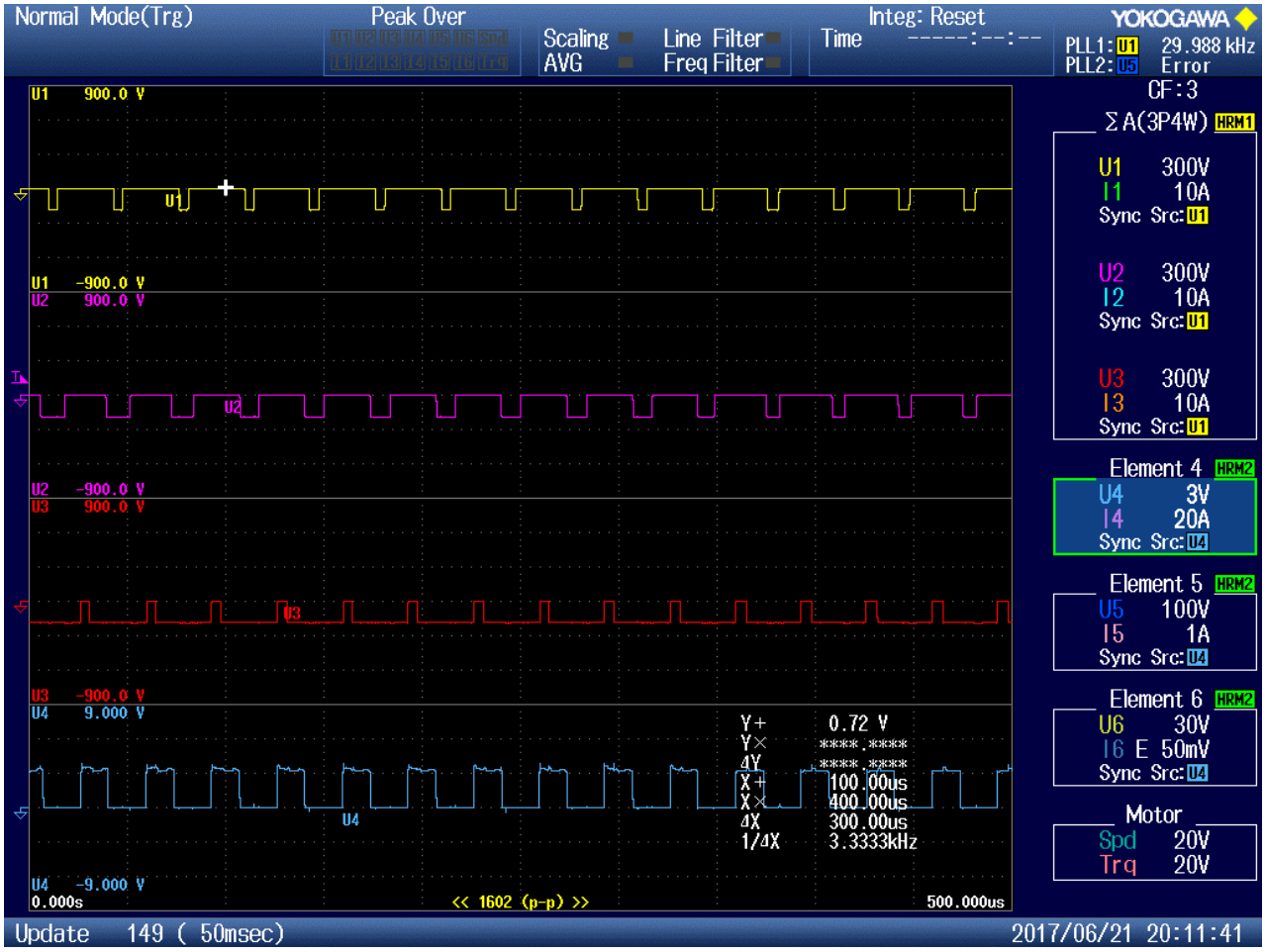

Figure 67: switch on times and sampling trigger pulse

5.7 Allocation of controller resources

The controller used in this thesis is the PXI-8840. The controller comprises of a CPU, a data acquisition card and an FPGA. The FPGA runs on 40MHz clock, and can implement instructions in parallel. The fast clock makes it ideal for handling time sensitive operations. For this reason, it is used to implement the control algorithm and the protection protocols. The cascaded structure of the control loops requires guarantees in the rate of execution of both the inner and outer-loops. Polling is used by the protection protocols to frequently check the state of the currents and voltages in the system. The rate of polling is defined per protection protocol and never changes throughout its operation to guarantee that state of the system is frequently being checked. The CPU serves as an interface between the user and the FPGA and data acquisition card. It is also used to run the RLS algorithm because it does not fit onto the FPGA. The emulator code is also run on the CPU. The CPU offers very poor timing resolution

as compared to the FPGA. The timing resolution also worsens with the amount of code running on the CPU.

Chapter 6

6. Experimentation

This section covers the experimental lab implementation of the concepts mentioned in previous chapters. It should be noted that the while the different systems are discussed separately, all parts of the system are in operation in each experiment. This ensures the practicability of the techniques employed because their impact on the entire the system can be observed. The logging of data is done online in Labview and takes up resources from the CPU. The sampling period is limited to 1ms to prevent a degradation in the operation of the CPU. The Yokogawa T1800 is used for power and harmonic analysis. The sampling rate of the Yokogawa is 2M/s. The Turbine speed is found to vary slowly during the experiments. Therefore, it is reasonable to assume that the electromagnetic torque and the mechanical input torque are equal according to equation 2.26. A torque transducer is used to measure the mechanical torque.

6.1 Gas turbine emulator

The ideal performance of the gas turbine emulator would result in a response like the simulated responses in figure 32 and 33. However, the simulation does not consider the processing speed of the controller. The emulator code runs on the PXI CPU in a control loop. The maximum rate that the loop can execute was 300µs. This causes a delay in the control signals sent to the drive of the DC-machine. The DC-machine's response under varying load conditions is given in figure 68. The speed of the DC-machine shows similar speed regulation to figure 33, with little deviations in speed when loading. Even with a load change of 300% at 14 seconds a small speed deviation is observed, due to the gradual loading of the gas turbine.

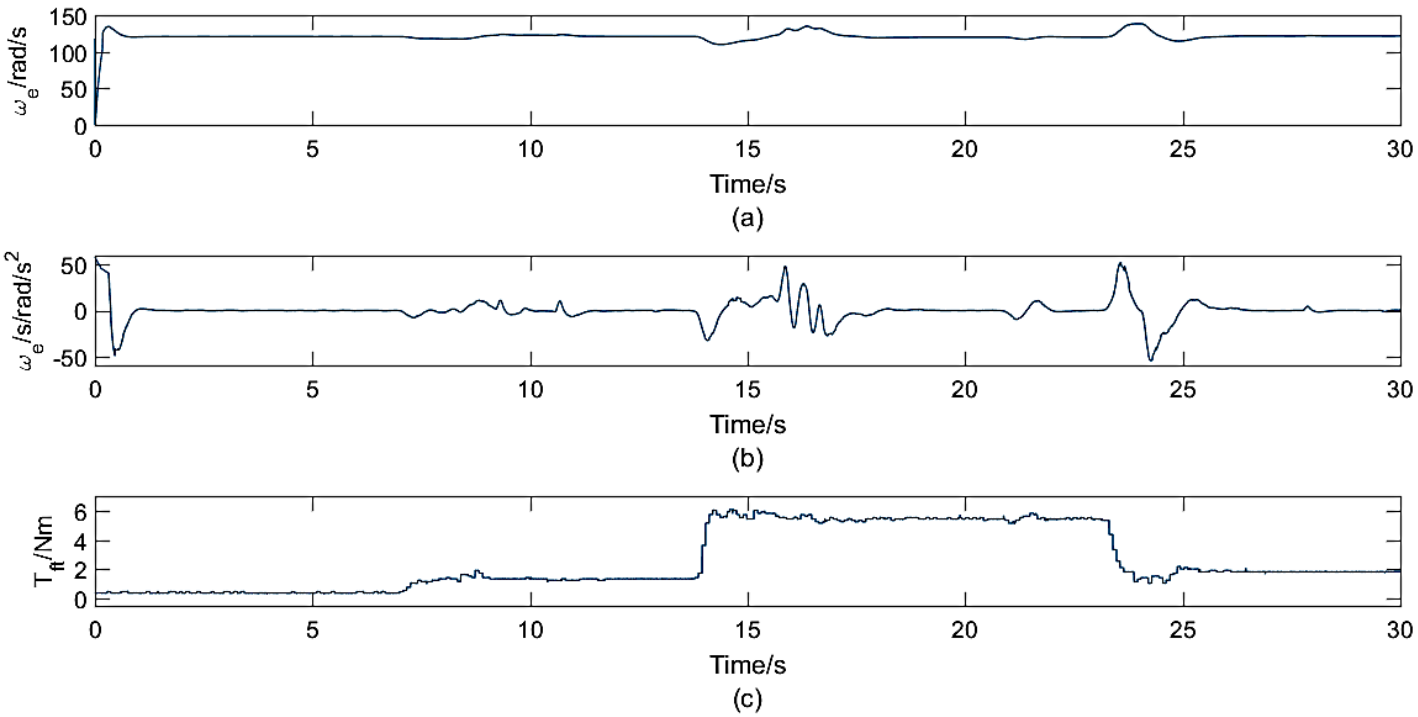

Figure 68: DC-machine (a) speed regulation (b) acceleration regulation (c) Torque response

The error between the speed of the DC-machine and its reference speed according to the gas turbine model is shown in figure 69. The error can be attributed to the slow loop rate of the emulator code running on the PXI CPU. The most effective way to mitigate the error without changing the Rowen model is to schedule the loading of the DC-machine gradually. The error that results from a load increase of 100% at 7 seconds is significantly smaller than the error that results from a load change of 300% at 14 seconds. The load changes of 300% and results in a peak error of 3 rad/s, which gives a maximum speed error of 2.5%.

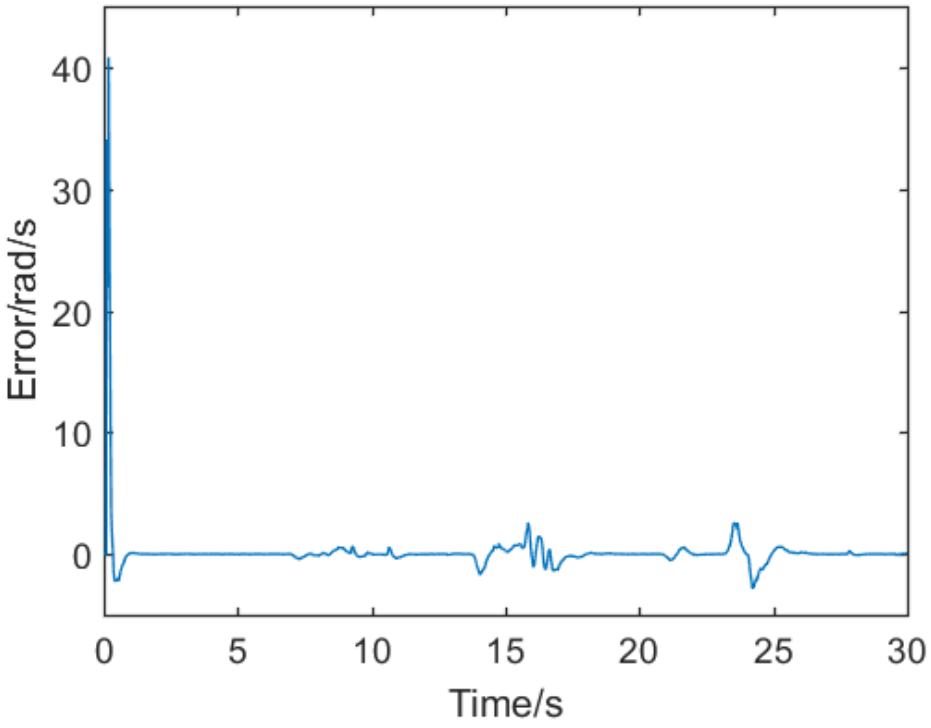

Figure 69: error between DC-machine speed and emulator model reference speed

6.2 Generator control

At the operating speed of 120rads/s, the losses are recorded at no load to observe the core losses, windage losses and mechanical losses. The total losses amount 72W. The losses are subtracted from the measurements taken during the experiments conducted in this chapter. In this section the different control strategies are explored as in chapter 4 and finally a minimum loss control scheme is developed.

6.2.2 Generator current control

The successful control of generator currents is shown in figure 70. The d-axis current references are always negative to avoid saturating the machine. The current responses are slower than those in section 4.2.1. A contributor to the additional delay is due to the dead time mentioned in section 5.3, however, a significant portion results from filtering. Significant measurement noise is picked up from the LEM modules due to the high frequency switching. If the measurements are not filtered, the control action could react to false high frequency measurement excursions. Therefore, a second order digital Butterworth filter is used to filter voltage and current measurements. The consequence of the use of a digital filter is a large delay in the acquisition of the measured value by the PI controller. A Butterworth filter is also

used on the DC-link voltage; therefore, the delay is also transferred to the DC-link control. As a result, the DC-link voltage response is still more than 10 times slower than the current response. Th DC-link response will be discussed in section 6.4.1

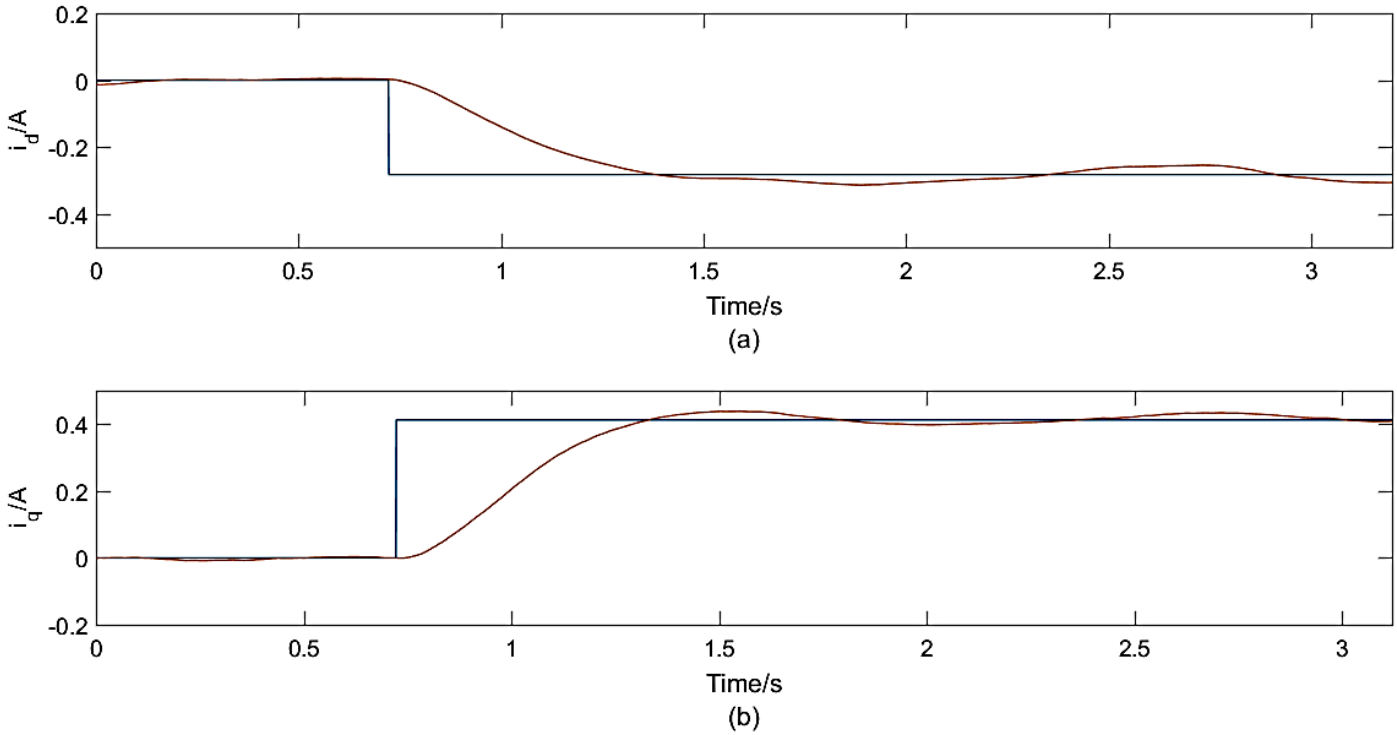

Figure 70: successful control of (a) d-axis current (b) q-axis current

6.2.3 Generator control strategies

Figure 71 illustrates the effect of the torque angle and stator current magnitude on the electromagnetic torque developed by the generator. The presence of a maximum torque developed for each stator current magnitude exist in the same manner as in figure 27 and 36 in sections 3.3. and 4.2.2 respectively. The variation in the developed torque as the torque angle changes is more apparent as the stator current increases. This is consistent with the simulations carried out in previous chapters.

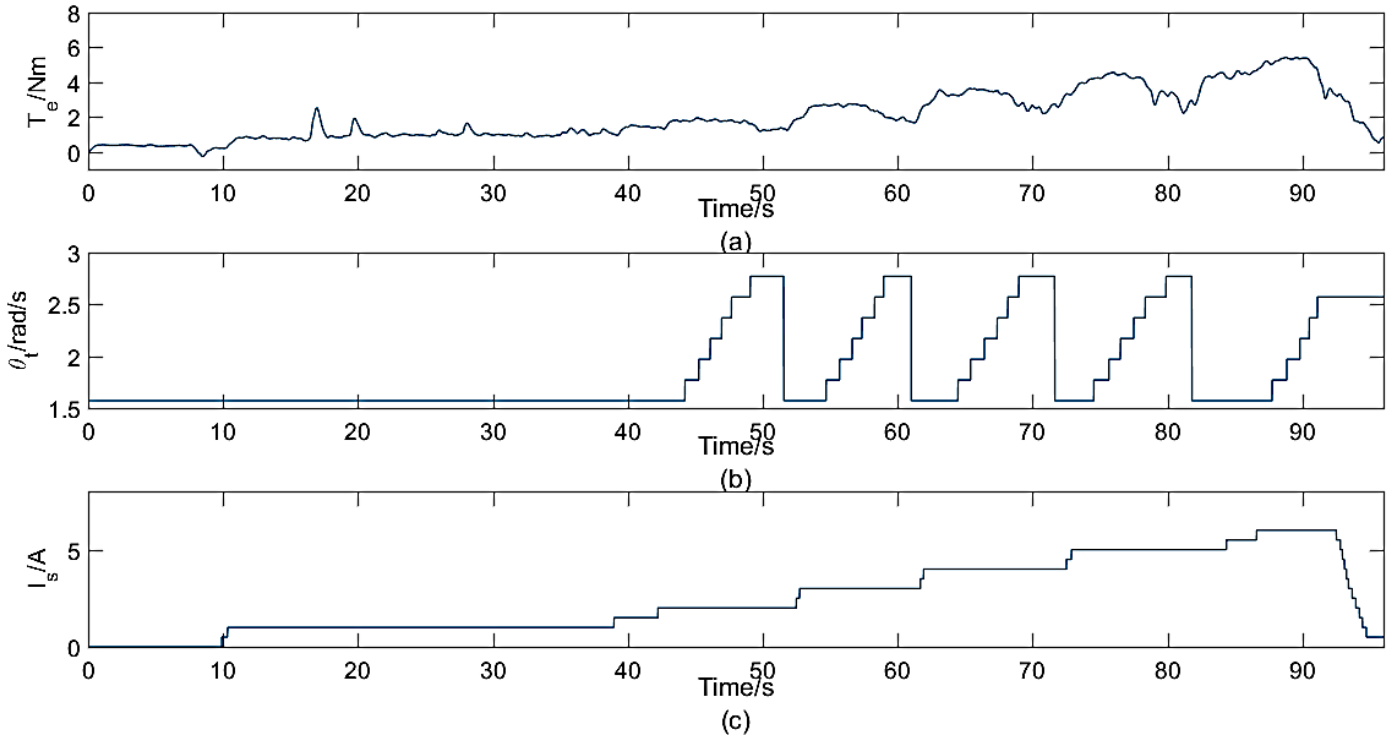

Figure 71:(a) Developed electromagnetic torque (b) torque angle (c) stator current magnitude

The MTPA torque θ_{to} angles from the experiment are shown in figure 72. They are presented with the simulated MTPA torque angle in figure 37 for comparison. The experimental and simulated values of θ_{to} take on a similar shape as the current varies, with the largest difference being 0.1 radians. The gradient of the developed torque near the maximum torque developed for each current magnitude is low. According to figure 71 (a), for a stator current magnitude of 5A, the maximum difference in the developed torque from the maximum developed torque, is 0.3Nm for a 0.6rad change from the MTPA torque angle. Thus, an error of 0.1rads in determining the MTPA torque angle would result in an insignificant difference around the maximum develop torque. The experiments also highlight the necessity for accurate models when simulating the IPM. In section 3.3 a model consisting of just the equivalent circuit of the generator was simulated and its MTPA torque angles were plotted in figure 28. Significant differences are observed between the MTPA torque angles in figure 28 and those found experimentally in figure 71. In section 4.2.1, a Simulink model is used, which uses the same equivalent circuit but also factors in harmonics and the effects of switching and sampling. This model produced MTPA torque angles that are much closer to the experimental values as shown in figure 72.

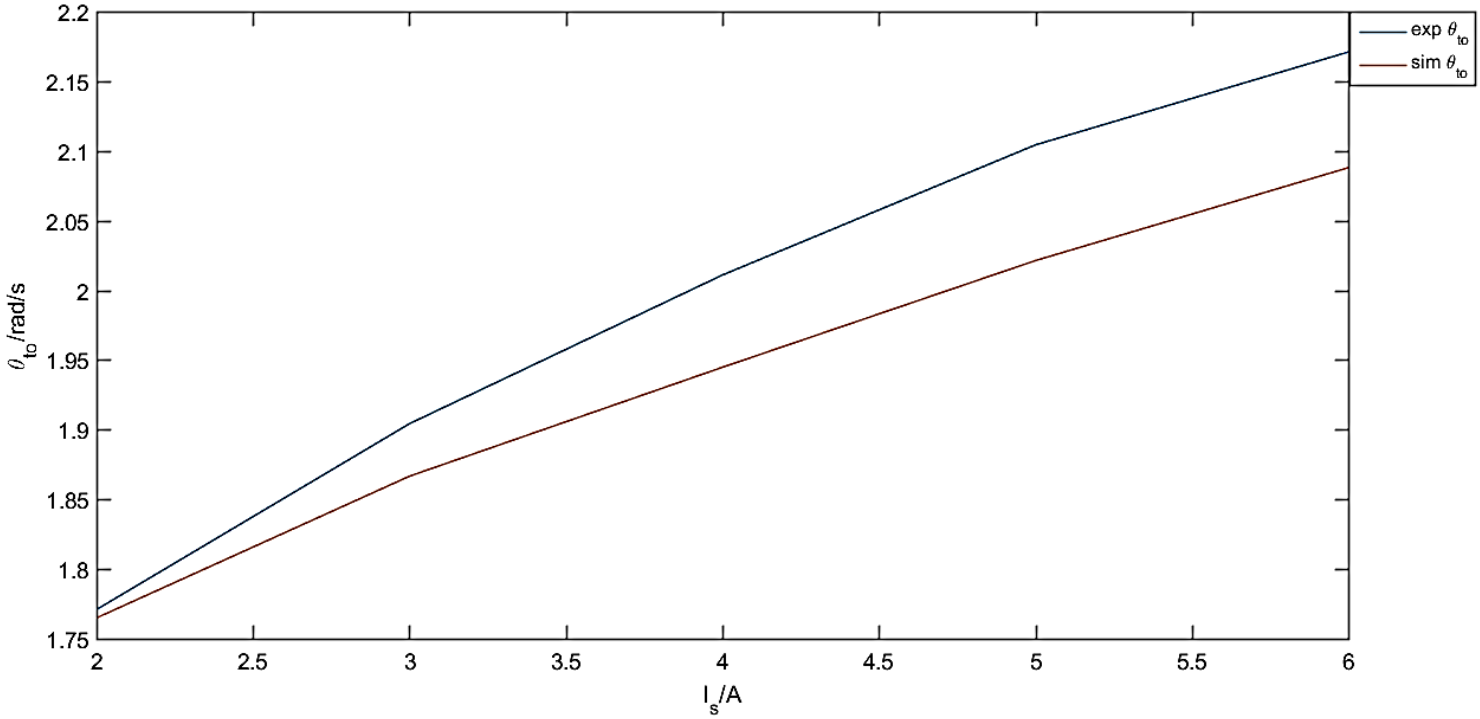

Figure 72: experimental and simulated values for the optimum torque angle

A factor that was not explored in previous chapters was the effect of speed on the MTPA torque angle. According to equation 3.42, the speed of the IPM has no bearing on determining MTPA torque angles. However, this does not consider effects from the turbine emulator on the IPM that result from them being mechanically coupled together. Figure 73 shows 3D graphs of the developed torque as a function of the current angle, current magnitude and speed of the IPM. The regions of maximum torque are highlighted in red. An average trend is observed where the smaller the stator current magnitude is, the smaller the MTPA torque angle becomes. This is corroborated by figure 72. However, the MTPA torque angles at lower speeds are less predictable and are located more randomly than at higher speeds. It is clear, that the prime mover's speed has a bearing on the MTPA torque angles and must be considered for practical implementation of MTPA control. Therefore, before MTPA control can be implemented from standstill to rated speed, an initial experiment must be conducted to find MTPA torque angles required for all speeds. A four- dimensional look-up table can be compiled from which operating points for the generator's speed, stator current magnitude and desired torque are searched to produce the required MTPA torque angle.

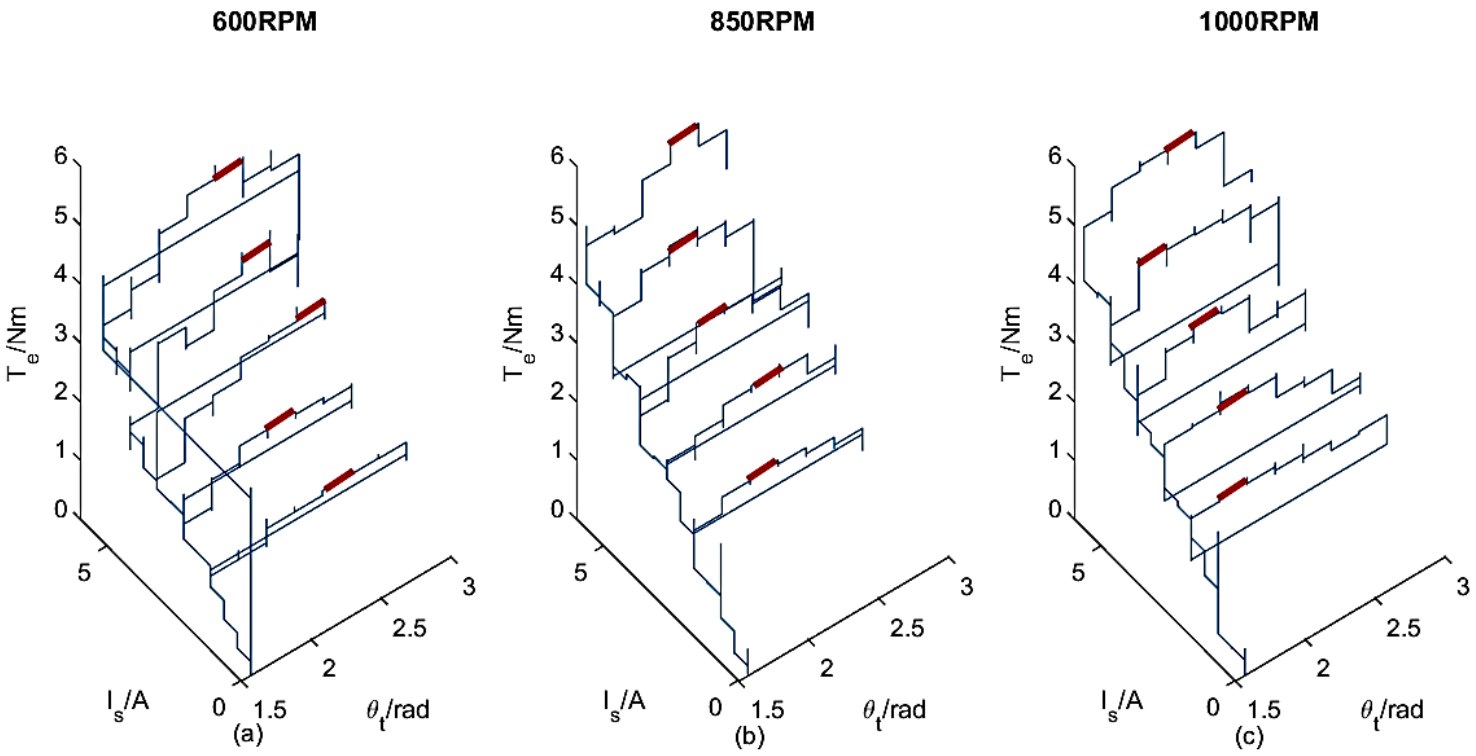

Figure 73: Developed EM torque as function of current magnitude and torque angle at (a) 600RPM (b) 850 RPM (c) 1000RPM

Consider the scenario where the generator-side converter is used to regulate the DC-link voltage at no load. The developed torque required to regulate the DC-link voltage is given in figure 74. The DC-link is regulated at 400V, stepped down to 300V and back up to 400V. A DC-link voltage of 300V gives a visibly lower torque THD than at 400V. Any distortion in the torque will be reflected in the stator currents and DC-link voltage. It can also be seen that the average torque is lower at 300V than at 400V, which is a result of lower losses in the DC-link capacitor. The DC-link capacitor has a parasitic series equivalent resistance associated with it called ESR. The higher the current ripple of the capacitor the higher the losses in the capacitor. High losses in the capacitor will result in significant heating and possible failure of the component. For these reasons, DC-link voltages are regulated to as low a voltage as possible, without saturating the converter.

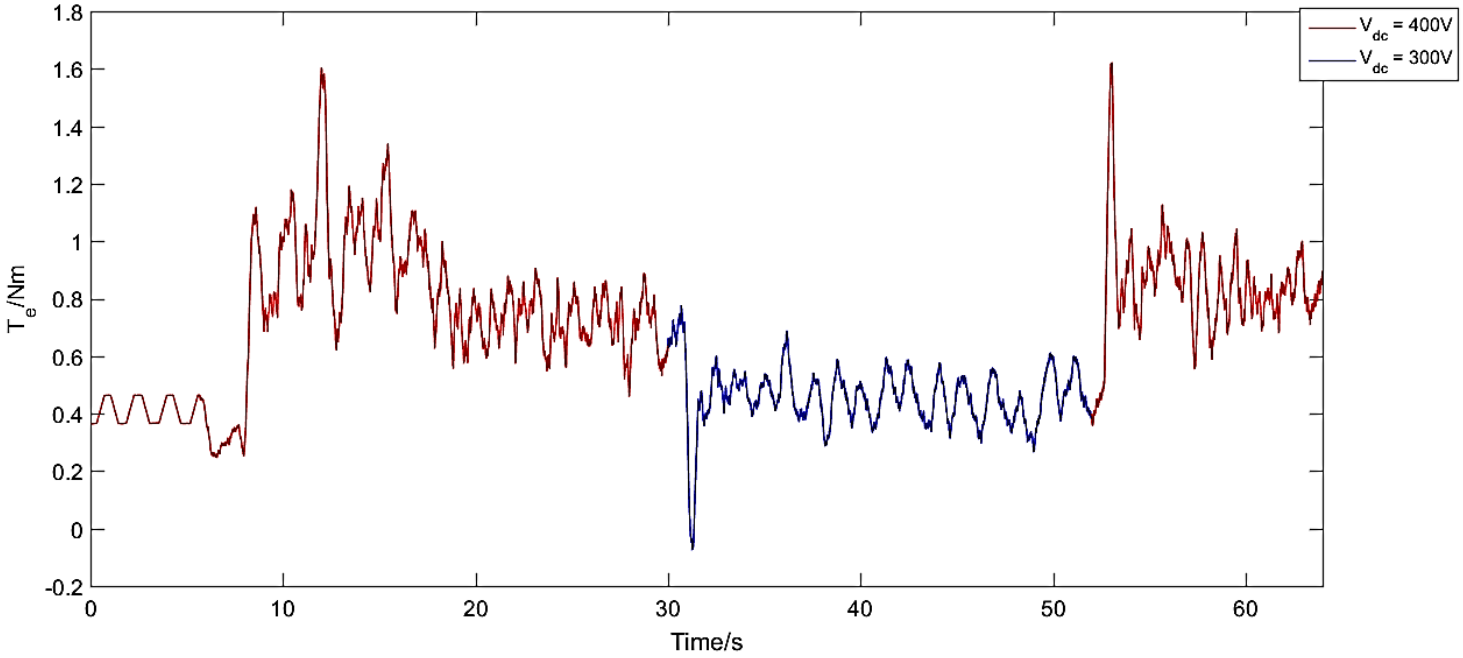

. Figure 74: Torque ripple

It was mentioned previously that a malfunctioning encoder resulted in the limiting of the IPM's speed to 1100RPM. Consequently, a lower induced EMF than expected is developed by the generator. This means lower stator terminal voltages from the converter are required to control the stator current. During the experiments, it is found that high DC-link voltages result in significant torque ripple. This is consistent with the findings in the previous discussion. It was decided that the DC-link voltage would be lowered to increase the modulation index. Consequently, the grid voltage as well had to be lowered to avoid converter saturation on the load-side converter.

The voltage utilisation is of greater importance than in previous chapters because of the DC-link voltage ripple. To avoid converter saturation, it is required that the line-to-line stator terminal voltage be lower than the DC-link ripple. According to figure 76, the stator terminal voltage ripple which is a consequence of the DC-link ripple increases as the stator current increases. The DC-link voltage can be increased so that the stator voltage remains below the DC-link voltage ripple. However, this would mean using a lower modulation index, which increases the THD of the stator currents, developed torque and load currents. A larger DC-link capacitor could be used to mitigate DC-link voltage ripple, but this would come at a higher purchasing cost and would result slower DC-link voltage dynamics. Field weakening provides the best solution in that it allows lower converter voltages to drive high stator current by

employing a torque angle greater than 90 degrees. It must be mentioned that significant weakening of the flux-linkage in the generator could lead to permanent demagnetization of the permanent magnets in the IPM's rotor. In figure 75, higher torque angles result in lower stator terminal voltage magnitudes required to regulate stator current.

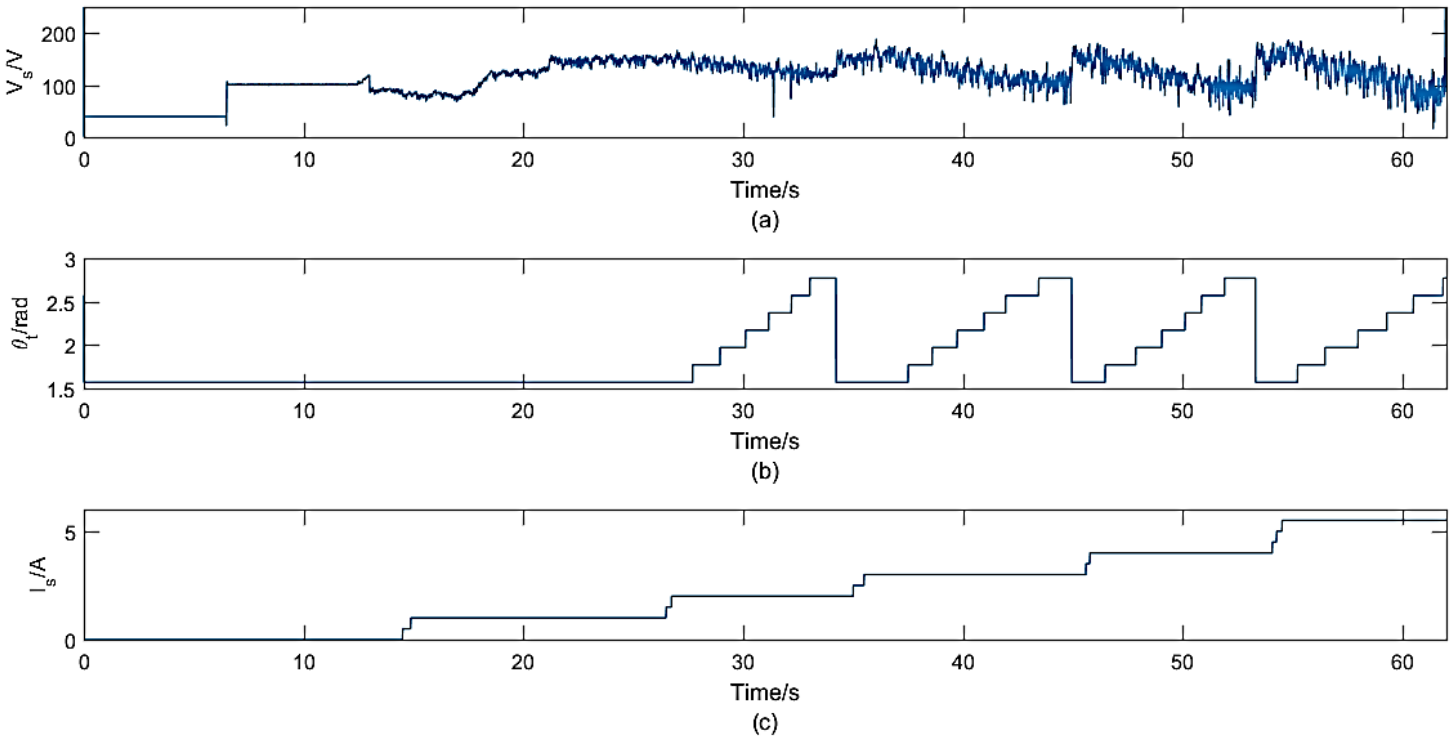

Figure 75: (a) Stator terminal voltage (b) Torque angle (c) Stator current magnitude

In chapter 4 it was determined that the most suitable control strategy was UPF control. This was due to its high torque production, low DC-ink utilisation and high power factor. A power factor of unity is achieved when the apparent power VA is equal to the active power P.

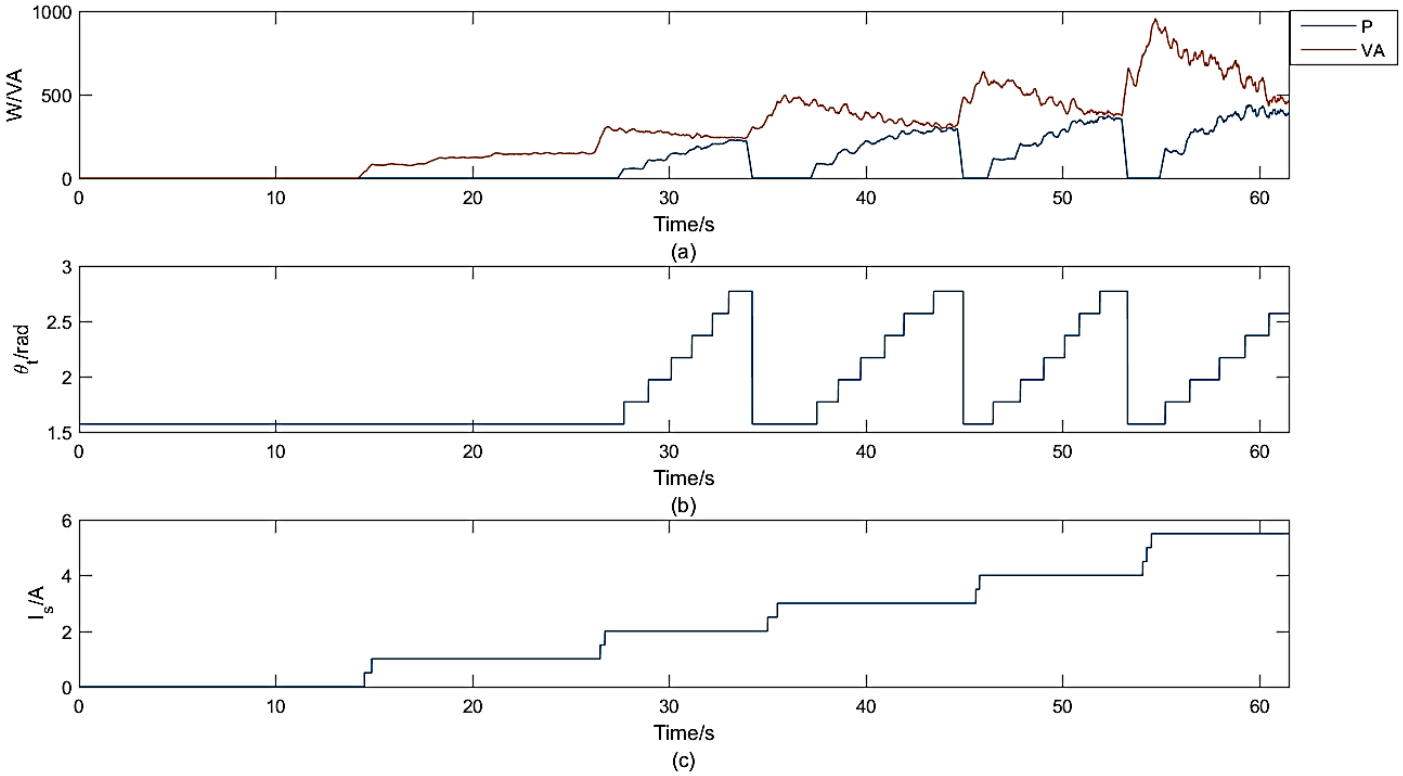

Figure 76: (a) Active and reactive power production (b) torque angle variation (c) Subsequent power factor variation

Figure 41 in section 4.2.2 gives a range of UPF torque angles for different stator currents. It was observed that the UPF torque angle displayed little variation from each other despite the different stator current magnitudes, varying from 2.1rad to 2.9rad. Additionally, the IPM displayed high power factors for the range of torque angles near the UPF torque angles. This is supported by figure 76 (a) where unity power factor is approached asymptotically. The result is a high power factor for torque angles near the UPF torque angle. Figure 76 (a) and (b) also show that the UPF torque angle falls within the range 2.1rad and 2.9rad. However, the UPF torque angles from the experiment vary less than those from the simulations. It is safe to say that a torque angle of 2.71rad will approximate unity power factor for all stator current magnitudes. Using one torque angle for the entire operation of the IPM will unburden the PXI processor as a look-up table is not required

MTPA control minimises stator conduction losses and increases mechanical power production, but this does not translate into the optimal operation of the generator. Figure 76 (a) shows the input mechanical power P_{mech} from the turbine emulator and the electrical power P_{gen} produced from the generator, for different torque angles and current magnitudes. The torque angle of maximum efficiency (ME) occurs where the difference between P_{mech} and

P_{gen}, is at a minimum. Figure 77 shows that ME torque angles occurs at bigger angles than the MTPA torque angles. ME torque angles also result in the highest production of electric power, even though they produce a lower developed torque than MTPA torque angles. Figure 77 (b) and (c) show that the worst efficiency rate occurs at a torque angle of 90 degrees. The efficiency gradually increases as the torque angle increases.

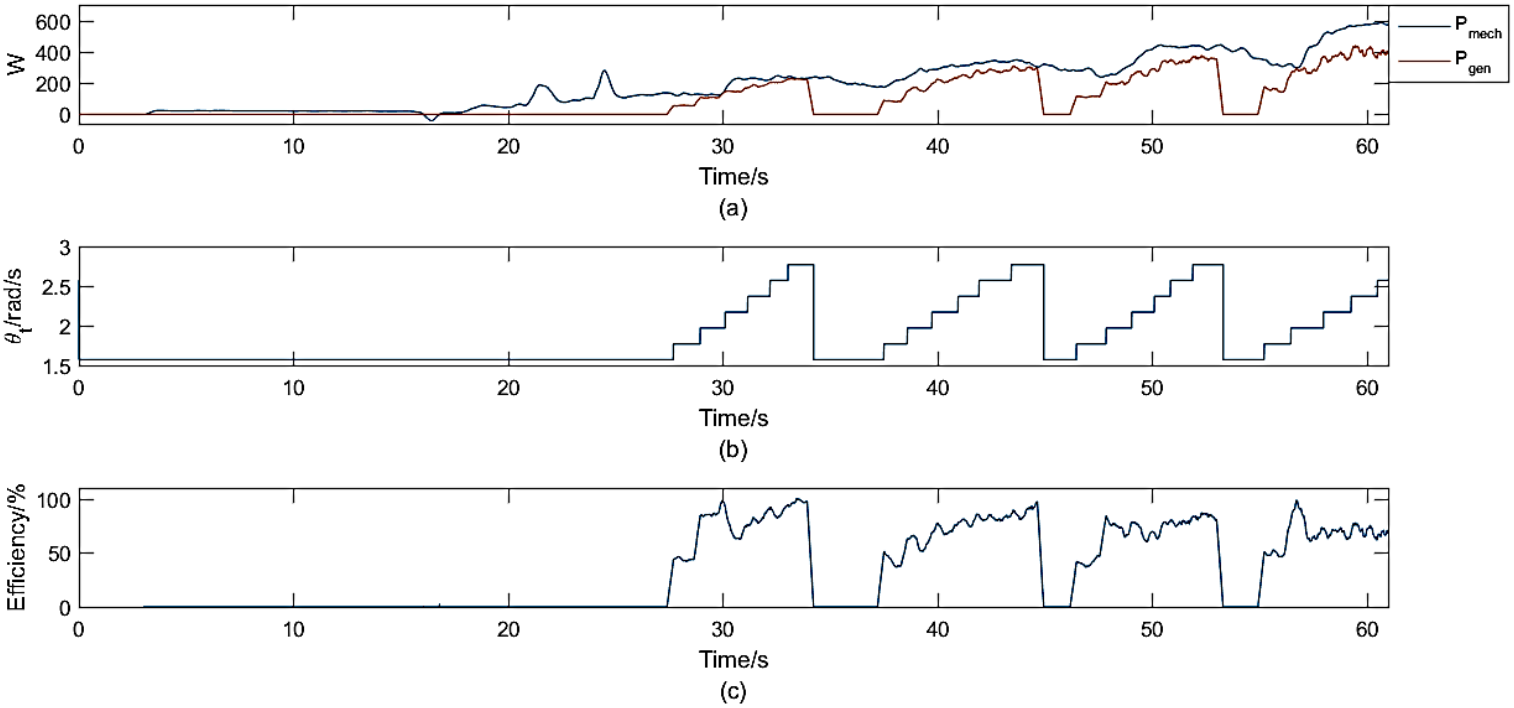

Figure 77: (a) Active and reactive power production (b) torque angle variation (c) generator efficiency

Like the power factor in figure 76, the efficiency asymptotically improves as maximum efficiency is approached. Earlier in the discussion it was concluded that torque angles near the MTPA torque angle would result in a near optimal torque production. In figure 77, the ME torque angle occurs immediately after the MTPA torque angle, and results in a near optimal developed torque. It was also concluded that the UPF torque angle in figure 76 was 2.71rad, while the ME torque angle in figure 77 is determined to be 2.83rad. The proximity of the ME toque angle to the UPF torque angle guarantees that the ME torque angle will result in a power factor that is close to unity. With a torque angle of 2.83rad, most of the stator current is contributed by the d-axis component. This results in significant field weakening and thus a low DC-link utilisation. Therefore, ME results in the optimal operation of the IPM when considering generator efficiency, developed torque, electric power production, power factor and DC-link voltage utilisation.

Figure 78 illustrates the performance of ME control strategy under different generator loads. The ME control strategy is evaluated on its performance regarding generator efficiency, power factor and ratio of developed torque to the torque that would result from MTPA control. Due to the proximity of the ME torque angle to the MTPA and UPF torque angles, it results in a near optimal power factor and developed torque in addition to maximising the efficiency of the IPM.

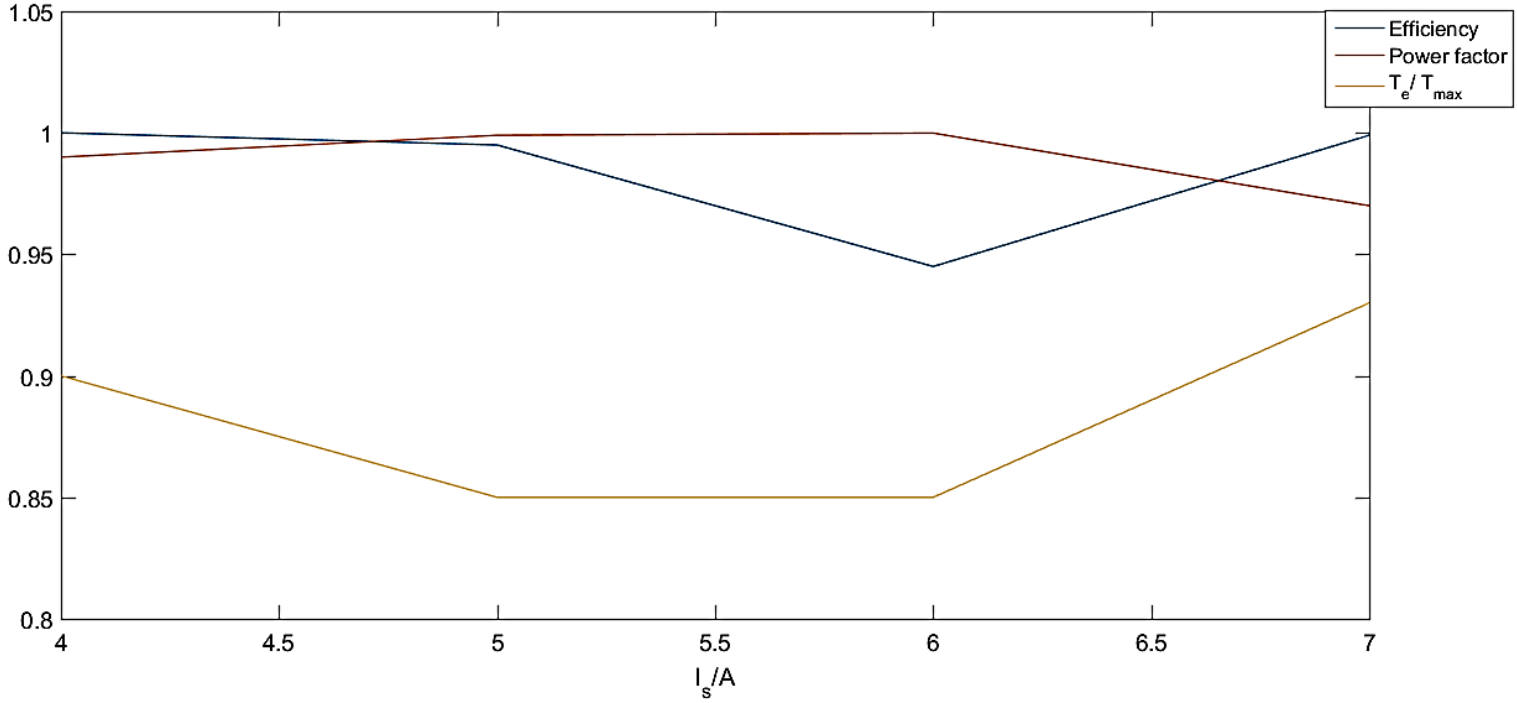

Figure 78: ME performance in terms of generator efficiency, power factor and developed torque

With ME control, efficiencies greater than 95% are achieved and unity power factor is attained. The ME control strategy can only be investigated through experimentation because the core and windage losses are not modelled in the simulations. The modelling of these losses can be tedious as environmental factors such as temperature can have an effect.

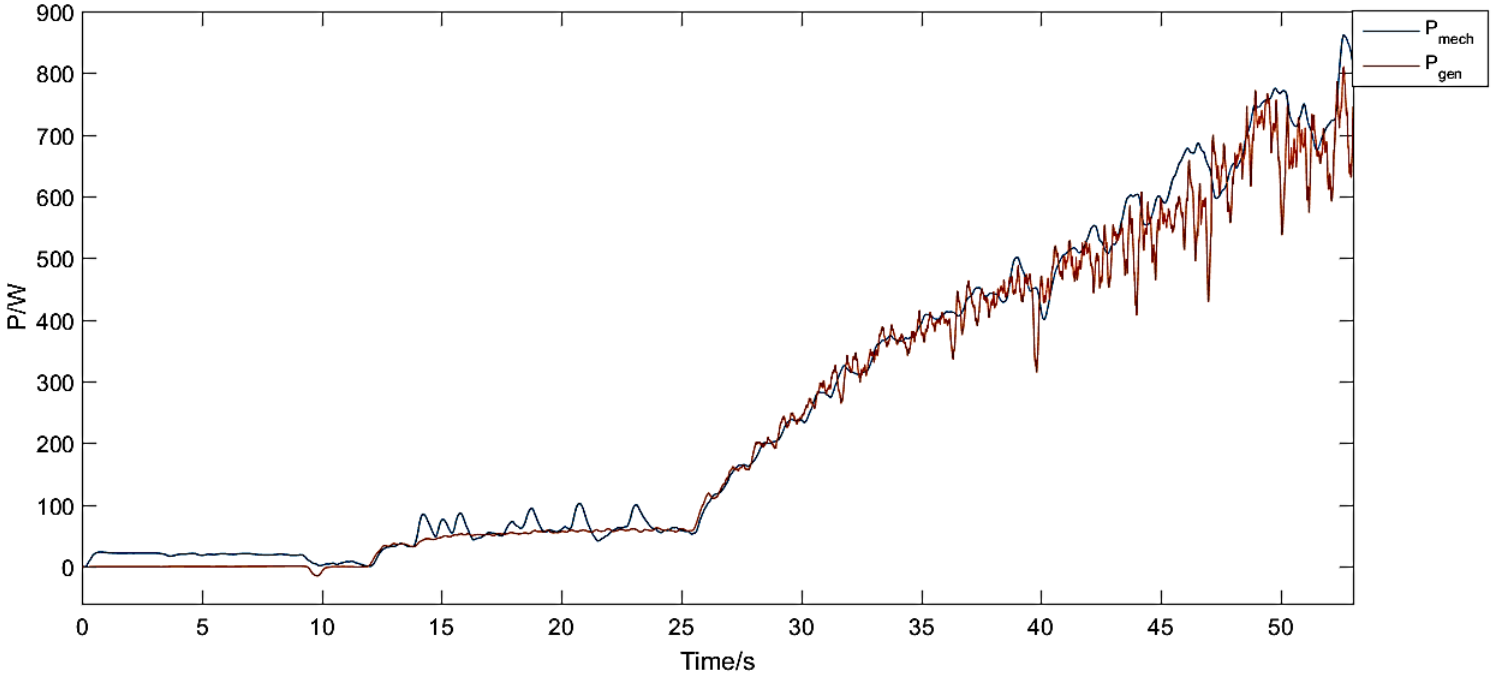

Figure 79: Performance of the ME control strategy

6.3 Load-side control

This section focuses on the control of load-side system. The control of load currents in both grid-tied and isolated operation is investigated. After which, control of load-side currents under unbalanced grid voltage conditions is carried out.

6.3.1 Grid current control

In grid-tied mode, the load-side converter delivers power to the utility grid. Successful control of gird currents is illustrated in figure 80. The ability to control both d-axis and q-axis currents means the load-side converter can determine the power factor of the power delivered to the grid. The slower reaction time as compared to the simulations can be attributed to the sampling rate of 4kHz, which is significantly slower than the rate used in Simulink. A faster sampling rate was required in Simulink to obtain legible results. The PI gains of the currents could be increased to speed up the response time, but this would be at the cost of a higher DC-link voltage utilisation. The LCL-filter was found to have a gain margin of 15dB in section 3.2.3, therefore larger control gains could also result in system instability. If the outer-loop control is delayed similarly, then no control issues should result. The current shows no signs of resonance which suggests the damping of the LCL-filter is successful.

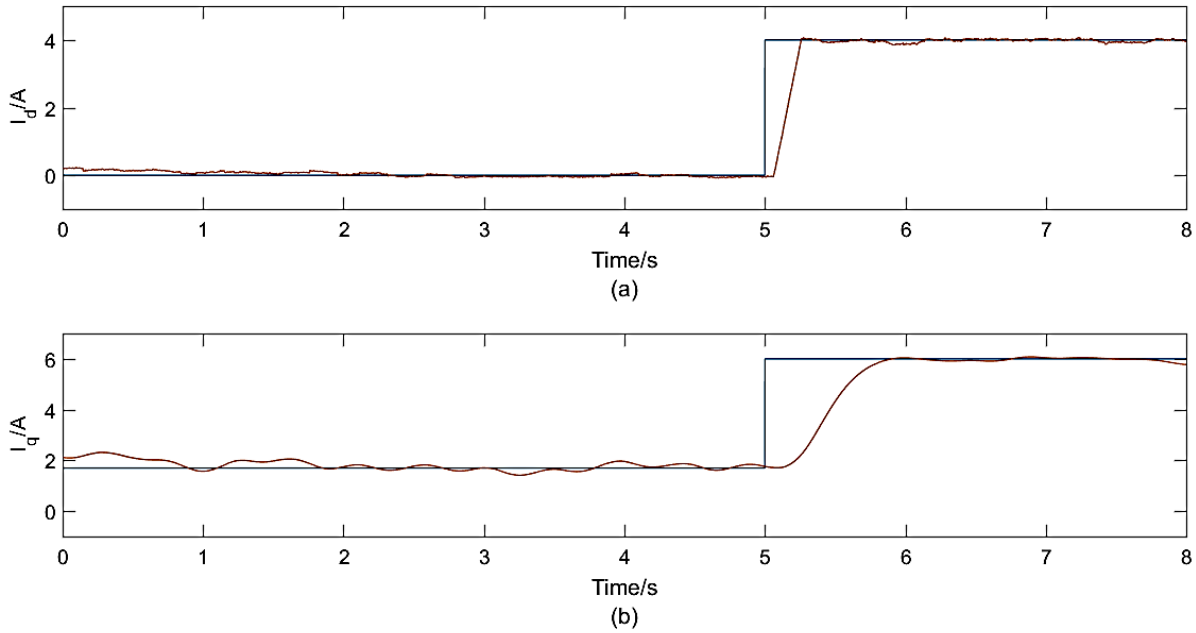

Figure 80: successful control of (a) d-axis current (b) q-axis current in grid-tied mode

6.3.2 load-side current control in isolated mode of operation

In this section the load-side converter feeds power to an isolated load. Figure 81 shows that the dynamic response of the d-axis and q-axis load currents is slightly slower than the grid current in figure 80. This is consistent with the simulations in section 4.3.2. A delay due to the slow sampling rate of 4kHz in the current response time is expected as in previous sections. The consequence of a slow inner-loop current response is that the outer-loop control must be at least 10 times slower. The outer-loop control could be specified as the regulation of the DC-link voltage. The DC-link voltage is slow varying compared to the current; for this reason, it is decided that a slower sampling rate of 3kHz is adequate. This means that the sampling of DC-link voltage could be executed by the CPU, which would free-up space on the FPGA. The slower sampling frequency delays the DC-link voltage response further than the current response is delayed. This ensures that the outer-loop DC-link voltage control is significantly slower than the inner-loop current control.

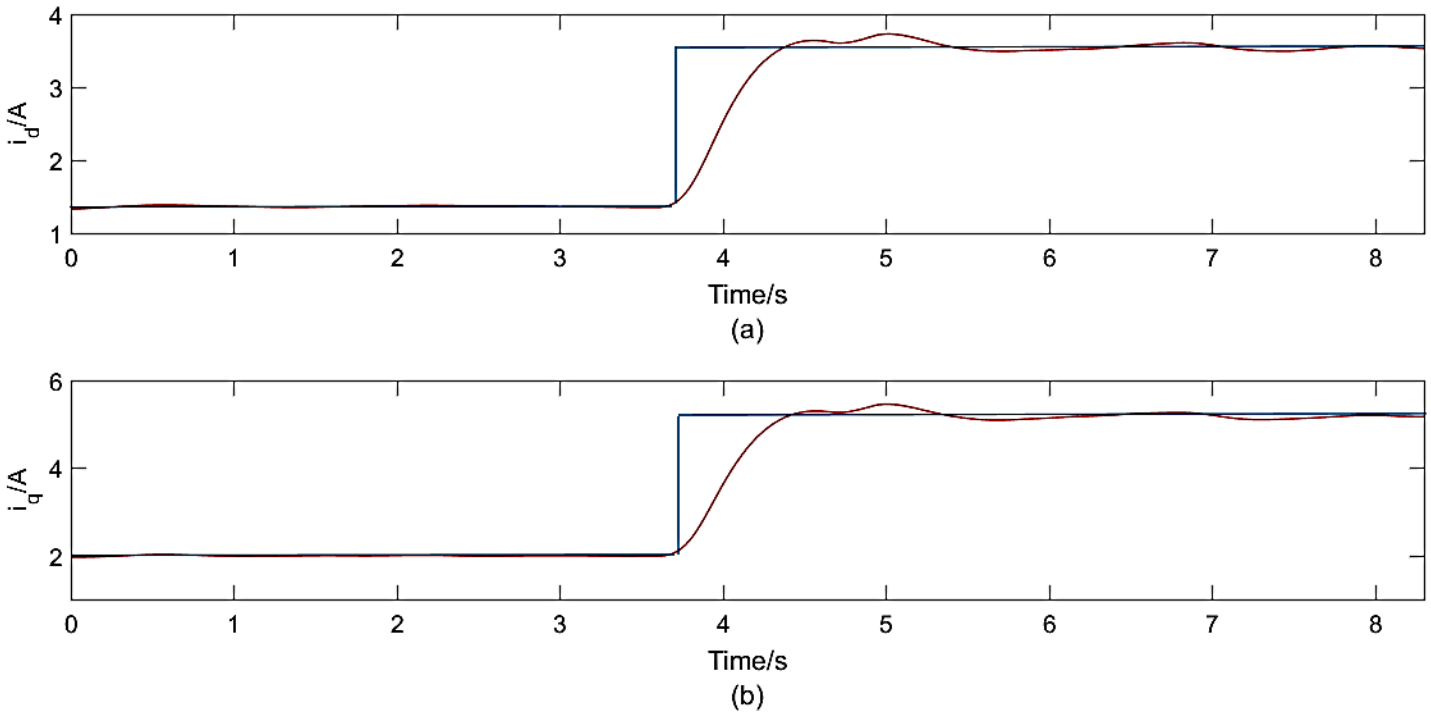

Figure 81: successful control of (a) d-axis current (b) q-axis current in isolated mode

6.3.3 Load-side current control during load-voltage unbalance

An algorithm that extracts positive and negative sequence quantities from an unbalanced grid voltage was developed in section 3.1.1. It was implemented in simulation in section 4.3.3 and will be implemented experimentally in this section. For the experimental implementation of the algorithm, unbalanced grid voltage magnitudes of 200V, 180V and 170V are used. The unbalanced voltages are achieved with a three-phase variac, with independent settings for each phase. The load-side currents become unbalanced because of the unbalanced load voltages. The result is a 100Hz oscillation above the d-axis and q-axis load-side currents. This is shown in figure 82 and is most apparent in the d-axis current.

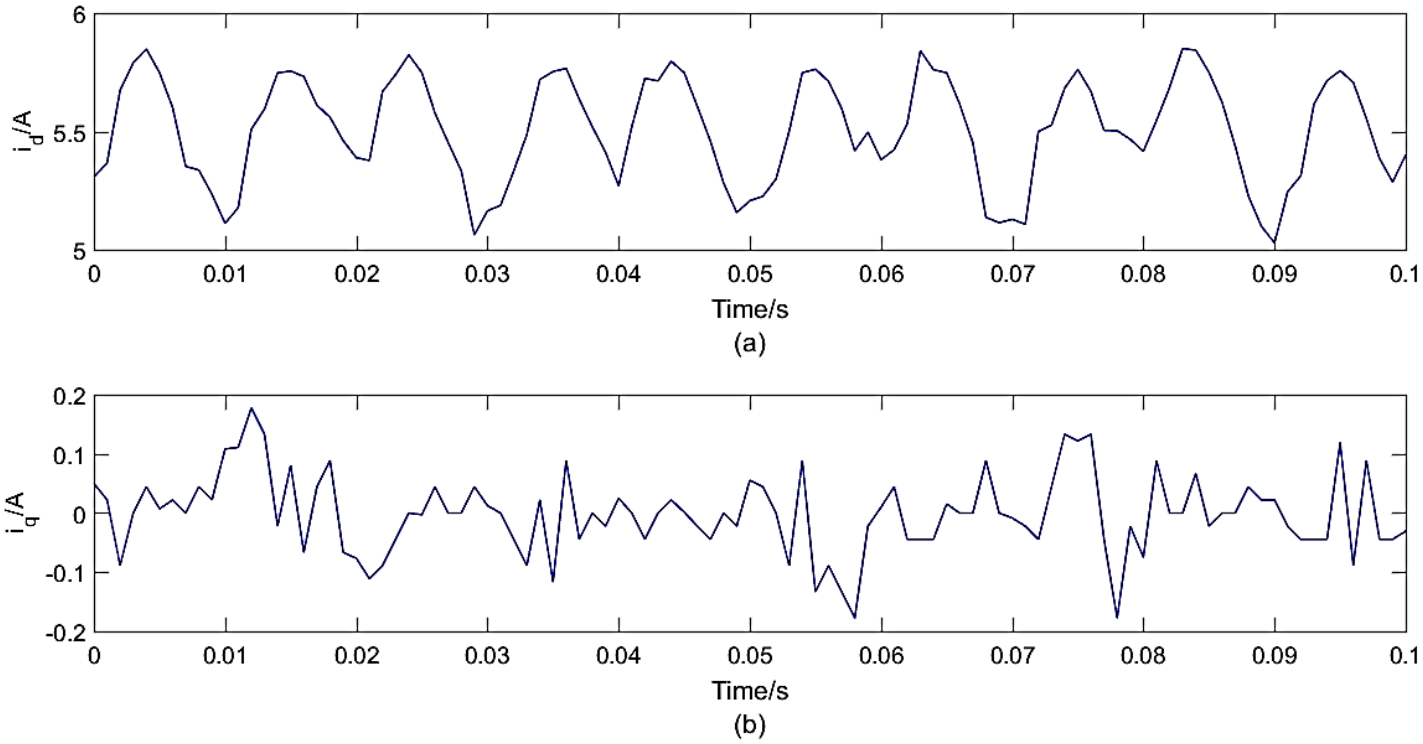

Figure 82: (a) d-axis current (b) q-axis current during unbalance

The oscillations are undesirable because they can compromise the controllability of the system and inject harmonics into a load or grid. The RLS algorithm from section 4.3.3 is implemented and the results are given in figure 83. The Unbalanced control is activated at 10 seconds and greatly reduces the oscillations in the currents. The RLS algorithm is slow to converge, as a result the control action is slow to implement change as expected from section 4.3.3.

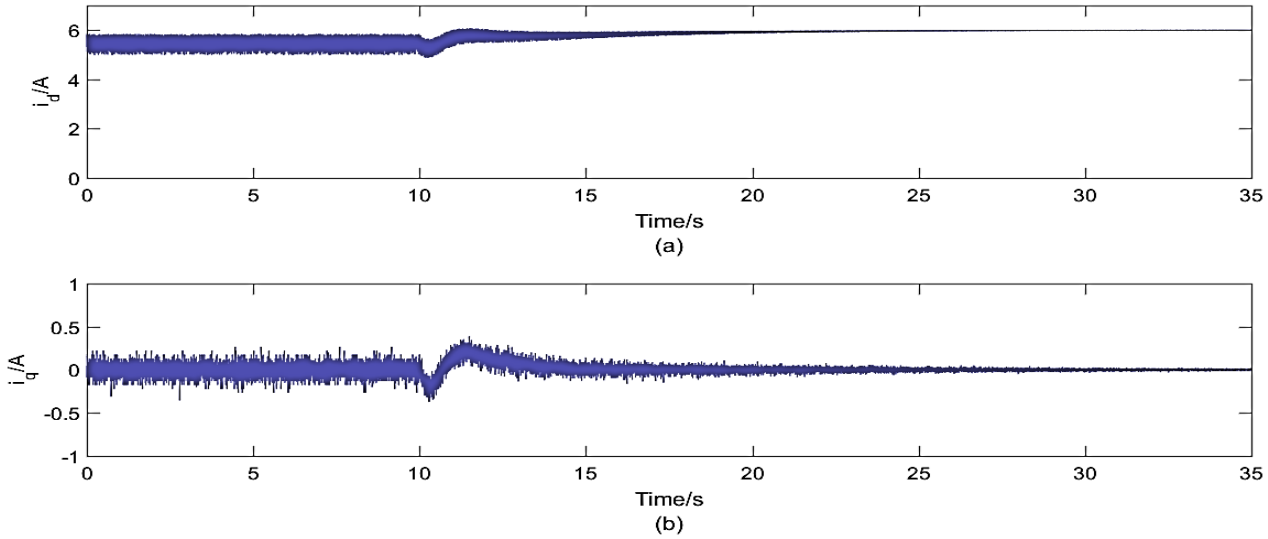

Figure 83: unbalanced current control (a) d-axis (b) q-axis

It must be noted that performance of the RLS algorithm is hindered by the slow processing rate of the CPU. Due to lack of space on the FPGA, the algorithm could not be placed on the FPGA for a faster performance. However, the concept was proven to be effective in mitigating the effects of load voltage unbalance.

6.4 Outer-loop control

This section discusses the outer-loop control possibilities for the generator-side and the load-side systems. It is argued that it is advantageous to have generator-side converter regulate the DC-link voltage, while the load-side converter regulates the load-side voltage during isolated mode of operation and reactive power compensation.

6.4.1 DC-link voltage regulation by the load-side converter

Most applications in literature use the load-side converter to regulate DC-link voltage. The low filter inductance of the system allows the load-side system to respond quickly to deviations in the DC-link voltage. Figure 84 illustrates the operation of the load-side system in grid-tied mode. At 0 seconds there is no input power from the generator-side system although the gas-turbine is driving the generator. The DC-link voltage is pre-charged to 230V at 3 seconds through a passive rectifier connected to the PMSG. The passive rectifier is then disconnected from the generator by a contactor. Synchronisation occurs after 5 seconds and the grid is connected to the load-side system shortly thereafter. The DC-link voltage is increased to 400V by drawing power from the grid at 7 seconds and is held at this value throughout the rest of the experiment. At 17.5 seconds the generator begins to produce electrical power and thus the load-side delivers power to the grid to prevent the DC-link voltage from rising. Power is delivered to the grid at unity power factor, therefore the q-axis current is kept at zero. The generator input power is varied and thus the d-axis current varies accordingly to regulate the DC-link voltage at 400V.

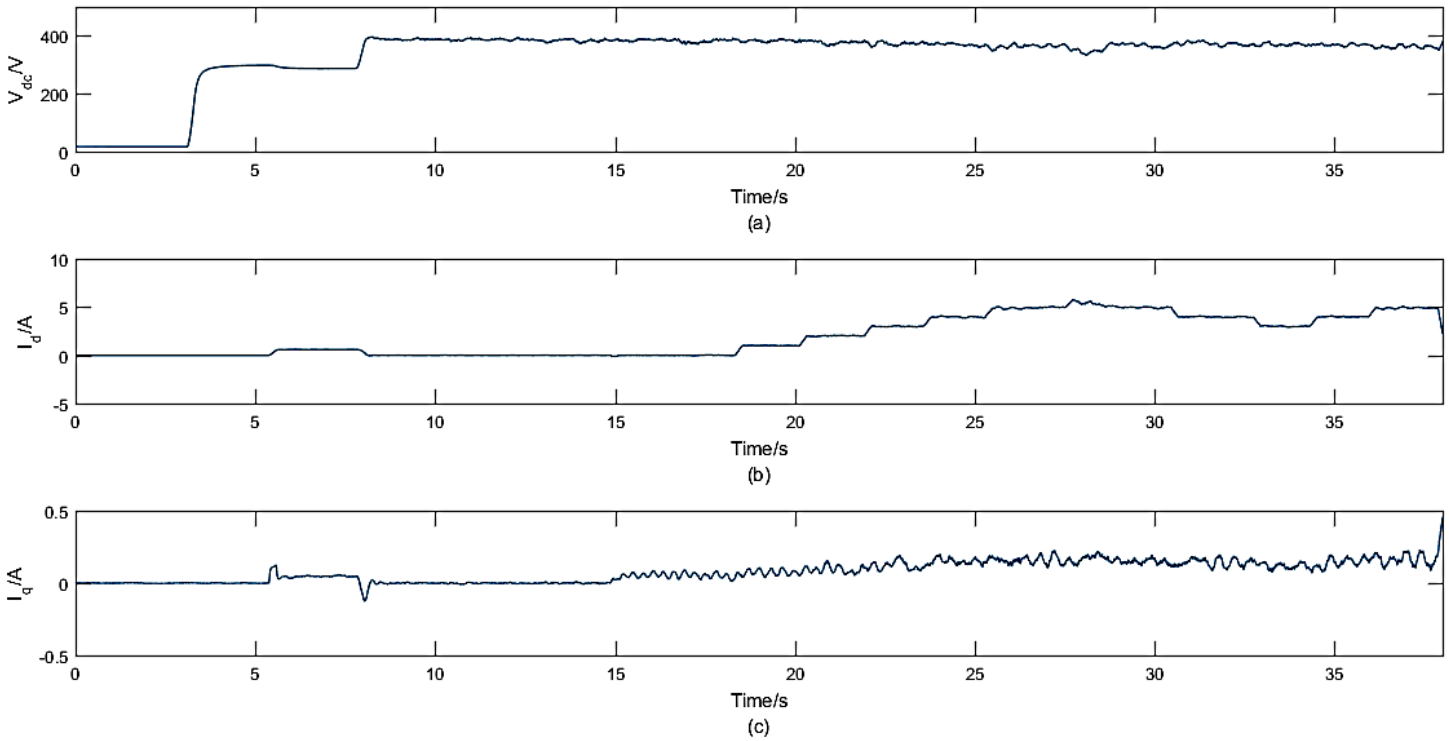

Figure 84: (a) DC-link voltage regulation (b) d-axis current (c) q-axis current

6.4.2 DC-link voltage regulation by the generator-side converter

The DC-link regulation can also be achieved by the generator-side converter. The electromagnetic torque of the IPM is used to vary the input power into the DC-link. An increase in the production of electrical power results in an increase in the DC-link voltage, and a decrease in electrical power production result in a decrease in the DC-link voltage. The generator current response is slower than the load-side current response (figures 70, 80 and 81) because of the larger generator inductances. Therefore, fast dynamics in the DC-link voltage must be ignored by the control system as this could cause instability of the generator-side system. A digital Butterworth filter is used by the control system to limit the bandwidth of the DC-link voltage as seen by the control system. A cut-off frequency of 150Hz is used.

Figure 85 illustrates the successful control of the DC-link voltage by the generator-side converter. The DC-link voltage is stepped from 440V to 400V. At 28 seconds the torque production decreases to allow the DC-link voltage to transition to the lower voltage; a subsequent increase in torque stabilises the DC-link voltage at 400V. The load-side system is not feeding a load, thus the torque observed during steady state is lost as heat in the DC-link. The DC-link voltage is high compared to the induced EMF from the generator therefore a

significant DC-link voltage ripple exists due to the THD in the torque, as explained in section 6.2.3 and figure 74. The generator current references are given in accordance with the ME control strategy.

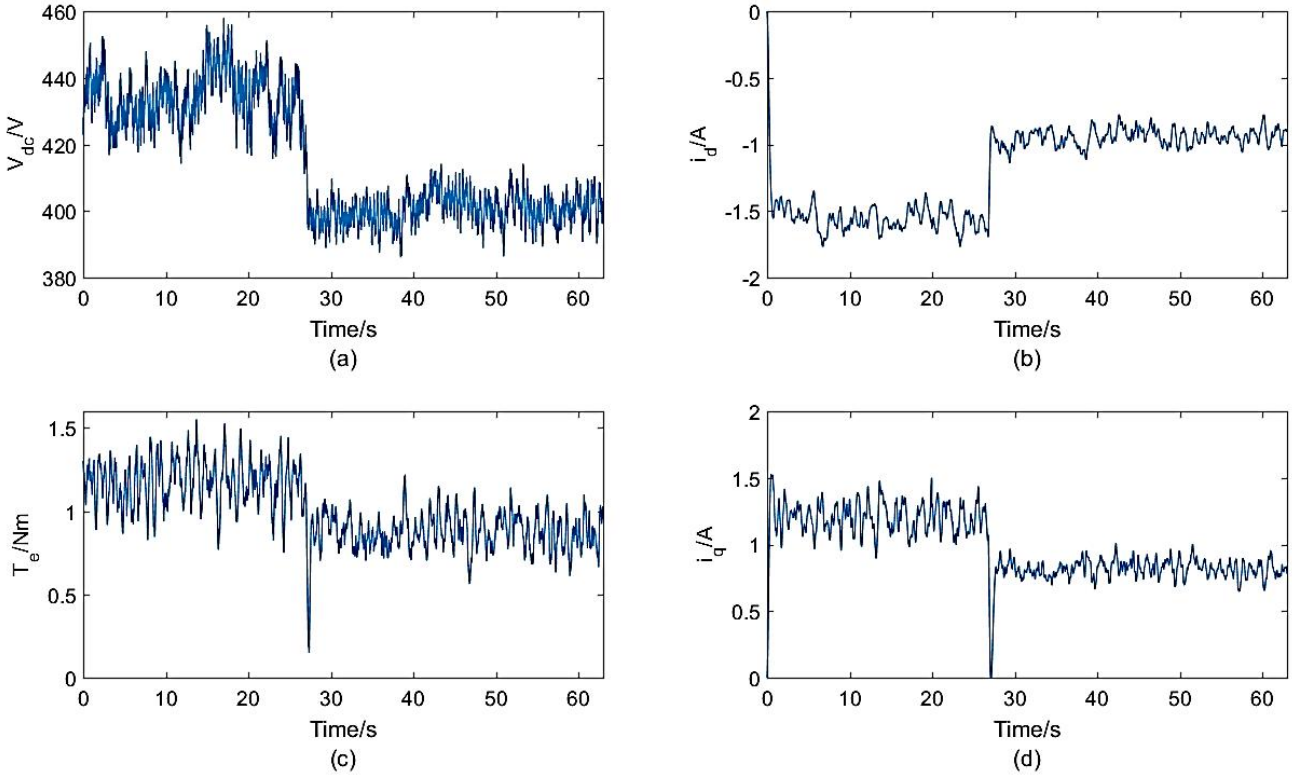

Figure 85: (a) DC-link voltage (b) d-axis current (c) electromagnetic torque (d) q-axis current

6.4.3 Isolated mode of operation

In isolated mode of operation, the load's power demand must be satisfied by the gas turbine generator system. The load demand can change at any moment; therefore, the control system must regulate power supplied to the load as well as the voltage across the load, all while ensuring efficient operation of the generator. The speed of the free-turbine is regulated by varying the gas turbine generator's mechanical torque production. If the speed of the free-turbine decreases below the reference speed, the mechanical input torque will increase; the opposite will happen if the speed of the free-turbine increases above reference speed. Loading of the turbine can be achieved by controlling the electromagnetic torque of the IPM. Through the control of the IPM, the mechanical input torque can momentarily be controlled without interfering with the operation of gas turbine emulator.

An increase in the load's power demand will result in a drop in the voltage across the load. The DC-link voltage will also drop as the load attempts to draw additional power from it. An

increase in the DC-link voltage indicates that more power is being generated than is being consumed by the load. A decrease in the DC-link voltage indicates less power is being generated than is demanded by the load. Therefore, the DC-link voltage can act as an indicator of power balance between the generator-side and load-side systems. When the generator-side converter regulates the DC-link, the IPM is used to control the loading of the gas turbine emulator. The gas turbine responds by varying the mechanical power it produces. The loading of the gas turbine by the IPM is implemented in a way that will balance the DC-link. The main advantage is that an additional line of communication is not required between the load-side and the turbine emulator to vary the mechanical torque from the turbine. As a result, the gas turbine and the IPM operate independently. The outer-loop control of the load-side can be used to regulate the voltage across the load and for reactive power compensation when necessary.

In figure 86 a variable resistive load is interfaced with the load-side converter. The DC-link is voltage is increased from 300V and 400V to demonstrate its controllability from the generator-side converter. The voltage across the load V_l is increased from 150V to 200V at 9 seconds to demonstrate its controllability by the load-side. The load's power demand changes from 200W to 600W at 25 seconds, this causes the DC-link voltage and the load voltage to decrease slightly. The generator-side system increases the electromagnetic torque of the IPM, slowing down the free-turbine. The turbine emulator responds by increasing its mechanical power input. The DC-link voltage is then restored back to its reference value. After which, the load voltage is also restored back to its reference value.

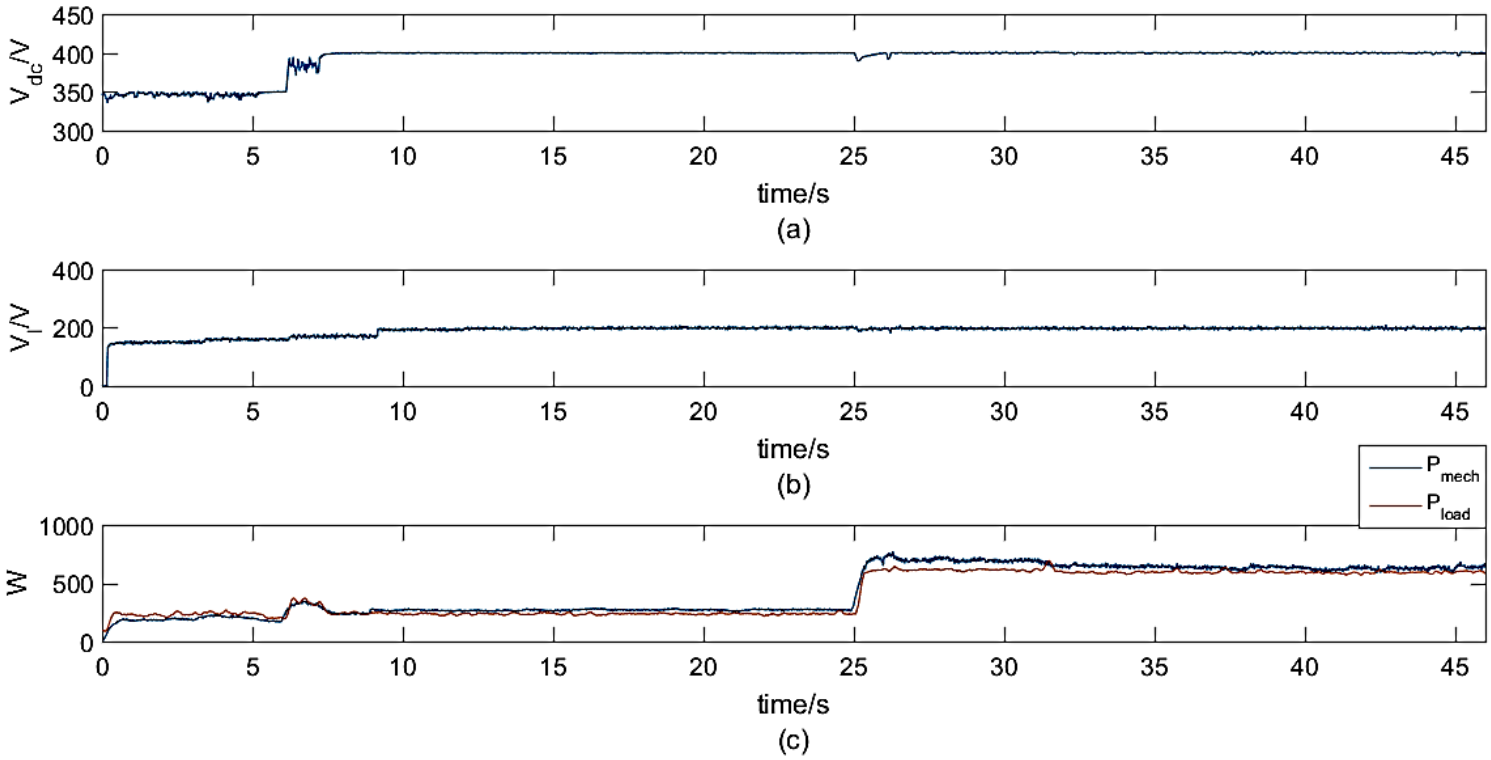

Figure 86: (a) DC-link voltage (b) Load voltage (c) Mechanical input and load demand power

The gas turbine generator system can form part of a microgrid, in which the voltage level needs to be maintained at the nominal value. In situation where the gas turbine cannot meet the load demand, reactive power compensation is used to raise the load voltage, while starving the load of active power. The d-axis and q-axis currents determine the active and reactive power respectively. In figure 87, the resistive load is varied from 200W to 600W while the power factor is varied from 0 to 1. At 17 seconds the power factor is decreased from 1 to 0 gradually until 40 seconds. This results in a gradual increase in the load voltage. At 40 seconds the power factor is suddenly increased to 1 and the load is increased to 600W thereafter. The load voltage decreases but increases again after the power factor is lowered again. In all cases, an increase in the reactive power results in an increase in the load voltage.

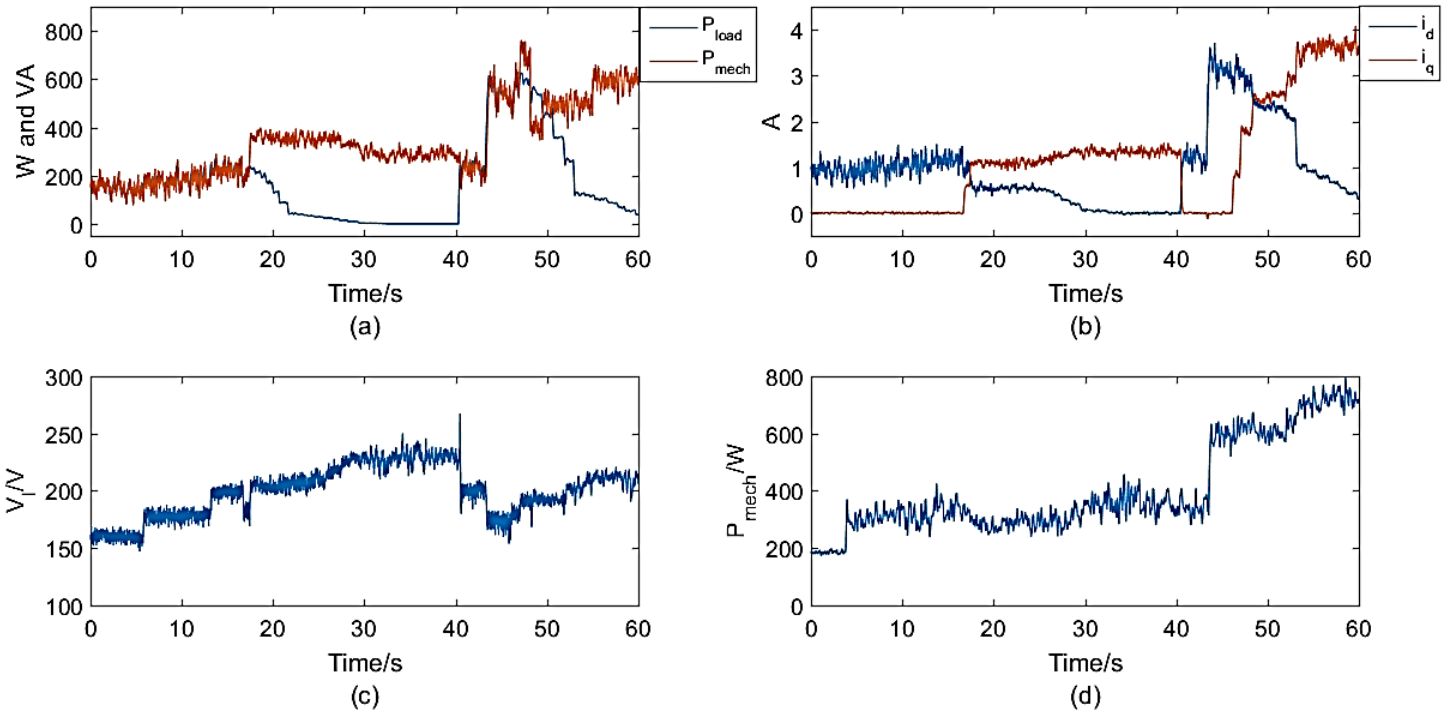

Figure 87: (a) Apparent and active power (b) d-axis and q-axis current (c) load voltage (d) Mechanical power input

As discussed in section 4.4.1 and illustrated in figure 55, it becomes increasingly difficult to regulate the DC-link voltage from the load-side with a low power factor due to the high current demand. It is also impossible to regulate both the load voltage and DC-link from the load-side simultaneously. Therefore, it is advantageous to regulate the DC-link from the generator-side and regulate the load voltage from the load-side during isolated operation and when applying reactive power compensation.

It was stated that the windage, mechanical and core loses are subtracted from the torque and mechanical power measurements. Therefore, the only expected losses in the system are due to the switching losses, the losses in the DC-link capacitor and the losses in the LCL-filter. Figure 88 shows the mechanical input power and the power consumed by the load. Power is delivered to the load at unity power factor. High efficiency is achieved at all loads, which results from the successful implementation of the ME control strategy.

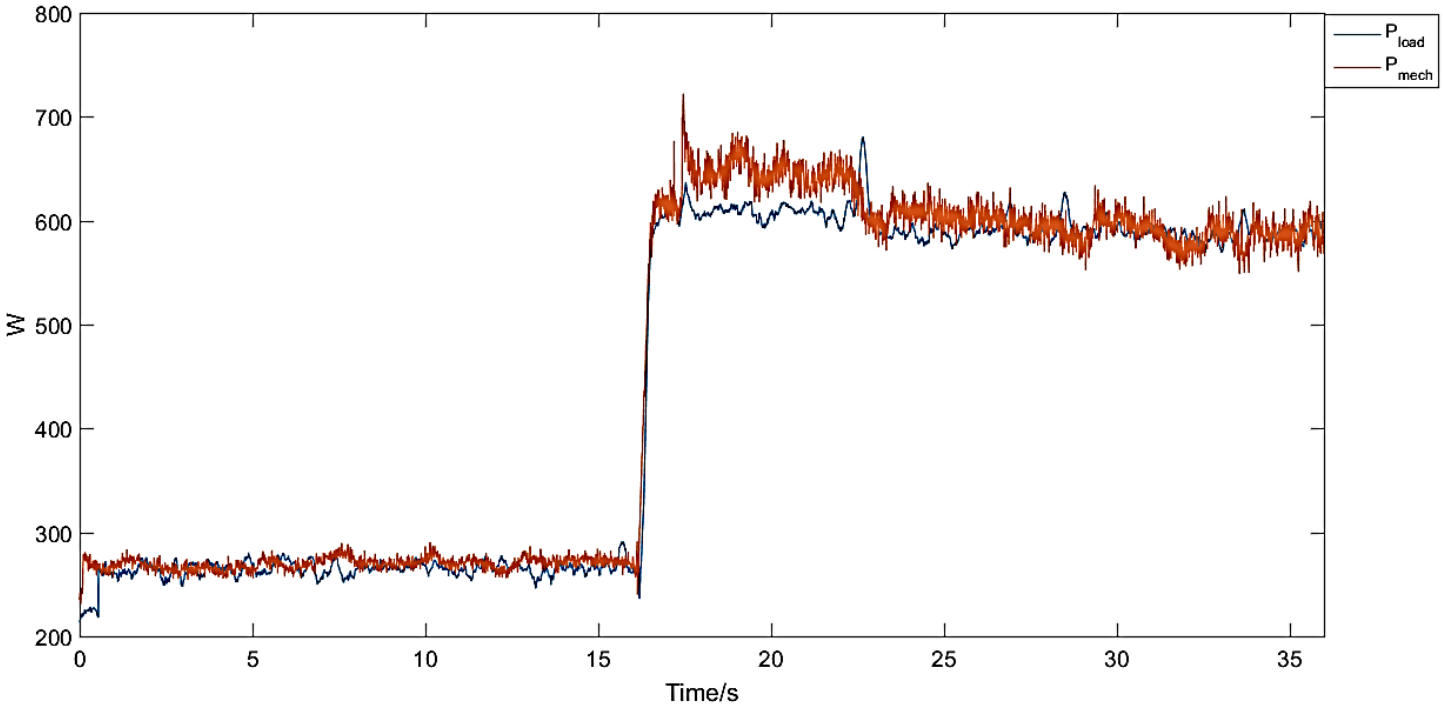

Figure 88: Mechanical input power and load's power demand

6.5 LCL-filter performance

The Yokogawa T1800 power analyser is used to calculate the THD in the current. With a sampling rate of 2M/s a more accurate result is found than if a PXI would be used. The LCL-filter performance is benchmarked with the performance of an L-filter with the same inductance to illustrate its effectiveness. Figure 89 shows the harmonic content of load-side currents through the L-filter. The scale used is logarithmic; the top of the scale represents 100A and the bottom represents 0.01A. The horizontal scale represents the harmonics of 50Hz. As expected the higher harmonics are attenuated the most. The lower harmonics, near the fundamental are mostly due to the control action. The larger the gains of the controls, the larger the control action would be when the system is not in steady state. This is another reason why a small a gain as possible is preferred when designing PI controllers.

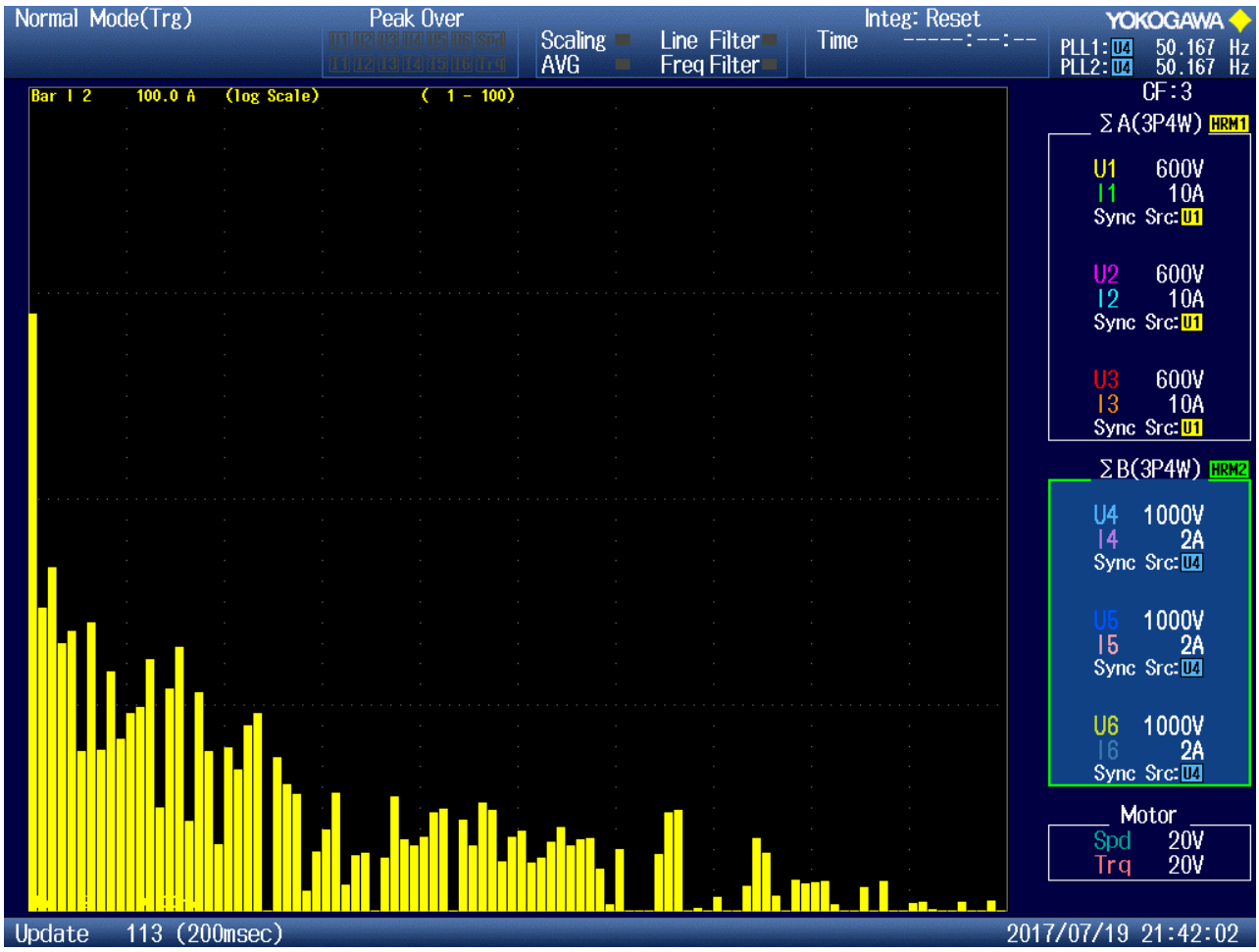

Figure 89: Harmonic content of current in L-filter

Figure 90 shows the harmonic content of the current in the LCL-filter. The filter displays much greater attenuation for higher harmonics as expected. The THD in the current is 3% well below the 5% required by the Grid-code. The low THD allows the controller design to accommodate larger gains in PI controllers if required.

Figure 90: Harmonic content of current in LCL-filter

Chapter 7

7. Conclusions and recommendation

7.1 Conclusions

A comprehensive study of the operation of a gas turbine generator is presented in this report. A turbine emulator is developed and implemented experimentally. A detailed experiment on possible control strategies for an IPM is conducted. A comparison of the control strategies identifies the best performing one. An unconventional control structure is devised that guarantees satisfactory performance of the system in grid-tied and isolated modes. Control of the system during unbalanced conditions is discussed and provision for reactive power compensation from the system is made. The following conclusions are drawn from the experiments:

- The simple structure of the Rowen gas turbine model makes it ideal for implementation on controller like the PXI. A DC-motor serves as convenient actuator in the emulation of a twin-shaft gas turbine because its torque and speed can be controlled by an armature voltage and DC-current. Using a DC-motor with a higher power rating than the IPM results in a better emulation of the gas turbine's speed. This is because large torques can be developed by the DC-motor to ensure accurate emulation of the gas turbine's dynamic behaviour, regardless of the loading by the IPM. The gas turbine emulator displays a maximum error of 2.5% from the model's reference speed.
- The IPM's different synchronous inductances provide control strategies that are not possible for an SPM. By varying the torque angle of stator current, the performances of ninety-degree torque angle control, maximum torque per ampere control and unity power factor control are compared. Metrics that are used to gauge each algorithm's performance are the DC-link voltage utilisation, torque development, conduction losses and power factor. Unity power factor control strategy yields the best performance of three. Through experimentation, a maximum efficiency control strategy is developed, that minimises conduction, windage, mechanical and core

losses. What's more, this control strategy performs well in terms of the performance metrics listed earlier.

- Load-side control in grid-tied and isolated operation is achieved in this report. An LCL-filter is designed according to grid code specifications for system integration with the utility grid or isolated load. The LCL-filter produces a THD of 3% which is below the maximum THD of 5% it is designed for. A recursive least squares grid voltage unbalance algorithm is then formulated. The algorithm is successfully implemented experimentally and is able to mitigatee negative sequence currents that result from the grid voltage unbalance.
- Two control structures are explored in this report. The first involves regulating the converter DC-link voltage from the load-side converter. This method results in unsatisfactory performance when the system is in isolated operation or is operating at a low power factor. In isolated mode, the load-side converter cannot regulate both the load and DC-link voltages simultaneously. When the system is operating at a low power factor, a high generator stator current is required to generated sufficient active power for DC-link voltage regulation. Thus, a second control structure is introduced that regulates the DC-link voltage from the generator-side converter. The load-side is then able to focus on the regulation of the load voltage and implement reactive power compensation.

7.2 Recommendation

The biggest limitation to this work was the malfunctioning encoder. This resulted in the experiments being conducted with a lower generator speed, DC-link voltage and grid voltage. However, this will not affect the findings of this report because the NTA, MTPA and UPF control strategies are derived from literature and show consistency with the experiments. The ME control scheme was formulated experimentally, therefore, the procedure is easily applicable to machines that operate at higher speeds and which are of a different topology. A sensorless method in attaining the rotor angle would eliminate the need for an encoder.

The RLS algorithm can theoretically be extended to accomodate grid voltage phase unbalances as well. A complete RLS algorithm that caters for both voltage magnitude and phase unbalances would be a strong advocate for its use over the popular SRF-PLL.

References

References

[1] W. G. Scott, "Micro-turbine generators for distribution systems," *IEEE Industry Applications Magazine,* vol. 4, *(3),* pp. 57-62, 1998. . DOI: 10.1109/2943.667911.

[2] L. C. L. Dale, L. B. Knowles and T. H. Morrison, "Gas-turbine plant for peak-load generation and synchronous compensation. A review of the installations for the CEGB," *Electrical Engineers, Proceedings of the Institution Of,* vol. 115, *(7),* pp. 969-979, 1968. . DOI: 10.1049/piee.1968.0177.

[3] (8 June). *How much carbon dioxide is produced when different fuels are burned?*. Available: https://www.eia.gov/tools/faqs/faq.php?id=73&t=11. [Oct. 10, 2018]

[4] (). *Natural Gas Overview*. Available: http://www.energy.gov.za/files/naturalgas_frame.html. [Oct. 10, 2018]

[5] (Jan 21,). *South Africa plans to add more natural gas, renewables to its energy supply mix*. Available: www.eia.gov/todayinenergy/detail.php?id=34752. [Oct. 10, 2018]

[6] S. Szewczuk, "Distributed generation systems for south africa based on renewable resources," in *ISES Solar World Congress,* 2009, pp. 1129-1137.

[7] S. K. Yee, J. V. Milanovic and F. M. Hughes, "Overview and Comparative Analysis of Gas Turbine Models for System Stability Studies," *IEEE Transactions on Power Systems,* vol. 23, *(1),* pp. 108-118, 2008.

[8] L. CUSSONS Technology, "P9005 CUSSONS TWO SHAFT AS TURBINE UNIT," 2004.

[9] AILER *et al*, "Nonlinear model-building of a low-power gas turbine," *Periodica Polytechnica Ser. Transp,* vol. 29, pp. 117-135, 2001.

[10] W. I. Rowen, "Simplified mathematical representations of heavy-duty gas turbines," *ASME J. Eng. Power,* vol. 105, pp. 865–869, 1983.

[11] L. N. Hannett, G. Jee and B. Fardanesh, "A governor/turbine model for a twin-shaft combustion turbine," *IEEE Transactions on Power Systems,* vol. 10, *(1),* pp. 133-140, 1995.

[12] Anonymous "Dynamic models for combined cycle plants in power system studies," *IEEE Transactions on Power Systems,* vol. 9, *(3),* pp. 1698-1708, 1994. . DOI: 10.1109/59.336085.

[13] M. Chinchilla, S. Arnaltes and J. L. Rodriguez-Amenedo, "Laboratory set-up for wind turbine emulation," in *Industrial Technology, 2004. IEEE ICIT '04. 2004 IEEE International Conference On,* 2004, . DOI: 10.1109/ICIT.2004.1490352.

[14] W. Li *et al*, "Research on wind turbine emulation based on DC motor," in *2007 2nd IEEE Conference on Industrial Electronics and Applications,* 2007, . DOI: 10.1109/ICIEA.2007.4318881.

[15] B. A. Correa *et al*, "Driving a synchronous motor so that it emulates a twin-shaft gas turbine engine," in *6th IET International Conference on Power Electronics, Machines and Drives (PEMD 2012),* 2012, . DOI: 10.1049/cp.2012.0296.

[16] B. A. Correa *et al*, "Gas turbine emulator for testing of high-speed generators," in *Proceedings of the IEEE SoutheastCon 2010 (SoutheastCon),* 2010, . DOI: 10.1109/SECON.2010.5453882.

[17] A. Rolan *et al*, "Modeling of a variable speed wind turbine with a permanent magnet synchronous generator," in *Industrial Electronics, 2009. ISIE 2009. IEEE International Symposium On,* 2009, pp. 734-739.

[18] N. K. Jena *et al*, "A decoupled control strategy for a grid connected direct-drive PMSG based variable speed wind turbine system," in *2015 International Conference on Energy, Power and Environment: Towards Sustainable Growth (ICEPE),* 2015, . DOI: 10.1109/EPETSG.2015.7510098.

[19] R. Krishnan, "PermanentMagnet synchronous," in *Electric Motor Drives: Modeling, Analysis, and Control*Anonymous Prentice Hall, 2001, pp. 513.

[20] S. Zhang *et al*, "Design of a Robust Grid Interface System for PMSG-Based Wind Turbine Generators," *IEEE Transactions on Industrial Electronics,* vol. 58, *(1),* pp. 316-328, 2011. . DOI: 10.1109/TIE.2010.2044737.

[21] S. h. Dong, Y. Wang and S. w. Shu, "A novel unity power factor control strategy based on flux-linkage re-orientation for PMSG based wind turbine," in *2014 IEEE Conference and Expo Transportation Electrification Asia-Pacific (ITEC Asia-Pacific),* 2014, . DOI: 10.1109/ITEC-AP.2014.6941171.

[22] S. Morimoto *et al*, "Output maximization control for wind generation system with interior permanent magnet synchronous generator," in *Conference Record of the 2006 IEEE Industry Applications Conference Forty-First IAS Annual Meeting,* 2006, . DOI: 10.1109/IAS.2006.256566.

[23] D. M. Miao, J. X. Shen and D. Shi, "Permanent magnet synchronous generators with various designs and control strategies," in *2013 Eighth International Conference and Exhibition on Ecological Vehicles and Renewable Energies (EVER),* 2013, . DOI: 10.1109/EVER.2013.6521550.

[24] Woei-Luen Chen and Yuan-Yih Hsu, "Direct output voltage control of a static synchronous compensator using current sensorless d-q vector-based power balancing scheme," in *2003 IEEE PES Transmission and Distribution Conference and Exposition (IEEE Cat. no.03CH37495),* 2003, . DOI: 10.1109/TDC.2003.1335333.

[25] C. Schauder and H. Mehta, "Vector analysis and control of advanced static VAr compensators," *IEE Proceedings C - Generation, Transmission and Distribution,* vol. 140, *(4),* pp. 299-306, 1993. . DOI: 10.1049/ip-c.1993.0044.

[26] M. M. Hussein *et al*, "Control of a variable speed stand alone wind energy supply system," in *Power and Energy (PECon), 2012 IEEE International Conference On,* 2012, pp. 71-76.

[27] D. N. Gaonkar, R. N. Patel and G. N. Pillai, "Dynamic model of microturbine generation system for grid connected/islanding operation," in *Industrial Technology, 2006. ICIT 2006. IEEE International Conference On,* 2006, pp. 305-310.

[28] S. K. Nayak and D. N. Gaonkar, "Modeling and performance analysis of microturbine generation system in grid connected/islanding mode," in *Power Electronics, Drives and Energy Systems (PEDES), 2012 IEEE International Conference On,* 2012, pp. 1-6.

[29] R. Teodorescu and F. Blaabjerg, "Flexible control of small wind turbines with grid failure detection operating in stand-alone and grid-connected mode," *Power Electronics, IEEE Transactions On,* vol. 19, *(5),* pp. 1323-1332, 2004.

[30] H. S. Kim *et al*, "Design of current controller for 3-phase PWM converter with unbalanced input voltage," in 1998, . DOI: 10.1109/PESC.1998.701945.

[31] V. P. Suppioni, A. P. Grilo and J. C. Teixeira, "Control methodology for compensation of grid voltage unbalance using a series-converter scheme for the DFIG," *Electr. Power Syst. Res.,* vol. 133, pp. 198-208, 2016. Available: http://www.sciencedirect.com/science/article/pii/S0378779615004113. DOI: //doi.org/10.1016/j.epsr.2015.12.034.

[32] H. Cha and T. K. Vu, "Comparative analysis of low-pass output filter for single-phase grid-connected photovoltaic inverter," in *2010 Twenty-Fifth Annual IEEE Applied Power Electronics Conference and Exposition (APEC),* 2010, . DOI: 10.1109/APEC.2010.5433454.

[33] W. Zhao and G. Chen, "Comparison of active and passive damping methods for application in high power active power filter with LCL-filter," in *2009 International Conference on Sustainable Power Generation and Supply,* 2009, . DOI: 10.1109/SUPERGEN.2009.5347992.

[34] A. Reznik *et al*, "Filter Design and Performance Analysis for Grid-Interconnected Systems," *Industry Applications, IEEE Transactions On,* vol. 50, *(2),* pp. 1225-1232, 2014.

[35] M. Liserre, A. Dell'Aquila and F. Blaabjerg, "Stability improvements of an LCL-filter based three-phase active rectifier," in *Power Electronics Specialists Conference, 2002. Pesc 02. 2002 IEEE 33rd Annual,* 2002, pp. 1201 vol.3.

[36] S. Jayalath and M. Hanif, "Generalized LCL-Filter Design Algorithm for Grid-Connected Voltage-Source Inverter," *IEEE Transactions on Industrial Electronics,* vol. 64, *(3),* pp. 1905-1915, 2017. . DOI: 10.1109/TIE.2016.2619660.

[37] B. A. Correa, "Emulation of an Aeroderivative Twin-Shift Gas Turbine Engine using an AC Electrical Motor Drive." , University of South Carolina, 2013.

[38] A. A. - Fejer, "The Compound Heat Pump Gas Turbine: An Approach to Energy Conservation for Process Industries," vol. -, *(- 79665),* pp. V01BT02A086, -, 1980.

[39] Y. S. H. Najjar, "Gas turbine cogeneration systems: a review of some novel cycles," *Applied Thermal Engineering,* vol. 20, *(2),* pp. 179-197, 2000. Available: http://www.sciencedirect.com.ezproxy.uct.ac.za/science/article/pii/S1359431199000198. DOI: //doi-org.ezproxy.uct.ac.za/10.1016/S1359-4311(99)00019-8.

[40] Y. Zhu and K. Tomsovic, "Development of models for analyzing the load-following performance of microturbines and fuel cells," *Electric Power Systems Research,* vol. 62, *(1),* pp. 1-11, 2002. Available: http://www.sciencedirect.com.ezproxy.uct.ac.za/science/article/pii/S0378779602000330. DOI: //doi-org.ezproxy.uct.ac.za/10.1016/S0378-7796(02)00033-0.

[41] S. R. Guda, C. Wang and M. H. Nehrir, "Modeling of Microturbine Power Generation Systems," *Electric Power Components and Systems,* vol. 34, *(9),* pp. 1027-1041, 2006. Available: https://doi-org.ezproxy.uct.ac.za/10.1080/15325000600596767. DOI: 10.1080/15325000600596767.

[42] D. M. Soto, A. Hasanzadeh and C. S. Edrington, "Gas turbine-synchronous generator system emulation using power electronics converters," in *2012 North American Power Symposium (NAPS),* 2012, . DOI: 10.1109/NAPS.2012.6336386.

[43] M. S. Kandil, M. El-Saadawi and K. Abo-Al-Ez, "Dynamic Modeling and Control of Microturbine DG System for Autonomous Operation," *IEEE 14th International Middle East Power Systems Conference (MEPCON'2010),* 2010.

[44] H. Keshtkar, A. Alimardani and B. Abdi, "Optimization of Rotor Speed Variations in Microturbines," *Energy Procedia,* vol. 12, pp. 789-798, 2011. Available: http://www.sciencedirect.com/science/article/pii/S187661021101931X. DOI: //doi.org/10.1016/j.egypro.2011.10.105.

[45] Jingya Dai, D. D. Xu and Bin Wu, "A Novel Control Scheme for Current-Source-Converter-Based PMSG Wind Energy Conversion Systems," *Power Electronics, IEEE Transactions On,* vol. 24, *(4),* pp. 963-972, 2009.

[46] A. A. Daoud, S. S. Dessouky and A. A. Salem, "Control scheme of PMSG based wind turbine for utility network connection," in *Environment and Electrical Engineering (EEEIC), 2011 10th International Conference On,* 2011, pp. 1-5.

[47] I. Boldea and S. A. Nasar, "Synchronous motors for drives," in *Electric Drives*, Second Edition ed.Anonymous CRC Press, 1998, pp. 253.

[48] M. Hanif, "Active damping techniques for suppressing the LCL-filter resonance in distributed generators," in 2013, . DOI: 10.1109/UPEC.2013.6714978.

[49] V. Blasko and V. Kaura, "A new mathematical model and control of a three-phase AC-DC voltage source converter," *Power Electronics, IEEE Transactions On,* vol. 12, *(1),* pp. 116-123, 1997.

[50] M. N. Uddin *et al*, "Comparison of position sensorless control based back-EMF estimators in PMSM," in 2015, . DOI: 10.1109/ICCITechn.2015.7488033.

[51] S. Gao and M. Barnes, "Phase-locked loops for grid-tied inverters: Comparison and testing," in 2016, . DOI: 10.1049/cp.2016.0304.

[52] S. Särkkä, *Bayesian Filtering and Smoothing.* 20133.

[53] R. Isermann and M. Münchhof, *Identification of Dynamic Systems.* 2011.

[54] Y. Shu and A. Takahiro, "Determination of direct and quadrature axis inductances of synchronous reluctance motors with allowance for cross saturation," *Elect. Eng. Jpn.,* vol. 149, *(4),* pp. 52-59, 2004. Available: https://doi.org/10.1002/eej.10377. DOI: 10.1002/eej.10377.

[55] X. Wei *et al*, "Design of LCL-filter for wind power inverter," in 2010, . DOI: 10.1109/WNWEC.2010.5673156.

[56] R. Peña-Alzola *et al*, "*LCL*-Filter Design for Robust Active Damping in Grid-Connected Converters," *IEEE Transactions on Industrial Informatics,* vol. 10, *(4),* pp. 2192-2203, 2014. . DOI: 10.1109/TII.2014.2361604.

[57] M. Liserre, F. Blaabjerg and S. Hansen, "Design and control of an LCL-filter-based three-phase active rectifier," *IEEE Transactions on Industry Applications,* vol. 41, *(5),* pp. 1281-1291, 2005. . DOI: 10.1109/TIA.2005.853373.

[58] M. Dou and R. Fu, "Experiment and analysis of d- and q-axes inductances of interior permanent magnet synchronous motor used in electric vehicles," in 2012, .

[59] K. Astrom and T. Hagglund, *PID Controllers: Theory, Design, and Tuning.* (2nd ed.) ISA, 1995.

[60] Z. Xu *et al*, "Over-modulation control strategy of SVPWM review," in 2016, . DOI: 10.1109/CCDC.2016.7531532.

[61] C. M. Wolf, M. W. Degner and F. Briz, "Analysis of current sampling errors in PWM, VSI drives," in 2013, . DOI: 10.1109/ECCE.2013.6646922.

[62] V. Blasko, V. Kaura and W. Niewiadomski, "Sampling of discontinuous voltage and current signals in electrical drives: a system approach," *IEEE Transactions on Industry Applications,* vol. 34, *(5),* pp. 1123-1130, 1998. . DOI: 10.1109/28.720453.

[63] F. Briz *et al*, "Current sampling and measurement in PWM operated AC drives and power converters," in 2010, . DOI: 10.1109/IPEC.2010.5543175.

Appendix A

Below are a set of derivation results used in calculating the solution for a least-squares problem for a vector $\boldsymbol{x}$ and a matrix $\boldsymbol{M}$.

$$\frac{d}{d\boldsymbol{x}}(\boldsymbol{M}\boldsymbol{x}) = \boldsymbol{M}^T$$

$$\frac{d}{d\boldsymbol{x}}(\boldsymbol{x}^T\boldsymbol{M}) = \boldsymbol{M}$$

$$\frac{d}{d\boldsymbol{x}}(\boldsymbol{x}^T\boldsymbol{x}) = 2\boldsymbol{x}$$

$$\frac{d}{d\boldsymbol{x}}(\boldsymbol{x}^T\boldsymbol{M}\boldsymbol{x}) = \boldsymbol{M}\boldsymbol{x} + \boldsymbol{M}^T\boldsymbol{x} \quad (= \mathbf{2}\boldsymbol{M}\boldsymbol{x} \text{ if } \boldsymbol{M}^T = \boldsymbol{M})$$

Appendix B

The schematic of the voltage level shifting board is given below.